

**University of Stuttgart**  
Germany



**INSTITUTE FOR  
COMPUTATIONAL  
PHYSICS**

**Diploma thesis**

**An iterative Poisson Boltzmann solver for  
regions with dielectric mismatch**

submitted by

**Alexander Schlaich**

University of Stuttgart  
Institute for Computational Physics

01. September 2011

Hauptberichter:  
Mitberichter:

Prof. Dr. Christian Holm  
Prof. Dr. Udo Seifert



# Zusammenfassung

Durch die Langreichweiteigkeit elektrostatischer Wechselwirkungen weichen die physikalischen und chemischen Eigenschaften von Elektrolytlösungen selbst bei sehr niedrigen Konzentrationen erheblich von den Eigenschaften idealer Lösungen ab. Glücklicherweise lässt sich mittels der sogenannten Mean-Field Näherung eine gute Beschreibung der thermodynamischen Eigenschaften einer Elektrolytlösung erreichen, falls nur einwertige Salzionen bei Raumtemperatur berücksichtigt werden sollen. In solch einer Mean-Field Methode wird die Poisson-Gleichung mit der Boltzmann Wahrscheinlichkeitsdichte, die die Ionenverteilung beschreibt, zur sogenannten Poisson–Boltzmann Gleichung gekoppelt. Diese stellt ein vielseitiges und äußerst erfolgreiches Hilfsmittel zur Untersuchung der Eigenschaften von Elektrolyten in Lösungen zur Verfügung.

Die Poisson–Boltzmann Gleichung kann mit Hilfe verschiedener numerischer Verfahren gelöst werden, unter welchen insbesondere auch die Methode der Finiten Elemente aufgrund ihrer Flexibilität erfolgversprechend ist. An Grenzschichten verschiedener Materialien – wie beispielsweise am Rand großer kolloidaler Teilchen, welche in Wasser Gegenionen dissoziieren, kommt es für gewöhnlich zu einem Sprung der dielektrischen Konstante, so dass im Allgemeinen die Ortsabhängigkeit der Dielektrizitätskonstante berücksichtigt werden muss. Der dabei entstehende numerische Mehraufwand macht ein solches Vorgehen nicht besonders effizient, da das Gebiet, auf welchem die Gleichungen gelöst werden müssen, auch auf die Bereiche welche der Flüssigkeit nicht zugänglich sind ausgedehnt werden muss. Zusätzlich erschwert die Behandlung der Unstetigkeiten an den Grenzflächen die Methodik zur Lösung des mathematischen Problems und verschlechtert dessen Konvergenzeigenschaften.

In dieser Arbeit wird ein Verfahren vorgestellt, das es ermöglicht die korrekte Lösung der Poisson–Boltzmann Gleichung im Falle unterschiedlicher dielektrischer Eigenschaften zu bestimmen. Hierzu werden Polarisationsladungsdichten an der Oberfläche eingeführt, wodurch Unstetigkeiten an den Grenzflächen implizit behandelt werden können, und somit in einem iterativen Verfahren die korrekten Randbedingungen bestimmt werden können. Dieses Verfahren, das wir als Iterativen Poisson–Boltzmann Löser (IPBS) bezeichnen, implementierten wir mit Hilfe der Distributed and Unified Numerics Environment (DUNE). Bevor wir damit die physikalisch interessante Fragestellung der zwischen zwei geladenen Kolloiden wirkenden mittleren Kräfte untersuchten, führten wir Testrechnungen anhand einiger Modelle durch, für die eine analytische Näherung bekannt ist. Soweit wir wissen, wurde bisher noch keine Lösung eines solchen Zwei-Kolloid-Problems veröffentlicht, in der auch Sprünge der Dielektrizitätskonstante berücksichtigt wurden. Mit Hilfe des IPBS

---

untersuchen wir die elektrostatische und osmotische Kraft zwischen zwei Kolloiden und gingen desweiteren der Frage nach, in wie weit das Konzept der Ladungsrenormalisierung auch außerhalb seines eigentlichen Parameterraumes seine Gültigkeit behält. Dabei vergleichen wir die erhaltenen Resultate insbesondere auch mit Ergebnissen aus Molekulardynamiksimulationen von Kreer et. al. [44], deren Behauptung von einem Scheitern des Konzeptes der Ladungsrenormalisierung wir nicht bestätigen können.

Die vorliegende Arbeit ist dabei wie folgt untergliedert: In der Einleitung soll eine Einführung zur Motivation dieser Arbeit gegeben werden, wobei auch auf die historische Entwicklung der Poisson–Boltzmann Theorie eingegangen wird; eine Herleitung der Poisson–Boltzmann Gleichung und damit verbundener Konzepte findet sich im zweiten Kapitel; im dritten Kapitel wird eine Zusammenfassung der Methode der Finiten Elemente gegeben sowie eine Beschreibung des Algorithmus hinter IPBS und Details zu dessen Implementierung; einige Testrechnungen und analytischen Vergleiche zur Sicherstellung der korrekten Arbeitsweise des Computerprogramms und des Algorithmus werden in Kapitel 4 vorgestellt; das fünfte Kapitel schließlich ist dem Zwei-Kolloid-Problem und dessen Lösung mittels IPBS gewidmet; das letzte Kapitel fasst die Resultate dieser Arbeit zusammen und liefert einen Ausblick auf künftige Möglichkeiten.

# Abstract

The physico-chemical properties of electrolytic solutions, even at very low concentrations, differ much from ideal ones, due to the long range nature of the electrostatic interaction. Fortunately, a mean-field approach can provide a good approximation to the thermodynamics of an electrolytic solution, if only monovalent ions at room temperature are present in the system of interest. The mean field approach which couples the Poisson equation to the Boltzmann probability distribution of ions creates the so-called Poisson–Boltzmann equation, an extremely successful and versatile tool to investigate the properties of electrolytes in solution.

The Poisson–Boltzmann equation can be solved using different computational techniques, but those based on finite element methods have proven to be one of the most successful due to their flexibility. In the presence of a dielectric mismatch at interfaces, as could be the case for a large colloidal particle releasing counter-ions in aqueous solution, or in the presence of confining walls, the Poisson–Boltzmann equation has to be generalized to include the dielectric boundary effects. This approach could, however, be not the most efficient one, because of the need for extending the domain of computation also to regions inaccessible to the solution, and because of the difficulties associated with the treatment of discontinuities at the interfaces.

In this thesis a method is presented that is able to recover the correct solution of the Poisson–Boltzmann equation in the presence of dielectric mismatch exploiting the surface polarization charges. This approach has the advantages of treating discontinuities implicitly, and to be able to determine iteratively the correct boundary conditions. This method, called Iterative Poisson Boltzmann Solver (IPBS), has been implemented in the Distributed and Unified Numerics Environment (DUNE), and has been tested for several test cases against analytical approximations of the theory before being applied to the interesting problem of the potential of mean force acting between two charged colloidal particles. To the best of our knowledge, no prior solution to the problem of two charged colloids having a dielectric mismatch with the surrounding solvent has ever been presented. Furthermore we apply the IPBS method to investigate the electrostatic and osmotic forces acting between the two colloids, determine the range of validity of theoretical approaches based on the concept of charge renormalization. We compare our results to those Kreer et. al. [44] recently obtained using Molecular Dynamics simulations whose claim of a failure of the Alexander charge renormalization concept we cannot reproduce.

This thesis is organized as follows: in the Introduction, the motivations which led to this work are presented, along with a historical background concerning Poisson–Boltzmann

---

theory; the derivation of the Poisson–Boltzmann equation and related concepts are presented in the second chapter; the third chapter introduces the finite elements method, the IPBS algorithm and its implementation; in the fourth chapter the various test cases which were used to validate the proper implementation of the algorithm are presented; the fifth chapter is devoted to the two-colloid problem and to its solution using IPBS; Conclusions and an outlook are given in the last chapter.

# **Erklärung**

Hiermit erkläre ich, dass ich die vorliegende Arbeit selbständig und ohne fremde Hilfe bzw. unerlaubte Hilfsmittel angefertigt habe und keine anderen als die angegebenen Quellen und Hilfsmittel benutzt, sowie die den benutzten Quellen wörtlich oder inhaltlich entnommenen Stellen als solche kenntlich gemacht habe.

Stuttgart, den 01. September 2011

Alexander Schlaich



# Contents

<b>1. Introduction</b>	<b>1</b>
1.1. Electrostatic interactions in liquid systems . . . . .	1
1.2. Strategy . . . . .	4
1.2.1. Description of the system . . . . .	4
1.2.2. Solution of Poisson–Boltzmann equation . . . . .	5
1.2.3. Algorithm theoretical background . . . . .	6
<b>2. Theoretical background</b>	<b>9</b>
2.1. Classical electrostatics . . . . .	9
2.1.1. Surface charges and dipoles . . . . .	10
2.2. Derivation of the Poisson Boltzmann Equation . . . . .	11
2.2.1. Statistical mechanics description of the system . . . . .	11
2.2.2. The mean-field approximation . . . . .	13
2.3. The reduced electrostatic potential . . . . .	16
2.4. Debye–Hückel theory . . . . .	17
2.4.1. The Debye screening length . . . . .	18
2.4.2. General solution of the linearized PBE . . . . .	18
2.5. Effective interactions between colloidal particles . . . . .	21
<b>3. Algorithm and implementation</b>	<b>27</b>
3.1. The finite element method . . . . .	27
3.2. The DUNE project . . . . .	33
3.3. Mesh generation using Gmsh . . . . .	35
3.4. Algorithm details and implementation . . . . .	39
3.4.1. Including dielectric mismatch . . . . .	41
3.4.2. Use of symmetry . . . . .	43
3.4.3. The configuration file . . . . .	46
<b>4. Verification</b>	<b>49</b>
4.1. A single spherical particle . . . . .	49
4.2. Planar symmetry . . . . .	57
4.2.1. A single planar surface . . . . .	57
4.2.2. The potential between two plane surfaces . . . . .	61

<b>5. The two-colloid problem</b>	<b>67</b>
5.1. The force in the effective surface charge density model . . . . .	67
5.1.1. Force calculation method . . . . .	67
5.1.2. Effective ion density and overlap of Debye layers . . . . .	71
5.2. Colloidal charge renormalization . . . . .	74
5.3. Influence of jumps of the dielectric constant at the colloids surface . . . . .	82
<b>6. Conclusions and outlook</b>	<b>85</b>
<b>7. Acknowledgements</b>	<b>87</b>
<b>A. Analytical results</b>	<b>89</b>
A.1. Gouy-Chapman theory of a charged plane . . . . .	89

# 1. Introduction

## 1.1. Electrostatic interactions in liquid systems

Under the name of soft-matter go all those systems for which the energy associated to thermal fluctuation is comparable with the interaction energy of its constituents. This feature typically leads to very rich phase diagrams of the systems but, on the other hand, makes the theoretical treatment of these systems very complicated. Electrostatic interactions play a major role in soft-matter systems, and can be exploited to achieve a large variety of physico-chemical properties [41]. Typical systems range from macroscopic charged particles suspended in a liquid [26] to the modeling of membranes [4], or the crystallization of charged colloidal dispersions [66]. Also other systems can be described in terms of soft-matter physics, covering biological properties of polyelectrolytes [24] as well as industrial important analysis of the swelling behavior of hydrogels [52].

In many cases, preferential adsorption of electrolytes, dissociation of ions due to polar solvents, or chemical reactions produce charged interfaces, at which often the intrinsic physical properties change abruptly. For example at the interface of colloids ( $\varepsilon_r \approx 4$ ) suspended in water ( $\varepsilon_r \approx 80$ ), the dielectric constant changes significantly, inducing orientation and polarization of interfacial molecules contributing to the microscopic separation of charge at these interfaces.

The resulting forces between surfaces of mesoscopic or macroscopic bodies through a third medium (e.g. air, electrolyte solution, ...) are commonly referred to as surface forces [38]. When modeling a system of mesoscopic particles in an electrolyte solution (fig. 1.1.1), the interaction energy can be simplified to a sum of five terms:

1. Overlap repulsion, which occurs when the electron clouds of two molecules begin to overlap. The Pauli exclusion principle forces the overlap electrons into higher excited states, the resulting energy is approximately squared to the overlap of the electron probability density. For macroscopic (like charged walls) or mesoscopic, and in particular spherical particles, it is generally appropriate to model them as *hard* surfaces, i.e. the energy contribution is zero for a finite distance and infinite for overlapping particles.
2. Charge-transfer, the donation of excess electrons to acceptor molecules, is generally negligible except for semi-conducting crystals. Therefore we have neglected this contribution since the focus of this thesis is on colloids.

## 1. Introduction

---

3. Electrostatic interactions which are dominated by the long-range nature of Coulomb's law. On the contrary, higher order multipole contributions become relevant on short length-scales.
4. Interactions between electrical and induced dipoles. This term will give a contribution proportional to the polarizability and distance.
5. Dispersion, the interaction between statistically induced dipoles. Together with the electrostatic multipole-interactions and the preceding item they are commonly referred to as van-der-Waals forces.

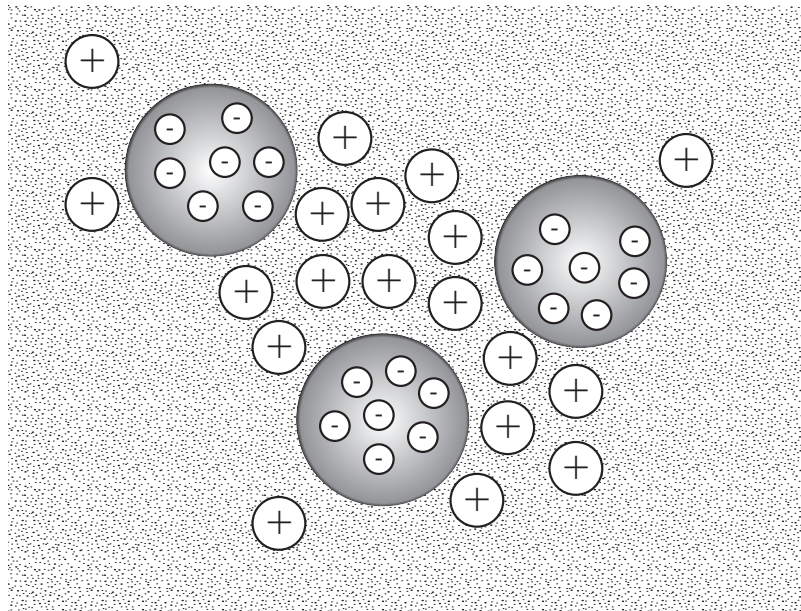


Figure 1.1.1.: Charged mesoscopic particles will attract counter-ions when dissolved in an electrolyte solution. The effective interaction can then be described in terms of surface forces, of which the most important will be the Coulomb force.

More than a century ago, Gouy [31] and Chapman [17] calculated the spatial distribution of monovalent ions near an infinite, uniformly charged surface. As any charged object immersed in an ionic solution, the interface attracts a cloud of opposite charges forming a diffuse *electric double layer*. Using a mean-field approach, the distribution of ions is given by the interplay of electrostatic interactions, both between the ions themselves and between ions and interface, and the entropy of the ions in the solution.

This approach was generalized by Debye and Hückel [18] in 1923, whose work derived the energy of an ion in the solution using a linearized approach, and led to the successful interpretation of thermodynamic data. The *Poisson–Boltzmann equation*, the result of the mean-field description of the soluted ions, is still an important tool in many branches

of research [28]. As the equation is a second order nonlinear partial differential equation, analytical solutions are only available for very few systems [34], most of them using power series expansions.

The statistical mechanics framework, on which the work of Debye and Hückel was based, was examined by Onsager [56] in 1933, and by Fowler and Guggenheim [29] in 1939, using the potential of mean-force. As Kirkwood [43] pointed out in 1934, the Poisson–Boltzmann approach is based on the assumption that it is possible to replace the potential of mean-force by the mean electrostatic potential. For commonly studied systems this latter approximation has nearly no influence on systems where ions have spherical shape, the ion-concentration is low enough for neglecting correlations, and the valency of the ions is low and (nearly) the same (i.e. the electrostatic interaction is small). Due to its outstanding success, Poisson–Boltzmann theory has been improved and extended ever since the thirties and various ways of calculating the free energy of such systems, most of them based on the linearization of the potential, have been developed.

One of the most remarkable and still popular approaches for the free energy of interacting particles was that of Derjaguin and Landau [19] (1941), and Verwey and Overbeek [71] (1948), hence the name of DLVO theory. Based on the expansion of the ideal gas free energy they derived an expression for an effective interaction potential between colloidal particles. Such interaction potentials are often used to interpret experiments on colloid aggregation behavior [27].

Under active research is the field of like-charge attraction in confined geometries [10]. Such attraction between colloidal particles of the same sign can also be observed for charged colloids and polyelectrolytes in solution introduced into a quasi-two-dimensional fluid. The fluid in such a slit is usually bounded by glass and silica surfaces that are negatively charged in contact with water, and the slit heights range to less than 100 nm [46]. Confining DNA molecules in that kind of geometries might lead to new insight into entropic configurational effects [45]. Within the framework of the PB theory, the interaction between identical colloidal particles is always repulsive, irrespective of whether the particles are isolated or confined [63]. The exact physical origin of these counter-intuitive forces remains unclear. However, polarizable objects in a nonuniform electric field, as caused by a geometrical confinement, experience a net force whose direction depends on the effective polarization of the object in the suspending medium [38]. The effect of such a confinement on colloidal particles is to the best of our knowledge not yet answered satisfactorily.

Another field of huge interest is the concept of an effective potential between charged colloidal particles [11] [23]. If two or more colloids approach, their electric double layers begin to overlap. In systems, where the salt concentration is low, the extension of these double layers is large, and therefore – especially for a dense concentration of colloids – deviations from pairwise additive interaction energies are expected. The DLVO theory predicts that an isolated pair of charged colloids in an aqueous salt solution will interact via a repulsive Yukawa potential in the case of a negligible overlap of their double layers.

## 1. Introduction

---

Examining the behavior of charge-stabilized colloidal suspensions using a simulation based on a full nonlinear Poisson–Boltzmann mean-field description, Dobnikar, Rzehak and von Grünberg [39] showed that there is a regime in the phase diagram where the DLVO description in terms of pairwise interacting Yukawa potentials differs drastically. However, their solution approach is based on the assumption of a constant surface charge on the colloids’ surface, which in the case of overlapping double layers becomes questionable as the effective charge density on the surface will be affected by the electrostatic repulsion of the other particles. In that case polarization effects cannot be neglected and the potential at the particle’s surface becomes complicated.

Though there are several numerical methods to effectively model the interaction of two charged spheres, using either the approach of constant surface charges [48] or constant surface potential [7], most of them use linearized Poisson–Boltzmann theory or performe some other kind of simplification. Including dielectric polarization effects into such a mean-field approximation is a non-trivial task though it can be done, for example by using linearized perturbation theory [36], or introducing a nonlinear dielectric response into the canonical partition function, resulting in a so-called dipolar Poisson Boltzmann equation [2].

This is where our algorithm shows promising results, including dielectric polarization in an iterative scheme determining the boundary conditions. Using standard finite element methods, we solve the nonlinear Poisson–Boltzmann equation in the solution domain for an unknown boundary condition at the particle’s surface, which is determined iteratively in a self-consistent approach from the electrostatic potential in the whole domain, including the jump of the electric field on boundaries where regions of different dielectric constant come in contact.

## 1.2. Strategy

### 1.2.1. Description of the system

In this work we will focus on the analysis of the potential, the ion distribution, and the resulting forces on mesoscopic colloids in a system of such colloids soluted in an electrolyte solution. Assuming the ions in solution to be of spherical shape and that they are small compared to the length-scale of interest, the electrolyte solution can be modeled as an aqueous fluid containing point charges, while the macro-ions are treated as impenetrable, charged or neutral and polarizable or non-polarizable objects. This description of small spherical ions is equivalent to that of a conducting particle of arbitrary shape. Furthermore we will limit the interactions between particles to only include the electrostatic forces besides entropic effects, as in the systems studied in this thesis this contribution is the most significant.

According to the laws of statistical mechanics, the potential, as well as the ion dis-

tribution, depends on the total energy of all ions in all possible configurations. The system is assumed to be in thermodynamic equilibrium in a canonical ensemble, having a well-defined constant temperature  $T$ , and a constant volume  $V$ . The electrostatic properties of the system can be obtained by the solution of the Poisson–Boltzmann equation (chapter 2.2), one of the most important equations of statistical physics [37].

In this context, the system consists of  $N_i$  ions of species  $s$ . In solution, each of these  $N_s$  ion species, that will only differ in their valency  $z_s$  as they are modeled as point-charges, will have a concentration  $c_s^{eq}$ . It turns out that the limitation to purely electrostatic interactions, approximating a single ion's potential energy  $w_i = z_i e \Psi$  by its electrostatic energy, is not a very crude one for systems where the concentration of colloidal particles is low enough such that correlation effects can be neglected, and neither the electrostatic potential  $|\Psi|$  nor the ion densities are too large such that ion correlations and excluded volume effects negligible as well[49]. Though there have been many points of criticism of the simple assumptions used for the Poisson–Boltzmann theory (e.g. [16]), it has been shown to model numerous systems of interest quite accurately, especially in the field of colloidal suspensions [62] and biological structural analysis [28]. Even in its linearized form, it reproduces a large range of experimental data and nowadays solutions of the Poisson–Boltzmann equation are an active field of research.

### 1.2.2. Solution of Poisson–Boltzmann equation

As the nonlinear Poisson–Boltzmann equation (NPB) is a second order nonlinear differential equation, it has resisted successfully from being solved analytically in most cases. There are only a few cases like an infinite charged wall (Gouy-Chapman model) or an infinite charged tube for which an analytical solution is available, both for the case of having salt in the solution and for the salt-free case, where only a number  $N$  of counter-ions is put into the system to ensure electro-neutrality with the  $N_C$  charged macro-ions of charge  $Ze$ ,  $Nz_i = N_C Z$ . Under the assumption of low salt concentration (i.e. small  $\kappa$ ), the NPB can be linearized, resulting in an excellent approximation for a huge number of systems, and making analytical solutions available for a larger range of geometries.

However, in the general case the NPB has to be solved numerically. Typical methods are finite differences [51] and multi-grid methods [35][34]. For our system, Poisson's equation has to be solved within the colloidal particle, whereas in the surrounding solution the nonlinear Poisson–Boltzmann equation determines the electrostatic potential and one has to account for the continuity of the potential and for Gauss' law for the electric field at the surface. Another possibility of solving the NPB is the method of finite elements, on which we will focus as it is rather simple to implement that kind of boundary condition within a FEM, allowing for interfaces of nearly arbitrary shape.

As it is a rather large undertaking to build a finite element solver from scratch we instead opted to explore the wide range of commercial and open source packages available. The goal of this thesis was to develop a powerful and efficient, well tested and well

## 1. Introduction

---

understood implementation, that is easy to use and offers a broad range of applications. Therefore we decided to use DUNE [57], the Distributed and Unified Numerics Environment for the implementation of the finite element method, which is a modular toolbox for solving partial differential equations (PDEs) with grid-based methods. It supports the easy implementation of methods like Finite Elements (FE), Finite Volumes (FV), and also Finite Differences (FD). Using its discretization module `dune-pdelab`, one is able build up a library of finite element methods in an easy and expandable way that is closely related to the mathematical formulation of finite element methods [58].

In our implementation, the user has to provide the system parameters, and a mesh, which contains all the geometrical information and boundary conditions for the calculation. We decided to provide input for the GMSH mesh format, which offers using a scripted description of the system setup and then provides powerful discretization algorithms of GMSH [30] to obtain the coordinates of elements and nodes. The implementation, which is fully parallelized, then is capable to use different backends for the exchangeable, highly efficient solvers for the resulting algebraic set of equations. Combining it with the parallel features of the mesh generation and the algorithm implementation, it is then perfectly suited to make use of modern features of high performance computing, enabling the possibility of solving the NPB in three dimension for huge and complicated systems while still providing an extensible interface.

### 1.2.3. Algorithm theoretical background

For most problems of interest, like crystallization properties of colloidal particles, one is not interested in the electrostatic potential in the inner region of the particle. But to fulfill the continuity of the electrostatic potential on the surface and to satisfy Gauss' law, the solution of Poisson's equation in the inner region is needed, which might take a large amount of computation time. The numerical cost could be decreased drastically by not solving Poisson's equation but instead applying an appropriate boundary condition on the particle's surface. Common assumptions are to model particles at constant surface potential (which physically describes a perfect conductor) or with a constant surface charge density.

While for some systems these assumptions hold perfectly true, one has to use more sophisticated methods to determine the correct boundary conditions for other ones. For a single spherical particle, one can use both types of boundary conditions to get the right solution of the NPB, while if considering two close spheres at a distance where the double-layers start overlapping, neither the potential on the surface is constant nor can the value of the electric field be determined by the surface charge density alone, as the surface charge of the second sphere will give a contribution too. It is in such geometrical setups, where our algorithm offers the possibility to determine the correct boundary conditions and also to include the effects of a jump in the dielectric permittivity on the surface  $S$ .

Using Neumann boundary conditions, we determine the electric field on the bound-

ary surface caused by the charge distribution  $\rho(\mathbf{r})$ . Within the Poisson–Boltzmann description the charge density of the micro-ions is related to the electrostatic potential  $\phi$ , so that we obtain an implicit definition of the electric field on the surface,

$$\mathbf{E}_S(\mathbf{r}) = -\nabla\phi_S(\mathbf{r}) = f(\rho(\phi)), \quad r \in S. \quad (1.2.1)$$

Here,  $\phi_S$  and  $\mathbf{E}_S$ , denote the values of the electric potential and field on the boundary surface respectively, while  $\phi$  denotes the potential in the whole domain. Equation 1.2.1 is the starting point for our iterative approach, which will be presented in more detail in chapter 3.4.



## 2. Theoretical background

### 2.1. Classical electrostatics

As the electrostatic interaction between ions in an electrolyte solution shall be treated on a mean field level in chapter 2.2, a short overview of the basic equations of classical electrostatics [40] will be presented here. Note that all values are given in terms of Système international d'unités (SI) units [67].

The force  $\mathbf{F}_p$  acting on a point charge  $q_p$  at position  $\mathbf{r}$  is directly proportional to the charge,

$$\mathbf{F}_p(\mathbf{r}) = q_p \mathbf{E}(\mathbf{r}). \quad (2.1.1)$$

The electric field  $\mathbf{E}$  is given by the generalized Coulomb's law,

$$\mathbf{E}(\mathbf{r}) = \frac{1}{4\pi\varepsilon} \int \rho(\mathbf{r}') \frac{(\mathbf{r} - \mathbf{r}')}{|\mathbf{r} - \mathbf{r}'|^3} d\mathbf{r}', \quad (2.1.2)$$

where we introduced the charge density  $\rho$  and the integral has to be performed over the whole space. The dielectric permittivity is defined as

$$\varepsilon \equiv \varepsilon_0 \varepsilon_r, \quad (2.1.3)$$

where  $\varepsilon_0$  is the vacuum dielectric permittivity and  $\varepsilon_r$  is called the relative dielectric constant characterizing a certain material. Coulomb's law and the fact that the electrostatic field is conservative can be expressed differential form,

$$\nabla \cdot \mathbf{E} = \frac{\rho}{\varepsilon} \quad (2.1.4)$$

$$\nabla \times \mathbf{E} = 0, \quad (2.1.5)$$

where eq. 2.1.5 directly follows from eq. 2.1.2.

Using Gauss's theorem for integrating eq. 2.1.4 over a volume  $V$  with a surface  $S$  enclosing a charge  $Q$  results in Gauss's law of electrostatics:

$$\int_S \mathbf{E} d\mathbf{S} = \frac{Q}{\varepsilon} \quad (2.1.6)$$

According to eq. 2.1.5 the curl of the electric field is zero, so that we can write the  $\mathbf{E}$  as gradient of a scalar function  $\Phi$ ,

$$\mathbf{E} \equiv -\nabla \Phi, \quad (2.1.7)$$

## 2. Theoretical background

---

where we introduced the electrostatic potential  $\Phi(\mathbf{r})$ . The electrostatic potential can be determined up to an additive constant by integrating the electric field along an arbitrary path between two points  $\mathbf{p}_1$  and  $\mathbf{p}_2$ :

$$\Phi(\mathbf{p}_2) = \int_{\mathbf{p}_1}^{\mathbf{p}_2} \mathbf{E}(\mathbf{r}) \cdot d\mathbf{r} + \Phi(\mathbf{p}_1) \quad (2.1.8)$$

Combining eqs. 2.1.4 and 2.1.7 results in Poisson's equation:

$$\nabla^2 \Phi(\mathbf{r}) = -\frac{\rho(\mathbf{r})}{\varepsilon} \quad (2.1.9)$$

### 2.1.1. Surface charges and dipoles

A common problem of electrostatics is the determination of the potential or the field due to a given surface charge distribution  $\sigma(\mathbf{r})$ .

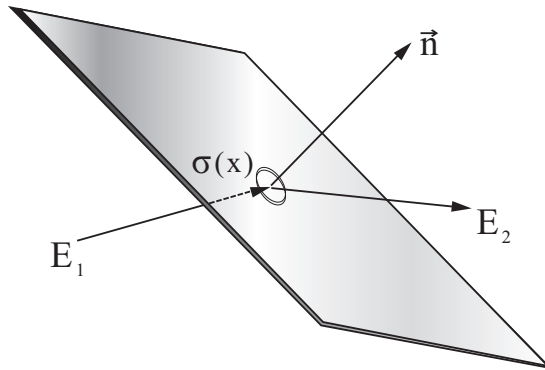


Figure 2.1.1.: A surface charge density  $\sigma$  causes a jump in the normal component of the electric field

Imagine a charged surface  $S$  like shown in figure 2.1.1, dividing two regions 1 and 2 of dielectric permittivity  $\varepsilon_1$  and  $\varepsilon_2$ , where the electric field takes  $\mathbf{E}_1(\mathbf{r})$  and  $\mathbf{E}_2(\mathbf{r})$  on the upper and lower face, respectively. The surface normal  $\hat{\mathbf{n}}$  points from region 1 to region 2. Gauss's theorem for a thin box at the surface directly yields a discontinuity for the normal component of the electric field,

$$(\varepsilon_1 \mathbf{E}_1(\mathbf{r}) - \varepsilon_2 \mathbf{E}_2(\mathbf{r})) \cdot \hat{\mathbf{n}} = -\sigma(\mathbf{r}), \quad (2.1.10)$$

in contrast it can easily been shown that the tangential component is continuous.

Another very common problem of electrostatics is that of polarization. The electric permittivity is a measure of how an electric field affects, and is affected by, a dielectric medium. The displacement field  $\mathbf{D}$  represents very generally how an electric field acts

on electrical charges in a medium. The mean effects of an external field in the medium itself are charge displacement (inducing a dipole moment) and orientation of permanent dipoles in the medium along the field lines. For linear, homogeneous, isotropic materials the dielectric tensor reduces to a scalar quantity  $\epsilon$ ,

$$\mathbf{D}(\mathbf{r}) = \epsilon \mathbf{E}(\mathbf{r}). \quad (2.1.11)$$

The dielectric permittivity is then defined as product of the vacuum dielectric permittivity  $\epsilon_0$  and the relative dielectric permittivity  $\epsilon_r$  (eq. 2.1.3), relating the material susceptibility  $\chi$  and the vacuum permittivity:

$$\mathbf{D} = \epsilon_0 \mathbf{E} + \mathbf{P} = \epsilon_0 (1 + \chi) \mathbf{E} = \epsilon_0 \epsilon_r \mathbf{E}, \quad (2.1.12)$$

where  $\mathbf{P}$  is the macroscopic polarization of the medium.

Eq. 2.1.10 already describes the jump of the electric field across the material surface due to the dielectric interface. But while in the case of non-polarizable materials this jump is only due to surface charges and the potential is continuous across the interface, for polarizable materials also the polarization field  $\mathbf{P}$  will give a contribution. Equation 2.1.10 gives a general description of how to solve such a kind of system having jump of the dielectric constant across a surface, but in order to do so the electric field on both sides 1 and 2 has to be known. For many cases it is appropriate to replace this two domain problem by an equivalent one without the dielectric jump. This can indeed be achieved by introducing an additional fictitious charge on the right hand side of eq. 2.1.10, the induced charge density  $\sigma_{\text{ind}}$ .

This method is equivalent to the well-known method of image charges that simplifies the solution of the Green's function in many cases. With this method it is sufficient to know the value of the electric field on one side of the interface and, thus, can reduce drastically the numerical effort during calculations. The method of an induced charge density at dielectric interfaces will therefore be used in our algorithm to include dielectric contrast.

## 2.2. Derivation of the Poisson Boltzmann Equation

### 2.2.1. Statistical mechanics description of the system

To describe the steady-state distribution of  $N$  ions in an electrolyte solution (see chapter 1.2.1), we start with the total energy in the system, given by the time independent Hamiltonian function

$$\mathcal{H}(\mathbf{q}, \mathbf{p}) = \frac{\mathbf{p}^2}{2m} + V(\mathbf{q}), \quad (2.2.1)$$

where  $\mathbf{q} = \mathbf{r}_1, \dots, \mathbf{r}_N$  are the generalized coordinates and  $\mathbf{p} = \mathbf{p}_1, \dots, \mathbf{p}_N$  are the generalized momenta. The ion mass  $m$  is not of any interest in our calculations, as it will not influence the ion distribution. One can show [54] that the canonical partition function,

$$Z = \text{Tr} \exp(-\beta \mathcal{H}), \quad (2.2.2)$$

## 2. Theoretical background

---

then factorizes into a kinetic (momentum) part,  $Z_{\text{kin}} = \text{Tr} \exp(-\beta \mathcal{H}_{\text{kin}})$ , and a configurational one,  $Z_{\text{cfg}} = \text{Tr} \exp(-\beta \mathcal{H}_{\text{cfg}})$ , where we introduced the inverse temperature  $\beta = 1/k_B T$ , with  $k_B$  being the Boltzmann constant and  $T$  the absolute temperature. The Helmholtz free energy,

$$F = -\frac{1}{\beta} \ln Z, \quad (2.2.3)$$

from which we will later obtain the ion distribution function, then also consists of a kinetic part,  $F_{\text{kin}}$ , and a configurational part  $F_{\text{cfg}}$ .

Assuming that all interactions in the system are of electrostatic nature (Debye approximation), We will now calculate the potential energy of the  $N$  ions in the field created by themselves. The strategy can be summarized as follows:

1. Start with the empty system and bring a single ion with, say, index 1, from infinity to its position  $\mathbf{r}_1$ . This will cost no energy at all as there are still no other ions, and thus, the potential can still be assumed to be zero without loss of generality.
2. Bringing a second ion to its position  $\mathbf{r}_2$ , it will interact with the potential of the first particle,

$$\Psi(\mathbf{r}_2) = -\frac{z_1 e}{4\pi\epsilon} \frac{1}{|\mathbf{r}_2 - \mathbf{r}_1|}. \quad (2.2.4)$$

3. As the Poisson equation is linear, the third ion we are insert into the system interacts with the linear superposition of the particles located at  $\mathbf{r}_1$  and  $\mathbf{r}_2$ :

$$\Psi(\mathbf{r}_3) = -\frac{z_1 e}{4\pi\epsilon} \frac{1}{|\mathbf{r}_3 - \mathbf{r}_1|} - \frac{z_2 e}{4\pi\epsilon} \frac{1}{|\mathbf{r}_3 - \mathbf{r}_2|} \quad (2.2.5)$$

4. Bring step by step all  $N$  particles to the system and sum up their single particle energy  $\epsilon_i = z_i e \Phi$  when bringing them in.

Finally, this procedure will end up with an expression for the potential energy,

$$\epsilon_{\text{pot}} = \sum_{i=2}^N \sum_{k=1}^{i-1} \frac{1}{4\pi\epsilon} \frac{z_i z_k e^2}{|\mathbf{r}_k - \mathbf{r}_i|} = \frac{1}{2} e^2 \sum_{i=1}^N \sum_{j \neq k=1}^N z_i z_k \Psi(\mathbf{r}_i, \mathbf{r}_k) \quad (2.2.6)$$

Note that in this procedure we explicitly made use of modeling point charges and avoided the diverging self-energy via the restriction  $i \neq j$  during the summation, that can be performed in arbitrary order due to the linearity of the Poisson equation.

If now - for the sake of simplicity during the calculation - we include the self-energy, we have to smear out the charges, as then the self-energy contributes a large, but finite value. As standard textbooks of electrostatics show, these self-energy contributions add a constant bias to the potential energy and due to gauge invariance of the electrostatic potential we can instead of eq. 2.2.6 use:

$$\epsilon_{\text{pot}} = \frac{1}{2} e^2 \sum_{i=1}^N \sum_{k=1}^N z_i z_k \Psi(\mathbf{r}_i, \mathbf{r}_k) \quad (2.2.7)$$

Having determined the potential energy, we now can turn to the calculation of the kinetic part of the free energy,  $F_{\text{kin}} = U - TS$ , where  $U$  is the internal energy and  $S$  is the configurational contribution to the entropy.

In order to calculate  $U$  and  $S$  as ensemble averages, we need the canonical probability density of a (configurational) micro-state  $\{\mathbf{r}_1, \dots, \mathbf{r}_N\}$  of the  $N$  ions, which is given by

$$p(\mathbf{r}_1, \dots, \mathbf{r}_N) = \frac{1}{Z_{\text{cfg}}} \exp(-\beta \epsilon_{\text{pot}}(\mathbf{r}_1, \dots, \mathbf{r}_N)), \quad (2.2.8)$$

where the configurational part of the canonical partition function is given by

$$Z_{\text{cfg}} = \text{Tr} \exp(-\beta \mathcal{H}_{\text{cfg}}) = \text{Tr} \exp(-\beta V(\mathbf{r})). \quad (2.2.9)$$

The configurational entropy  $S$  then is a logarithmic measure for the density of states, which, introducing the trace of all (configurational) micro-states, can be written as

$$\begin{aligned} S &= -k_B \text{Tr}(p \ln p) \\ &= -k_B \int_V d\mathbf{r}_1 \dots d\mathbf{r}_N d\mathbf{r}'_1 \dots d\mathbf{r}'_N p(\mathbf{r}_1, \dots, \mathbf{r}_N) p(\mathbf{r}'_1, \dots, \mathbf{r}'_N). \end{aligned} \quad (2.2.10)$$

The configurational contribution to the internal energy  $U$  then is defined as the ensemble average  $\langle \epsilon_{\text{pot}} \rangle$  of the potential energy, that using eq. 2.2.7 is given by

$$\begin{aligned} U &= \langle \epsilon_{\text{pot}} \rangle = \text{Tr}(p \epsilon_{\text{pot}} p) \\ &= \frac{1}{2} e^2 \int_V d\mathbf{r}_1 \dots d\mathbf{r}_N d\mathbf{r}'_1 \dots d\mathbf{r}'_N p(\mathbf{r}_1, \dots, \mathbf{r}_N) p(\mathbf{r}'_1, \dots, \mathbf{r}'_N) \sum_{i=1}^N \sum_{k=1}^N z_i z_k \Psi(\mathbf{r}_i, \mathbf{r}'_k) \end{aligned} \quad (2.2.11)$$

Using this expression for the configurational internal energy one could directly find the configurational Helmholtz free energy,

$$F_{\text{cfg}} = U - TS. \quad (2.2.12)$$

The difficult part is the calculation of the  $N$ -body probability density in eq. 2.2.8 due to the coupling of  $\Psi(\mathbf{r}_i, \mathbf{r}_k)$ , for which no analytical solution is known.

### 2.2.2. The mean-field approximation

In order to proceed with the calculations we now have to do the basic approximation, upon which the Poisson–Boltzmann theory is based on. The *mean-field* approximation replaces the probability density  $p$  given by eq. 2.2.8 by  $p^*$ , neglecting all ion correlations. In other words we assume that the probability of finding an ion at a position  $\mathbf{r}$  is only dependent on the total ion number density, that is normalized given by

$$p_1(\mathbf{r}) = \frac{n(\mathbf{r})}{N}, \quad (2.2.13)$$

## 2. Theoretical background

---

where the index 1 denotes that it is a single particle property and the resulting probability density then follows as a product of these single particle densities,  $p^* = p_1(\mathbf{r}_1) \cdots p_1(\mathbf{r}_N)$ . The resulting configurational entropy then is given by the product of these single particle densities,

$$\begin{aligned} S &= -k_B \text{Tr}(p^* \ln p^*) \\ &= -k_B \int_V d\mathbf{r}_1 \dots d\mathbf{r}_N (p_1(\mathbf{r}'_1) \cdots p_1(\mathbf{r}'_N)) \ln (p_1(\mathbf{r}'_1) \cdots p_1(\mathbf{r}'_N)) \\ &= Nk_B \int_V d\mathbf{r} p_1(\mathbf{r}) \ln p_1(\mathbf{r}) \\ &= -k_B \int_V d\mathbf{r} n(\mathbf{r}) \ln \frac{n(\mathbf{r})}{N}. \end{aligned} \quad (2.2.14)$$

Similarly we can simplify the ensemble average of the potential energy in eq. 2.2.11 using the definition of  $p^*$ ,

$$\begin{aligned} \langle \epsilon_{pot} \rangle &= \frac{1}{2} e^2 \int_V d\mathbf{r} d\mathbf{r}' p_1(\mathbf{r}) p_1(\mathbf{r}') \sum_{i=1}^N \sum_{k=1}^N z_i z_k \Psi(\mathbf{r}_i, \mathbf{r}'_k) \\ &= \frac{1}{2} e^2 \int_V d\mathbf{r} d\mathbf{r}' \frac{n(\mathbf{r}) n(\mathbf{r}')}{N^2} \sum_{i=1}^N \sum_{k=1}^N z_i z_k \Psi(\mathbf{r}_i, \mathbf{r}'_k). \end{aligned} \quad (2.2.15)$$

Combining the kinetic part of the free energy, which for the  $N$  ions is given by a functional dependency of the ion mass  $m$  and the inverse temperature  $\beta$ ,

$$F_{\text{kin}} = N\beta f(m, \beta), \quad (2.2.16)$$

with the configurational contribution (eq. 2.2.14) to the entropy with the configurational free energy in the mean field approximation (eq. 2.2.15), we now get the functional for the Poisson–Boltzmann free energy,

$$\begin{aligned} F_{\text{PB}}(n(\mathbf{r})) &= \frac{1}{2} e^2 \int_V d\mathbf{r} d\mathbf{r}' \frac{n(\mathbf{r}) n(\mathbf{r}')}{N^2} \sum_{i=1}^N \sum_{k=1}^N z_i z_k \Psi(\mathbf{r}_i, \mathbf{r}'_k) \\ &\quad + \beta \int_V d\mathbf{r} n(\mathbf{r}) \left[ \ln \frac{n(\mathbf{r})}{N} + f(m, T) \right] \end{aligned} \quad (2.2.17)$$

The Bogoliubov inequality for the mean-field approximation in the Gibbs ensemble gives an upper bound for any free energy approximation [54],

$$F \leq F_{\text{PB}}. \quad (2.2.18)$$

So we can determine the ion number density  $n(\mathbf{r})$  by minimizing the functional 2.2.17 taking into account the following two constraints:

1. The total number of ions in the system,  $N$ , is a fixed parameter.  
As the variation is performed in  $n(\mathbf{r})$ , one has to make sure that  $\int_V d\mathbf{r} n(\mathbf{r}) = N$ .
2. The ion number density  $n(\mathbf{r})$  is related to the charge density  $\rho(\mathbf{r})$  of the Poisson equation (eq. 2.1.9) via  $\rho(\mathbf{r}) = \sum_i e z_i n_i(\mathbf{r})$ , where the index denotes the  $i$ -th ion species.

The first constraint can be satisfied by introducing the Lagrange multiplier  $\mu$ , which we will identify as the chemical potential. The Poisson–Boltzmann free energy functional then reads [21],[13]:

$$F_{\text{PB}}(n(\mathbf{r})) = \frac{1}{2} e^2 \int_V d\mathbf{r} d\mathbf{r}' \frac{n(\mathbf{r})n(\mathbf{r}')}{N^2} \sum_{i=1}^N \sum_{k=1}^N z_i z_k \Psi(\mathbf{r}_i, \mathbf{r}'_k) + \beta \int_V d\mathbf{r} n(\mathbf{r}) \left[ \ln \frac{n(\mathbf{r})}{N} + f(m, T) \right] + \mu \int_V d\mathbf{r} \left[ n(\mathbf{r}) - \frac{N}{V} \right] \quad (2.2.19)$$

Minimizing eq. 2.2.19 with a variation in  $n(\mathbf{r})$  results in

$$0 \equiv \frac{\delta F_{\text{PB}}}{\delta n(\mathbf{r})} = \mu + e^2 \int_V d\mathbf{r}' \frac{n(\mathbf{r}')}{N} \sum_{i=1}^N \sum_{k=1}^N z_i z_k \Psi(\mathbf{r}_i, \mathbf{r}'_k) + \beta \int_V d\mathbf{r} n(\mathbf{r}) \left[ \ln \frac{n(\mathbf{r})}{N} + f(m, T) + 1 \right] \quad (2.2.20)$$

We can identify the second term on the right hand side of eq. 2.2.20 with the electrostatic potential

$$\Phi(\mathbf{r}) = \int_V d\mathbf{r} \sum_{i=1}^N z_i e n_i(\mathbf{r}) \Psi(\mathbf{r}_i, \mathbf{r}') = \rho(\mathbf{r}) \Psi(\mathbf{r}_i, \mathbf{r}') , \quad (2.2.21)$$

where we used the volume charge density given by the second constraint, which is thus fulfilled. The minimization problem then simplifies to

$$0 = \mu + \int_V d\mathbf{r} \rho(\mathbf{r}) \Phi(\mathbf{r}) + \beta \int_V d\mathbf{r} n(\mathbf{r}) \left[ \ln \frac{n(\mathbf{r})}{N} + f(m, T) + 1 \right] . \quad (2.2.22)$$

Solving the latter expression for the number density of species  $i$ ,  $n_i(\mathbf{r})$ , finally yields

$$n_i(\mathbf{r}) = n_{0,i} \exp(-\beta z_i e \Phi(\mathbf{r})) , \quad (2.2.23)$$

where the quantities  $f(m, T)$  and  $\mu$  have been absorbed into the amplitude  $n_0 = n_0(m, T, \mu)$ . The proper value of  $n_0$  or the chemical potential  $\mu$  respectively, is then fixed by the first constraint,  $\int_V d\mathbf{r} n(\mathbf{r}) \equiv N$ . According to this definition,  $n_0$  is the ion number density at any point where  $\Phi(\mathbf{r}) = 0$ .

The electrostatic potential itself is given by the Poisson equation 2.1.9,

$$\nabla^2 \Phi(\mathbf{r}) = -\frac{\rho(\mathbf{r})}{\varepsilon} = \frac{e}{\varepsilon} \sum_i z_i n_i(\mathbf{r}),$$

## 2. Theoretical background

---

and, substituting the expression for the number ion density into the latter, finally yields the Poisson–Boltzmann equation,

$$\nabla^2 \Phi(\mathbf{r}) = \frac{e}{\varepsilon} \sum_i z_i c_i^{eq} \exp(-\beta z_i e \Phi(\mathbf{r})), \quad (2.2.24)$$

where we introduced the equilibrium concentration of the  $i$ -th ion species in the solution.

### 2.3. The reduced electrostatic potential

For numerical calculations and simulations it is convenient to rewrite the set of equations of relevance in dimensionless, so-called reduced, units. As we will see, it is quite convenient to introduce the reduced electrostatic potential  $\phi$  as

$$\phi(\mathbf{r}) = \frac{e}{k_B T \Phi(\mathbf{r})}. \quad (2.3.1)$$

The Poisson's equation then reads

$$\nabla^2 \phi(\mathbf{r}) = -\frac{e}{k_B T} \frac{\rho(\mathbf{r})}{e \varepsilon} = -\frac{e^2 \sum_i z_i c_i^{eq}}{k_B T \varepsilon_0 \varepsilon_r} n_i(\mathbf{r}). \quad (2.3.2)$$

We now introduce the Bjerrum length,

$$\ell_B = e^2 / (4\pi \varepsilon_0 \varepsilon_r k_B T), \quad (2.3.3)$$

which defines the length-scale at which the thermal energy equals the electrostatic interactions. Its value for water ( $\varepsilon_r \approx 80$ ) at room temperature ( $T \approx 300$  K) is approximately  $\ell_B \approx 0.71$  nm.

Poisson equation in reduced units can then be written as

$$\nabla^2 \phi(\mathbf{r}) = -4\pi \ell_B \rho(\mathbf{r}). \quad (2.3.4)$$

By inserting the reduced potential into eq. 2.2.24 we recover the Poisson–Boltzmann equation in reduced units,

$$\nabla^2 \phi(\mathbf{r}) = -4\pi \ell_B e \sum_i z_i c_i^{eq} \exp(-z_i \phi(\mathbf{r})). \quad (2.3.5)$$

For a symmetric  $z - z$  electrolyte ( $z_1 = z_2 = z$ ), the latter simplifies to

$$\nabla^2 \phi(\mathbf{r}) = \frac{\kappa^2}{z} \sinh(z\phi(\mathbf{r})), \quad (2.3.6)$$

where we introduced the Debye screening length (explained in more detail in chapter 2.4.1),

$$\frac{1}{\kappa} = \left( \frac{\varepsilon k_B T}{\sum_i (z_i e)^2 c_i^{eq}} \right)^{\frac{1}{2}} = \frac{1}{\sqrt{4\pi \ell_B \sum_i z_i^2 c_i^{eq}}}, \quad (2.3.7)$$

Comparing with Poisson's equation (2.3.4), we can then determine the effective ion density  $\rho(\mathbf{r})$  in the solution,

$$\begin{aligned}\rho(\Phi(\mathbf{r})) &= e \sum_i z_i c_i^{eq} \exp(-z_i \Phi(\mathbf{r})) \\ &= \frac{\kappa^2 z}{4\pi\ell_B} \sinh(-z\Phi(\mathbf{r})),\end{aligned}\quad (2.3.8)$$

where the latter expression is valid only for the case of a symmetric  $z-z$  electrolyte.

## 2.4. Debye-Hückel theory

A first theoretical treatment of electrostatic interactions of electrolytes in solution using Poisson Boltzmann theory was given by P. Debye and E. Hückel in 1923 [18]. In their work they determined the electrostatic energy to get the correct activity coefficients. This was of interest as for weak electrolytes theories available at that time were predicting freezing and melting points that contradicted experimental observations.

As Bjerrum showed in 1909 [15] strong electrolytes can be treated as fully dissociated up to very high concentrations, and even for weak electrolytes at intermediate concentrations nearly no effects of undissociated ions are seen. Limiting their analysis to monovalent ( $z = 1$ ) symmetric electrolytes (like NaCl or KCl) they showed a way to calculate the electrostatic energy of a single ion in the solution using the mean-field potential of all other ions. In the general case this is given more accurately by the nonlinear Poisson-Boltzmann equation. Putting these assumptions into eq. 2.3.5 and using the spherical symmetry of this certain ion ( $\phi(\mathbf{r}) = \phi(r)$ ), this yields

$$\nabla^2 \phi(\mathbf{r}) = \kappa^2 \sinh(\phi(\mathbf{r})) \quad (2.4.1)$$

Here we introduced the characteristic length

$$\frac{1}{\kappa} = \left( \frac{\varepsilon_0 \varepsilon_r k_B T}{2 \sum_i c_i^\infty (z_i e)^2} \right)^{1/2} \equiv \lambda_D \quad (2.4.2)$$

as Debye and Hückel proposed in their paper, which is nowadays referred to as the Debye screening length.

Assuming that the electrostatic field is only relevant at distances  $r \gg a$ , where  $a$  is the diameter of the ion, the potential  $\phi(r)$  will decrease significantly with growing distance  $r$ . Performing a series expansion it is then very reasonable to approximate  $\sinh(\phi(\mathbf{r})) \approx \phi(\mathbf{r})$  for small values of the electrostatic potential,  $\phi \ll 1$ , which simplifies eq. 2.4.1 to:

$$\nabla^2 \phi(\mathbf{r}) = \kappa^2 \phi(\mathbf{r}) \quad (2.4.3)$$

### 2.4.1. The Debye screening length

We now want to examine the physical properties of the screening length in eq. 2.4.2. Inserting the numbers for water at room temperature ( $25^{\circ}\text{C}$ ) and measuring the molar concentration  $c_i$  of ion species  $i$  in (Mol/L) we get

$$\lambda_D = \frac{0.303}{\sqrt{I}} \text{ nm}, \quad (2.4.4)$$

where the *ionic strength* of the electrolyte solution is defined as

$$I = \frac{1}{2} \sum_{i=1}^N c_i z_i^2. \quad (2.4.5)$$

To get a better understanding of this length scale one can imagine an electrode of potential  $\phi = 0$  put in an electrolyte solution at potential  $\phi$ . Using eq. 2.4.3 and letting  $z$  denote the axis perpendicular to the electrode, a possible solution is:

$$\phi(z) = \phi_0 \exp(-\kappa z) \quad (2.4.6)$$

In this general solution the electrostatic potential of the single ion drops off in an exponential manner with a characteristic length  $\lambda_D = 1/\kappa$ . As the right hand side of eq. 2.4.3 denotes the source term of Poisson equation (2.3.4) we can now calculate the ion density

$$\rho(z) = -4\pi\ell_B\kappa^2\phi(z) \exp(-\kappa z) \quad (2.4.7)$$

According to eq. 2.4.7 the characteristic length  $\lambda_D$  is the distance at which the ion density dropped to  $1/e$  of its original value.

### 2.4.2. General solution of the linearized PBE

Having in mind the properties of the Debye screening length we now want to determine the electrostatic potential around the highlighted spherical ion of charge  $Q$ .

It is appropriate to introduce polar coordinates for eq. 2.4.3 which yields:

$$\frac{1}{r^2} \frac{\partial}{\partial r} \left( r^2 \frac{\partial \phi(r)}{\partial r} \right) = \kappa^2 \phi(r) \quad (2.4.8)$$

The general solution of eq. 2.4.8 is

$$\phi(r) = A \frac{e^{-\kappa r}}{r} + A' \frac{e^{\kappa r}}{r} \quad (2.4.9)$$

Asuming that the electrolyte is in equilibrium at infinity, the electrostatic potential asymptotically goes to zero,  $\lim_{r \rightarrow \infty} \phi(r) = 0$ , such that we can determine the constant  $A' = 0$ . According to [18] we can split the following calculation into two parts: the first where we assume that the size of the ions is negligible and will deliver the limit of infinite dilution, and a second part where the ions have finite size.

### Negligible ion radius

For the absence of counter-ions, which is nearly fulfilled for small distances  $r$ , the potential will look like that of a point charge,

$$\phi(r) = \ell_B \frac{Q}{r}. \quad (2.4.10)$$

The constant  $A$  can be determined by  $A = \ell_B Q$  which transforms eq. 2.4.9 to

$$\phi(r) = \ell_B Q \frac{e^{-\kappa r}}{r} = \ell_B \frac{Q}{r} - \ell_B \frac{Q - e^{-\kappa r}}{r} \quad (2.4.11)$$

where we split the potential into the two contributions, the first being the potential of a point charge and the second being the contribution of all surrounding ions to its potential. For small values of  $r$  the latter gives a contribution

$$-\ell_B Q \kappa.$$

The potential energy that the ion contributes to its surrounding ions can then be written as

$$u = -\ell_B Q^2 \kappa \quad (2.4.12)$$

Using classical electrostatics the total potential energy  $U$  of the system consisting of  $N$  ions can be written as sum of point-like charges  $Q_i$  multiplied with the potential  $\phi_i$  at their positions:

$$U = v \frac{1}{2} \sum_i Q_i \phi_i \quad (2.4.13)$$

As the system consists of  $N$  positive ions with potential difference  $-\ell_B Q \kappa$  and  $N$  negative ions with potential difference  $\ell_B Q \kappa$  the total energy is

$$U = \frac{NQ}{2} (-Q \ell_B \kappa) - \frac{NQ}{2} (Q \ell_B \kappa) = -NQ^2 \ell_B \kappa \quad (2.4.14)$$

### Finite ion radius

As we stated in eq. 2.4.4 the characteristic length for realistic salt concentrations can easily reach molecular dimensions. In such cases it is not appropriate to use point charges, but rather we have to deal with the finite size of ions. Continuing on the same line of the mean-field approach we introduce a radius  $a$  which defines a sphere with an a priori different dielectric permittivity  $\epsilon$ , in whose center a point charge is located. The inner part of the sphere can be described using the Bjerrum length  $\ell_B^{in}$ . In the mean-field description the radius  $a$  obviously is not identical to the ion size but defines the mean distance to which other ions can approach. For symmetric salt systems this radius is quite near to what one would think of as the ion radius, but there still might be some differences, e.g. due to solvation effects. In many experimentally relevant situations this

## 2. Theoretical background

---

is a reasonable approximation. Recalling eq. 2.4.9 we still have to determine the constant  $A$  for the potential outside the sphere,

$$\phi(r) = A \frac{e^{-\kappa r}}{r} \quad (2.4.15)$$

while in the inside of the sphere we have to solve a problem similar to the one above, with a point charge sitting in the center:

$$\varpi(r) = \ell_B \frac{Q}{r} + B \quad (2.4.16)$$

The constants  $A$  and  $B$  can then be determined using the continuity conditions at the sphere's surface,

$$\begin{aligned} \phi(a) &= \varpi(a) \\ \left( \frac{d\phi r}{dr} \right)_{r=a} &= \left( \frac{d\varpi r}{dr} \right)_{r=a} \end{aligned} \quad (2.4.17)$$

which yield the system of linear equations

$$A \frac{e^{-\kappa a}}{a} = \ell_B \frac{Q}{a} + B \quad (2.4.18a)$$

$$A e^{-\kappa a} \frac{1 + \kappa a}{a^2} = \ell_B \frac{Q}{a^2} \quad (2.4.18b)$$

from which the constants  $A$  and  $B$  can be determined to be

$$A = \ell_B Q \frac{e^{\kappa a}}{1 + \kappa a} , \quad B = -\ell_B^{in} Q \frac{\kappa}{1 + \kappa a} \quad (2.4.18c)$$

Note that the value of  $B$  is the potential at the center of the sphere generated by the ions around it. So again we can write the energy of a positive ion:

$$u = -\ell_B Q^2 \kappa \frac{1}{1 + \kappa a} \quad (2.4.19)$$

In the limit of dilute solutions ( $\kappa \rightarrow 0$ ) we get the same result as in eq. 2.4.12 while for large concentrations ( $\kappa \gg 1$ ) the dominant characteristic length becomes  $a$  as the energy goes like

$$u = -\ell_B \frac{Q^2}{a}.$$

Like in the previous case we can then sum up positive and negative ions to get the total energy of the system:

$$U = -\frac{N}{2} Q^2 \ell_B \kappa \left[ \frac{1}{1 + \kappa a_1} + \frac{1}{1 + \kappa a_2} \right] \quad (2.4.20)$$

Here we already introduced different radii for positive and negative charged ions, as it is generally appropriate (e.g. KCl).

## 2.5. Effective interactions between colloidal particles

We now want to determine the potential of a dispersion of  $N_0$  charged, spherical colloidal particles dissolved in a polar solvent of dielectric constant  $\varepsilon$ . The colloidal particles are treated as a hard spheres of radius  $R$  and carrying a charge  $Ze$  ( $|Z| \gg 1$ ). The dissolved ions are modeled as hard spheres as well, while their radius is assumed to be negligible,  $a \ll R$ , and their valency is supposed to be  $z$ . Furthermore the solution is assumed to be in thermodynamic equilibrium with a salt reservoir, which fixes the chemical potentials  $\mu_+$  and  $\mu_-$  of the micro-ions.

We can then describe the system in the so-called semi-grand canonical ensemble, which is characterized by the set  $\{N_0, \mu_+, \mu_-, V, T\}$  of variables, where the number  $N_0$  of colloids is fixed but the number of micro-ions is allowed to fluctuate. Coordinates of the colloids and the ions are denoted  $\{\mathbf{R}_i\}$  and  $\{\mathbf{r}_i\}$  respectively. Using the generalized coordinates  $\{\mathbf{q}\} = \{\{\mathbf{R}_i\}, \{\mathbf{r}_i\}\}$ , the Hamiltonian 2.2.1 reads:

$$\mathcal{H}(\mathbf{q}, \mathbf{p}) = \frac{\mathbf{p}^2}{2m} + V(\{\mathbf{R}_i\}, \{\mathbf{r}_i\}), \quad (2.5.1)$$

where we can skip the discussion of the first term on the right hand side as qualitatively it will give the same contribution as in section 2.2. The electrostatic interaction potential then can be split,

$$V(\{\mathbf{R}_i\}, \{\mathbf{r}_i\}) = V_{cc}(\{\mathbf{R}_i\}) + V_{ci}(\{\mathbf{R}_i\}, \{\mathbf{r}_i\}) + V_{ii}(\{\mathbf{r}_i\}), \quad (2.5.2)$$

where  $V_{cc}$ ,  $V_{ci}$ , and  $V_{ii}$  are sums of pair potentials for colloid-colloid interactions, colloid-ion interactions, and ion-ion interactions respectively.

We now want to average out the degrees of freedom of the ion solution, so that the problem is effectively reduced to a one-component system of colloids dressed with their electric double layers. We define the semi-grand canonical partition function,

$$Z_{\text{cfg}} = \text{Tr} \exp(-\beta V_{cc}(\mathbf{r}) \Xi(\mu_+, \mu_-, V, T; \{\mathbf{R}_i\})), \quad (2.5.3)$$

where

$$\Xi = \text{Tr} \exp(-\beta (V_{ci}(\mathbf{R}, \mathbf{r}) + V_{ii}(\mathbf{r}) - \mu N)) \quad (2.5.4)$$

is the grand canonical partition function of the ions in the external potential  $\varsigma(\mathbf{r})$  of the poly-ions in a configuration  $\{\mathbf{R}_i\}$ ,

$$\varsigma(\mathbf{r}) = \sum_{i=1}^{N_0} \Psi(|\mathbf{r} - \mathbf{R}_i|). \quad (2.5.5)$$

Introducing the effective interaction between the colloidal particles dressed with the electrical double layer,

$$V_{\text{eff}}(\{\mathbf{R}_i\}) = V_{cc}(\{\mathbf{R}_i\}) + \Omega(\mu_+, \mu_-, V, T; \{\mathbf{R}_i\}) \quad (2.5.6)$$

## 2. Theoretical background

---

we can re-express eq. 2.5.3 as:

$$Z_{\text{cfg}} = \text{Tr} \exp(-\beta V_{\text{eff}}(\mathbf{R})). \quad (2.5.7)$$

Note, that the first term in the effective potential is the direct interaction of colloids, which is assumed to be pairwise additive, whereas the effective interaction is not, as it also includes a “volume” term, which is independent of the poly-ion coordinates.

In eq. 2.5.6, we introduced the grand potential,

$$\Omega = F - \mu N = U - TS - \mu N, \quad (2.5.8)$$

that can be evaluated by the methods of density-functional theory, similar to those used in section 2.2. If we limit ourselves to a mean-field approach (2.2.13), the grand potential function of the fluid can be re-expressed as a functional of the ion number densities  $n_+$  of the positive ions and  $n_-$  of the negative ions [33],

$$\Omega(n_+, n_-) = F(n_+, n_-) - \sum_{\nu} \int_V [\mu - \phi_{\nu}(\mathbf{r})] n_{\nu}(\mathbf{r}) d\mathbf{r}, \quad (2.5.9)$$

where  $\phi_{\nu}(\mathbf{r})$  denotes the external potential acting on a particle of species  $\nu = +, -$ . The free energy functional can then be split into a kinetic part representing the well known ideal gas contribution (which we referred to as the kinetic part of the entropy in eq. 2.2.16),

$$F^{id} = k_B T \int_V n_{\nu}(\mathbf{r}) (\ln[\Lambda^3 n_{\nu}(\mathbf{r})] - 1) d\mathbf{r} \equiv N \beta f(m, \beta) = F_{\text{kin}} \quad (2.5.10)$$

and a configurational part (2.2.17), which is also commonly referred to as excess contribution to the free energy,

$$F^{ex} \equiv F_{\text{cfg}} = F(\varsigma(\mathbf{r})). \quad (2.5.11)$$

However, the solution of the resulting variational problem for the densities  $n_{\nu}(\mathbf{r})$  in the multi-center potential (2.5.5) is a very formidable task and could, for example, be determined via molecular dynamics simulations [50].

Instead, we assume the inhomogeneities in the distribution of ions in the solution caused by the colloids to be weak, i. e. that correlation effects can be neglected. This is the case for a dilute system of colloids whose charge per volume,  $Ze/4\pi R^2$  is fairly small such that the electrostatic interactions are sufficiently screened on the length-scale of the mean free path. The ideal free energy functional (2.5.10) can then be expanded in the deviation of the local ion number density from its bulk value.

$$\Delta n_{\nu}(\mathbf{r}) = n_{z_{\nu}}(\mathbf{r}) - c_{\nu}^{eq}, \quad (2.5.12)$$

Expanding to the second order and including an interaction energy term resulting from Coulombic interactions (2.2.7), the intrinsic free energy functional of the ions can be

approximated as

$$F(n_+, n_-) = \sum_{\nu} \left( F^{id}(n(\mathbf{r}) = c_{\nu}^{eq}) + k_B T \ln[\lambda^3 c_{\nu}^{eq}] \int_V \Delta n_{\nu}(\mathbf{r}) d\mathbf{r} \right. \\ \left. + \frac{k_B T}{2c_{\nu}^{eq}} \int_V [\Delta n_{\nu}(\mathbf{r})]^2 d\mathbf{r} \right) + ze \Delta n(\mathbf{r}) \int_V \Psi(\mathbf{r}) d\mathbf{r}. \quad (2.5.13)$$

Inserting the latter expression into eq. 2.5.9 and replacing the chemical potential  $\mu$  of the ions by that of an ideal gas,

$$\mu = -k_B T \ln \left( \frac{V}{N \Lambda^3} \right), \quad (2.5.14)$$

we now can minimize the grand potential (2.5.9) with variation of the ion number density, resulting in:

$$0 \equiv \frac{\delta \Omega}{\delta n_{\nu}(\mathbf{r})} = k_B T \frac{\Delta n_{\nu}(\mathbf{r})}{c_{\nu}^{eq}} + z_{\nu} e \int_V \Psi(\mathbf{r}) d\mathbf{r} + \phi_{\nu}(\mathbf{r}) \quad (2.5.15)$$

The colloidal particles shall now be treated as fixed point charges (we will recover the finite radius later), so that, limiting again to pure electrostatic interactions, we can re-express the external potential  $\phi_{\nu}(\mathbf{r}) = z_{\nu} e \Psi^{ext}(\mathbf{r})$ , where  $\Psi^{ext}(\mathbf{r})$  is the “external” electrostatic potential of the colloids acting on the ions.

Introducing the total electrostatic potential,

$$\Phi(\mathbf{r}) = \Psi(\mathbf{r}) + \Psi^{ext}(\mathbf{r}) = \int_V \frac{e}{4\pi\varepsilon} \frac{\sum_{\nu} z_{\nu} n_z(\mathbf{r}') + Z n^{ext}(\mathbf{r}')}{|\mathbf{r} - \mathbf{r}'|} d\mathbf{r}', \quad (2.5.16)$$

where the microscopic number density of the colloids is given by  $n^{ext}(\mathbf{r}) = \sum_i \delta(\mathbf{r} - \mathbf{R}_i)$ . Equation 2.5.15 then can be simplified to:

$$\Delta n_{\nu}(\mathbf{r}) = -\beta c_{\nu}^{eq} z_{\nu} e^2 \int_V \frac{e}{4\pi\varepsilon} \frac{\sum_{\nu} z_{\nu} n_z(\mathbf{r}') + Z n^{ext}(\mathbf{r}')}{|\mathbf{r} - \mathbf{r}'|} d\mathbf{r}', \quad (2.5.17)$$

To further simplify this problem, we limit to the case of having only counter-ions in the system, as it won’t affect the final interaction potential in its qualitative form. Fourier transformation and the application of the convolution theorem yields for both sides of the latter equation:

$$\hat{n}(\mathbf{k}) = -\ell_B \left( \frac{\hat{n}(\mathbf{k})}{k^2} + \frac{Z}{k^2} \sum_{i=1}^N \exp(-i\mathbf{k} \cdot \mathbf{R}_i) \right) \\ = -\frac{\kappa^2}{k^2 + \kappa^2} Z \sum_{i=1}^N \exp(-i\mathbf{k} \cdot \mathbf{R}_i), \quad (2.5.18)$$

## 2. Theoretical background

---

where we used the Debye screening length  $\kappa$  (2.4.2) and the Fourier transform

$$\begin{aligned}
\int d^3x \frac{1}{|\mathbf{x}|} e^{-i\mathbf{q}\cdot\mathbf{x}} &= \lim_{u \rightarrow 0} \int d^3x \frac{\exp(-u|\mathbf{x}|)}{|\mathbf{x}|} e^{-i\mathbf{q}\cdot\mathbf{x}} \\
&= \lim_{u \rightarrow 0} \int_0^\infty dr \int_{-1}^1 d\cos\vartheta 2\pi r^2 \frac{\exp(-ur)}{r} e^{-iqr \cos\vartheta} \\
&= 2\pi \lim_{u \rightarrow 0} \int_0^\infty dr \int_{-1}^1 ds r \exp(-r(u + iq)) \\
&= \frac{2\pi}{-iq} \lim_{u \rightarrow 0} \int_0^\infty dr [\exp(-r(u + iq))]_{-1}^1 \\
&= \frac{2\pi i}{q} \lim_{u \rightarrow 0} \left[ \frac{1}{u + iq} \right]_{-1}^1 \\
&= \frac{2\pi i}{q} \frac{2}{iq} \\
&= \frac{4\pi}{q^2}.
\end{aligned}$$

The inverse Fourier transform of eq. 2.5.18 reveals the counter-ion density profile,

$$n(\mathbf{r}) = \sum_{i=1}^N \frac{Z\kappa^2}{4\pi} \frac{\exp(-\kappa|\mathbf{r} - \mathbf{R}_i|)}{|\mathbf{r} - \mathbf{R}_i|} \equiv \sum_{i=1}^N n_i(\mathbf{r}). \quad (2.5.19)$$

The latter expression shows the total profile being a superposition of ion profiles related to each individual colloid.

We now want to re-introduce the finite radius  $R$  of the colloids, imposing that the ion number density must be zero whenever  $|\mathbf{r} - \mathbf{R}_i| < R$ . To ensure charge neutrality we must then normalize the single colloids counter-ion distributions, such that

$$\int_{|\mathbf{r} - \mathbf{R}_i| > R} n_i(\mathbf{r}) = |Z/z|, \quad (2.5.20)$$

which would be met by replacing the total charge  $Z$  of the colloidal particle by a renormalized charge,

$$Z' = Z \frac{\exp(\kappa R)}{1 + \kappa R}. \quad (2.5.21)$$

Note that the normalization condition 2.5.20 implicitly assumes that the electrical double layers of two distinguishable particles, have on average such a small overlap, that correlations in the ion distribution can be neglected. This is in keeping with the assumptions in the beginning of this section.

Using the linearity of Poisson equation, we can then formulate the resulting electric potential as superposition of single colloidal contributions,

$$\Phi(\mathbf{r}) = \sum_{i=1}^N \frac{Z'e}{4\pi\epsilon} \frac{\exp(-\kappa|\mathbf{r} - \mathbf{R}_i|)}{|\mathbf{r} - \mathbf{R}_i|} \equiv \sum_{i=1}^N \Phi_i(\mathbf{r}). \quad (2.5.22)$$

Substituting the latter expression for the potential and the density profile (2.5.19) into the definition of the grand potential, (2.5.9), we note that the effective interaction energy (2.5.6) can be written as

$$V_{\text{eff}}(\{\mathbf{R}_i\}) = \sum_{i=1}^N \sum_{j>1}^N v_{\text{eff}}(|\mathbf{R}_i - \mathbf{R}_j|) + V_0, \quad (2.5.23)$$

where the effective interaction potential  $v_{\text{eff}}(x)$  is electrostatic contribution to the well known Derjaguin–Landau–Verwey–Overbeek (DLVO) potential[19][71],

$$v_{\text{eff}}(x) = e^2 \frac{Z'^2}{4\pi\varepsilon} \frac{\exp(-\kappa x)}{x}, \quad (2.5.24)$$

where  $x$  denotes the separation of the particles' centers. Consequently, the pairwise additive forces acting between two colloids can be determined via

$$\begin{aligned} \mathbf{F}_{\text{eff}}(\mathbf{R} - \mathbf{R}') &= e^2 \frac{Z'^2}{4\pi\varepsilon} \left( \frac{\exp(-\kappa x)}{x^2} + \kappa \frac{\exp(-\kappa x)}{x} \right) \frac{(\mathbf{R} - \mathbf{R}')}{|\mathbf{R} - \mathbf{R}'|} \\ &= Z^2 \ell_B \left( \frac{\exp(\kappa R)}{1 + \kappa R} \right)^2 \left( \frac{\exp(-\kappa x)}{x^2} + \kappa \frac{\exp(-\kappa x)}{x} \right) \mathbf{e}_x. \end{aligned} \quad (2.5.25)$$

The structure-independent term  $V_0$  in (2.5.23) includes, among other contributions, the self-energy of the electric double layers. It has an important effects in the prediction of phase diagrams [70]. Since in this work we will focus on the analysis of forces between particles, we will neglect that contribution. Provided that co-ions are included in the definition of  $\kappa$  the functional form of the effective potential will stay the same and the assumption made in eq. 2.5.18, performing the Fourier using a single species of counter-ions only, is justified.

Pairwise additivity of inter-particle forces is not a strict consequence of the system's setup but follows directly of the quadratic expansion used in eq. 2.5.13. We will discuss in chapter 5 how well this approximation can be justified. For example it has been shown, that the quadratic expansion is inadequate for systems with highly charged colloids, as due to the strong attraction of the ions to the colloids, a layer of ions will become very tightly bound to the colloids surface, reducing the bare colloid's charge to an effective value  $Z_{\text{eff}}$ . Experimental measurements of the effective pair potential show good agreement with predicted curves for suitable chosen values of  $Z_{\text{eff}}$ .



# 3. Algorithm and implementation

## 3.1. The finite element method

As almost every physical problem can be modeled in terms of differential equations, and for most problems of interest analytical solutions are very rare due to geometric or material properties, numerical solution and stochastic simulation of physical systems has become very important over the last few decades, where computational power has grown rapidly. These methods provide new insight into physical processes and systems that could not be analyzed (at least not without simplifying assumptions, or, that could not be described in their whole complexity) before.

One of the most common methods to solve a mathematical model of a system is the method of finite elements, a general discretized variational solution method, which we will introduce here. One of the key ingredients is to transform the solution of the differential equation into a minimization problem, what is commonly called the Ritz-method [60], that can be transformed to the method of Galerkin [59] for reasons of simplification and numerical optimization.

To illustrate this method we consider a boundary value problem [65]  $Lu = f$ , with a differential operator  $L$  that we want to solve in a domain  $\Omega$ . Here,  $u$  is the solution and  $f$  defines sources of the field. Including the boundary conditions (we consider boundaries of Dirichlet and Neumann type) at  $\partial\Omega$  (see fig. 3.1(a)) and rewriting the problem as  $Lu - f = 0$ , we have to solve:

$$Lu - f = 0 \quad \text{in the whole domain } \Omega, \quad (3.1.1)$$

$$\nabla u \cdot \hat{\mathbf{n}} = g_n \quad \text{on boundaries } \partial\Omega \text{ of Neuman type}, \quad (3.1.2)$$

$$u = u_0 \quad \text{on boundaries } \partial\Omega \text{ of Dirichlet type}. \quad (3.1.3)$$

The basic idea of the method is to approximate the solution  $u(x)$  by a linear combination of well-known ansatz-functions (also called interpolation functions)  $\phi_i(x)$  and undetermined coefficients  $u_i$ ,

$$u \approx u^{(n)} = \sum_{i=1}^n u_i \phi_i(x), \quad (3.1.4)$$

where the interpolation functions  $\phi_i$  are assumed to be linear independent, smooth and continuously differentiable. Furthermore, we assume that they fulfill the boundary conditions. Using this approximation, we will introduce an error into the solution, called the

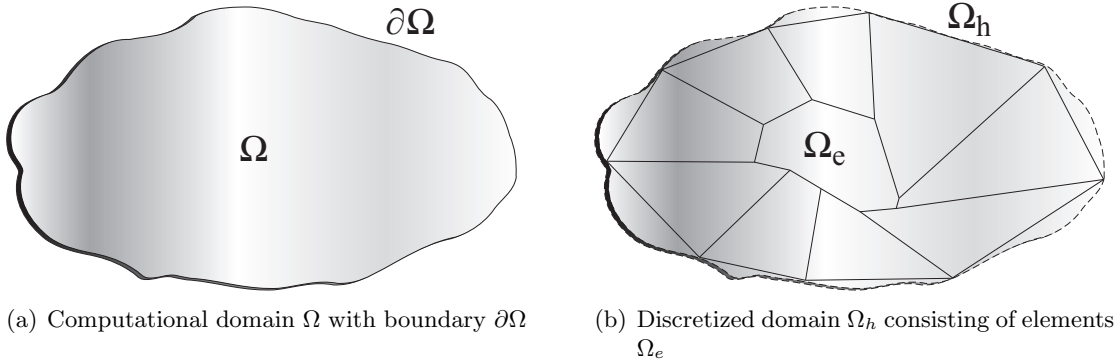


Figure 3.1.1.: A typical domain in which the boundary value problem shall be solved and its discretized equivalent for the finite element method

residual  $R$ ,

$$Lu^{(n)} - f = R, \quad (3.1.5)$$

and the coefficients  $u_i$  can be determined by minimizing the functional  $R^2$  (least-squares method) via variation in the  $u_i$ , so that at each integration point we have

$$\int_{\Omega} (Lu^{(n)} - f)^2 dV \rightarrow 0. \quad (3.1.6)$$

Minimization methods like the one given by eq. 3.1.6 are commonly referred to as methods of weighted residuals. Posing the problem in the weak formulation one obtains a Ritz variational problem, for which we multiply an arbitrary test-function  $v \in V \subseteq U$ , so that the coefficients can be determined by solving

$$\int_{\Omega} (Lu^{(n)} - f) v dV \rightarrow 0, \quad (3.1.7)$$

where 3.1.7 must be true for all test-functions  $v \in V$  and all ansatz-functions  $u \in U$ . We now have to choose an appropriate basis  $\phi_1, \phi_2, \dots, \phi_n \in U^{(n)}$ , and then determine the coefficients  $u_i$  in (3.1.7). Using Galerkin's method, we choose  $v = \phi_1, \phi_2, \dots, \phi_n$ . Note that it is often convenient to use test-functions which differ from zero only in certain regions, which will further simplify the resulting set of equations. Galerkin's method can then be formalized as an abstract problem posed in a weak formulation on a Hilbert space,  $U^{(n)}$ , namely, to find  $u^{(n)} \in U^{(n)}$  such that for all  $v \in U^{(n)}$ , the residual vanishes,  $R(u, v) = 0$ .

We will now limit ourselves to the analysis of elliptic partial differential equations, such that (3.1.1) reads

$$-\Delta u + au = f(u). \quad (3.1.8)$$

The weak formulation (3.1.7) can then be integrated by parts with respect to the boundary conditions (3.1.2) and (3.1.3), yielding

$$\int_{\Omega} \nabla u \nabla v + a u v - f(u) v dV + \int_{\partial\Omega} u_0 v + g_n v dS = 0. \quad (3.1.9)$$

If  $f$  is linear, the determination of the coefficients  $u_i$  results in a linear system of equations,

$$\sum_{j=1}^n A_{ij} u_j - F_i = 0, \quad (3.1.10)$$

where

$$A_{ij} = \int_{\Omega} \nabla \phi_i \nabla \phi_j + a \phi_i \phi_j \, dV + \int_{\partial\Omega} u_0 \phi_i \phi_j \, dS = 0. \quad (3.1.11)$$

We can now improve the approximation of  $u$  by dividing the domain  $\Omega$  into several sub-domains  $\Omega_e$ , which we will call finite elements. The finite elements as a whole will form a discretized copy  $\Omega_h$  of the original domain  $\Omega$ . Fig. 3.1.2 shows an example of how the approximation of a function  $u$  by polynomial functions  $u_h$  on each element can be achieved.

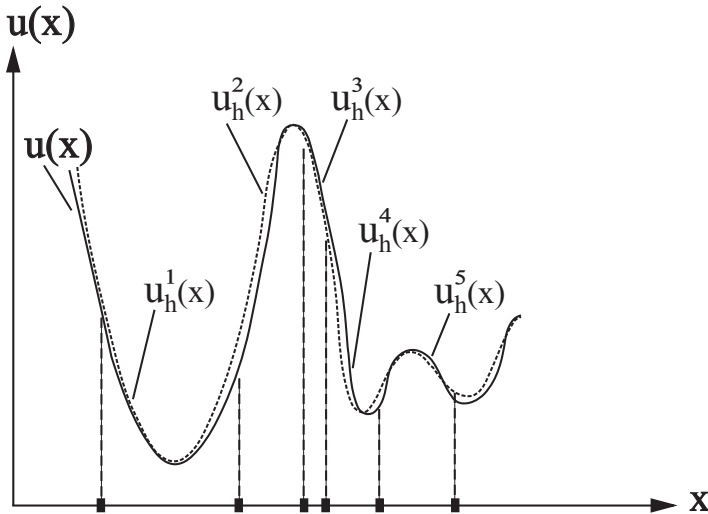


Figure 3.1.2.: A continuous function  $u$  can be approximated by e.g. polynomial ansatz-functions, which are defined on discrete elements.

The approximation is then achieved by interpolating the ansatz-functions between the boundary values given by the nodes (see fig. 3.1.3). For reasons of simplicity we will limit to linear interpolation schemes, but the extension to higher order interpolation is straight forward. On a given one-dimensional element  $e$ , the approximated function  $u_h^e$  is given by

$$u_h^e(\xi) = (1 - \xi)u_1^e + \xi u_2^e, \quad (3.1.12)$$

where we introduced the element-local coordinates  $0 \leq \xi < 1$  and the  $u_i^e$  denotes the value of  $u_h$  at the  $i$ -th node. Defining the ansatz-functions on the nodes of the element  $e$ ,  $\phi_1^e(\xi) = 1 - \xi$  and  $\phi_2^e(\xi) = \xi$ , the latter simplifies to

$$u_h^e(\xi) = \phi_1^e(\xi)u_1^e + \phi_2^e(\xi)u_2^e. \quad (3.1.13)$$

### 3. Algorithm and implementation

---

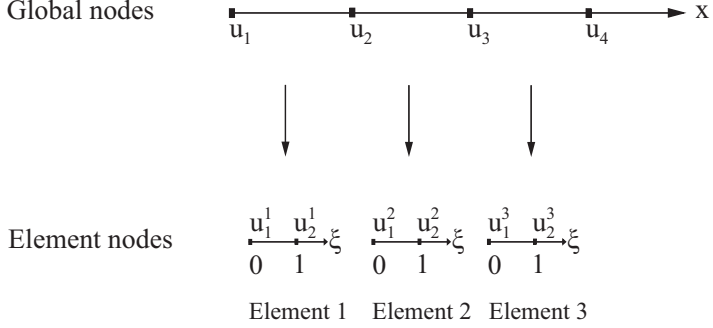


Figure 3.1.3.: The ansatz-functions are interpolated between the nodes of the elements. ensuring the connection condition is fulfilled as each node belongs to two elements. Each node gets a global numbering, and on each element the ansatz-functions are approximated using the element-local numbering.

The relation between the local node numbering  $u_i^e$  and the global node index  $j$ , is given by the connectivity matrix  $C$ ,

$$u_j = u_i^e, \quad j = C(e, i), \quad (3.1.14)$$

while the relation between the element-local coordinates  $\xi$  and the global coordinates  $x$  is given by

$$x(\xi) = \phi_1^e(\xi)x_1^e + \phi_2^e(\xi)x_2^e, \quad (3.1.15)$$

where  $x_i^e$  denotes the global coordinates of the  $i$ -th node of the element  $e$ .

We can then summarize the procedure of solving a one-dimensional linear differential equation using linear ansatz-functions as a task of finding the values of the  $\phi_i^e$ , where the completeness and the orthogonality of the ansatz-functions,

$$\sum_i \phi_i^e(x) = 1 \quad \text{and} \quad \phi_i^e(x_j) = \delta_{ij}, \quad (3.1.16)$$

must be fulfilled, i.e. the interpolation at an element-local position  $\xi$  is done by weighting the values  $u_1^e$  and  $u_2^e$ . An extension to ansatz-functions of higher order can then be easily obtained by increasing the number of element nodes, such that eq. 3.1.16 is fulfilled.

The value of the solution at a global coordinate  $x$  can then easily be determined by summing up the weighted values at the nodes of all elements,

$$u^h(x) = \sum_{i=1}^N \phi_i(x)u_i. \quad (3.1.17)$$

The scheme can be extended to, in principle, arbitrary dimensions, that do not necessarily need to be of spacial dimension, but can for example model physical properties

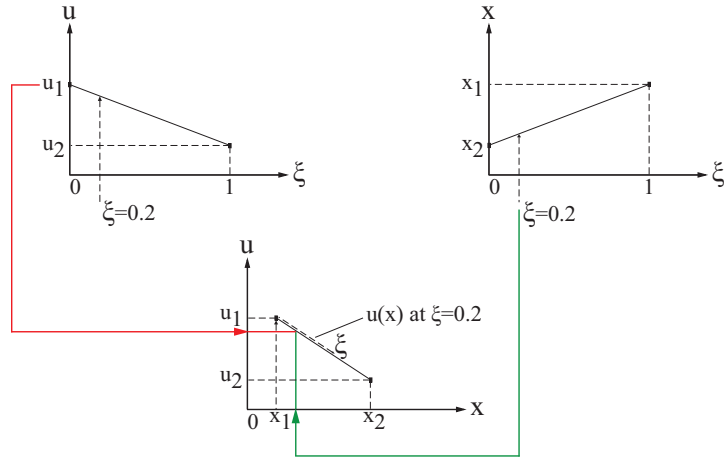


Figure 3.1.4.: Relation between element-local coordinates  $\xi$ , local coordinates  $x$ , and the solution  $u_h(x)$  for one-dimensional linear elements.

like temperature, pressure and so on. One can also use different ansatz-functions (like polynomials of different degrees) on different elements, and solve for vectorial functions  $\mathbf{u}$ . Therefore the method of finite elements is a very versatile tool for a giant range of applications.

Implementing boundary conditions is not a very difficult task, as boundaries of Dirichlet type will lead to a reduction of the system's degrees of freedom, introducing the node values  $u_i^h = u_0$ , while boundaries of Neumann-type are evaluated during the integration over each element, as stated above, and using the derivate of each ansatz-function to calculate the gradient. Then, using eq. 3.1.7 and minimizing with variation of the unknown element-node values  $u_i^h$ , one obtains an expression similar to eq. 3.1.10, with the matrix entries  $A_{ij}$  being

$$A_{ij} = \sum_i u_i \int_{\Omega_h} \nabla \phi_i \nabla \phi_j + a \phi_i \phi_j \, dV + \int_{\partial\Omega} u_0 \phi_i \phi_j \, dS = 0, \quad (3.1.18)$$

where we already used the reduction of the degrees of freedom introduced by the Dirichlet constraints, and the sum goes over all  $N$  element nodes that have unknown values  $u_i^e$ . However, for practical purposes, one does not want to expand in the ansatz-functions  $\phi_i$ , but one can use element-wise calculation of the integrals and then arrange the results via the connectivity matrix  $C$ .

During our calculations for the two-colloid problem, we use two-dimensional, triangular meshes, but a generalization to three-dimensional (and also higher-dimensional) meshes is straight-forward. A triangular mesh element consists of three nodes, accordingly

### 3. Algorithm and implementation

---

eq. 3.1.12 transforms to

$$u^h(x, y) = \sum_{i=1}^3 \phi_i^e(x, y) u_i^e, \quad (3.1.19)$$

where the linear ansatz-functions for triangles are given by

$$\phi_i^e(x, y) = a_i + b_i x + c_i y \quad i = 1, 2, 3. \quad (3.1.20)$$

The coefficients  $a_i, b_i, c_i$  depend on the geometry of the triangle and can be calculated via the orthogonality condition,

$$\phi_i^e(x_j, y_j) = \delta_{ij}. \quad (3.1.21)$$

For triangular elements, the ansatz-functions  $\phi_i(x, y)$  can be interpreted as a center of mass, weighting the values  $u_i$  according to the differential equations and the boundaries.

The system of equations 3.1.10 is linear, if  $f$  in equation 3.1.1 is linear, so that the resulting system of equations is given by

$$\sum_{j=1}^n A_{ij} u_j - F_i = 0, \quad (3.1.22)$$

where  $\mathbf{A}$  is called the stiffness-matrix.  $A$  is positive semi-definite, symmetric and sparse due to the orthogonality of the ansatz-functions on the elements, which yields

$$A_{ij} = \begin{cases} 0 & \text{if } j \notin \{i-1, i, i+1\} \\ \neq 0 & \text{if } j \in \{i-1, i, i+1\} \end{cases}, \quad (3.1.23)$$

i.e. by sorting the coefficients in a clever way, we can obtain a band structure in the resulting stiffness-matrix. Due to the size of common problems for which such numerical solution methods are used, the solution of the resulting linear system is huge and can usually not be solved directly. Highly efficient methods are available to store the elements of sparse matrices, like block matrices or band structure matrices while the determination of the solution vector can be obtained via common methods [25]. Usually stationary iterative solvers like Gauss-Seidel, Jacobi or Successive over-relaxation (SOR) are used, or Krylov-subspace methods like the Conjugate Gradient (CG) method, the Generalized minimal residual method (GMRES) or the method of Biconjugate Gradients (BiCG) are applied. The choice on which solver to use and its efficiency depends highly on the symmetry and structure of the matrix. For our calculations presented in chapter 4 and 5 we used a SOR preconditioned Biconjugate gradient stabilized method (BiCGSTAB) for sequential runs and a CG method for parallel runs.

However, if  $f$  is nonlinear, i.e.  $f(u)$ , the resulting system of equations 3.1.22 is nonlinear. In order to use the efficient and fast linear solvers previously mentioned, we want to linearize each equation,

$$\mathbf{G}(\mathbf{u}) = 0, \quad (3.1.24)$$

where we introduced  $\mathbf{G}(\mathbf{u}) = \mathbf{A}\mathbf{u} - \mathbf{F}(\mathbf{u})$  for the sake of simplicity, so that the problem reduces to that of finding the zeros of  $\mathbf{G}(\mathbf{u})$ . Assuming sufficient differentiability, we can perform a Taylor expansion around a guessed value  $\mathbf{u}_0$  to the linear order,

$$\mathbf{G}(\mathbf{u}) = \mathbf{G}(\mathbf{u}_0) + \Delta\mathbf{u} \frac{d\mathbf{G}(\mathbf{u}_0)}{d\mathbf{u}}, \quad \Delta\mathbf{u} = \mathbf{u} - \mathbf{u}_0. \quad (3.1.25)$$

The guessed value  $\mathbf{u}_0$  can then be determined by Newton's method in an iterative procedure, approximating  $\mathbf{G}(\mathbf{u}_0) \approx 0$  by a recursion rule,

$$\mathbf{u}_{n+1} = \mathbf{u}_n - \mathbf{G}'(\mathbf{u}_n)^{-1} \mathbf{G}(\mathbf{u}_n), \quad (3.1.26)$$

where we introduced the Jacobi matrix,

$$\mathbf{G}'(\mathbf{u}) = \frac{d\mathbf{G}}{d\mathbf{u}} = \begin{bmatrix} \frac{\partial G_1}{\partial u_1} & \dots & \frac{\partial G_1}{\partial u_n} \\ \vdots & \ddots & \vdots \\ \frac{\partial G_n}{\partial u_1} & \dots & \frac{\partial G_n}{\partial u_n} \end{bmatrix}. \quad (3.1.27)$$

The convergence depends on the initial guess  $\mathbf{u}_0$  (the closer to the zero, the better, but in the absence of any intuition about where the zero might lie, we can limit ourselves to a small interval by making use of the intermediate value theorem). The method will usually converge, provided this initial guess is close enough to the unknown zero, and that  $\mathbf{G}'(\mathbf{u}_0) \neq 0$ . Then, the linearized system of equations is solved after each iteration, as long as the linearization residual  $\epsilon$  is larger than the tolerance. For a zero of multiplicity 1, the convergence is at least quadratic, meaning that the residual  $\epsilon$  decays quadratically with the number of iterations.

## 3.2. The DUNE project

A huge number of software packages, both commercial and open source, are available for solving partial differential equations, using different solution methods, programming philosophies and data structures. Each of these packages has its own unique set of advantages and disadvantages. The most common problem is that each software package uses different data structures representing a computational grid, and therefore, code written for a specific package cannot easily be transformed to work with a different one. However, the requirements for such data structures vary widely from application to application. The typical trade-off is efficiency vs. flexibility. Hence each code will be more suitable in some areas of applications, and less so in others.

For our implementation we were focusing on very generic (different solution methods, reuse, extendibility) and efficient open source projects. The “Distributed and Unified Numerics Environment“ DUNE [57] has the capability to overcome these common the

### 3. Algorithm and implementation

---

data-handle limitations. DUNE has a component-based software architecture where each component possesses an abstract interface and exists in several implementations with different features. This concept is realized very efficiently using generic programming techniques in C++, which essentially removes the interface overhead at compile-time [8] [9]. Additionally, existing software can be reused to implement any of the components functionality and also to be used in own projects (called `dune-modules`).

Of particular interest for our needs were the finite element codes UG, ALBERTA, and ALUGrid, that have been adapted to the DUNE framework, enabling us to use parallel and adaptive meshes with multiple element types and refinement rules linked together in one executable. Local community support available via the SimTech cluster of excellence at the University of Stuttgart was also one of the reasons for our decision.

In the following we will give a quick overview on the DUNE core modules and `dune-pdelab`, on top of which the IPBS module is built:

**dune-common** provides base-classes used by all other modules as well as the build-system infrastructure and the library to handle dense matrices and vectors.

**dune-grid** is containing all the infrastructure to handle nonconforming elements in hierarchically nested grids, that can handle multi-type elements in arbitrary space dimensions. A full parallelization for all grids is guaranteed and output routines are offered.

**dune-istl** contains the generic sparse matrix and vector classes as well as a variety of solvers. A special feature is the use of templates to exploit the recursive block structure of finite element matrices at compile time. Available solvers include Krylov methods, (block-) incomplete decompositions and aggregation-based algebraic multigrid.

**dune-localfunctions** provides shape functions defined on reference elements. Also provided are interpolation operators and special keys which can be used to assemble global function spaces on finite-element grids.

**dune-pdelab** provides classes to considerably simplify the implementation, offering flexible discrete function spaces and operators based on weighted residual formulation. In particular we were interested in its nonlinear, stationary finite element methods.

Using the simplifications `dune-pdelab` offers, we can now provide an overview of the core components our nonlinear Poisson–Boltzmann solver. Detailed information can be found in the code documentation, that will be available with the source code.

- The main program (`IPBS.cc`), defining global properties and creating the grid via a so-called grid factory. The grid, read in the GMSH-format, is initialized and a grid-pointer is created, so properties of the nodes and elements can be accessed. For the grid handling we used the UG grid manager and read in boundary properties via physical properties defined in the mesh (see sec. 3.3). After the possibility of global refinement, all the parallel communicators are initialized and the grid is distributed

to all processors. Using UG it is at the moment not possible to refine the mesh adaptively in a parallel run, but switching to ALUGrid is an alternative for future projects.

- The driver (`ipbs_Pk.hh`), being the core component setting up a grid function space, an abstract class containing the finite element map providing a basis on each element (which are polynomials of degree  $k$  in our case), a method to reduce the degrees of freedom introduced by Dirichlet constraints, and a vector backend.  
The grid operator space, computing the residual system of equations is set up specifying a local operator with trial and test grid function spaces and selecting a suitable matrix backend.  
A linear solver backend is selected and the Newton solver is applied, storing the degrees of freedom in a vector container  $\mathbf{u} \in \mathbf{U}$ . Finally output routines are called.
- The local operator (`PBLocalOperator.hh`), providing the volume integral `alpha_volume` and the surface integral `alpha_boundary` in the evaluation of the stiffness matrix  $A_{ij}$ , eq. 3.1.22. The system of equations then is assembled by the gridfunctionspace.
- Classes providing evaluation methods for element and boundary types, as well as methods evaluating the value of Dirichlet or Neumann boundary conditions (`boundaries.hh`).

Furthermore we provide various methods for the output of the electric field and potential as well as the resulting ion density profile, a method measuring the force between particles, the infrastructure for adaptive refinement full parallelization for our code providing support for all kinds of two-dimensional calculations and the infrastructure for three-dimensional calculations. For detailed information please refer to the code documentation.

### 3.3. Mesh generation using Gmsh

In our implementation, the grid is read in via the Gmsh mesh format, specifying positions of vertices and their connections to elements. A simple to use and powerful tool to set up different geometries and problem specifications has been found in Gmsh, a 3D finite element grid generator with a build-in CAD engine and post-processor [30].

Gmsh is built around four modules: geometry, mesh, solver and post-processing, of which we are interested only in the first two. The specification of any input to these modules is done either interactively using the graphical user interface or in ASCII text files using Gmsh's own scripting language, which have proven to be a powerful tool for our method.

The basic procedure to set up a geometry file can be seen in the following listing, setting up a single sphere used during our algorithm evaluation.

### 3. Algorithm and implementation

---

Gmsh geometry file example

```
// Gmsh project created on Mon May 30 14:41:33 2011
// Creates the iPBS single sphere with a symmetric mesh
// refinement is done via the characteristic length

radius = 10;
position = 0; // Center position of the sphere
box_size = 50;
outer_refinement = 5;
inner_refinement = 0.2;

// Define the geometry for 2d-sphere (iPBS)

Point(1) = {position , 0, 0, 1.0};
Point(2) = {position , radius , 0, inner_refinement};
Point(3) = {position-radius , 0, 0, inner_refinement};
Point(4) = {position+radius , 0, 0, inner_refinement};
Point(5) = {-box_size , 0, 0, outer_refinement};
Point(6) = {box_size , 0, 0, outer_refinement};
Point(7) = {-box_size , box_size , 0, outer_refinement};
Point(8) = {box_size , box_size , 0, outer_refinement};
Circle(1) = {4, 1, 2};
Circle(2) = {2, 1, 3};
Line(3) = {4, 6};
Line(4) = {3, 5};
Line(5) = {5, 7};
Line(6) = {7, 8};
Line(7) = {8, 6};
Line Loop(8) = {6, 7, -3, 1, 2, 4, 5};
Plane Surface(9) = {8};

// Define physical groups for assigning B.C.
// 0 is for Dirichlet boundary elements
// 1 for Neumann
// 2 for iPBS
Physical Line(0) = {6,7,5};
Physical Line(1) = {4, 3};
Physical Line(2) = {2, 1};

// At least one physical surface (or physical volume)
// is needed by DUNE gmshreader (otherwise all elements
// are boundaries)
Physical Surface(13) = {9};
```

The procedure creating a mesh using the scripted Gmsh geometry module can be summarized in a few simple steps:

1. Define global variables used in the script.
2. Define the points of the geometry you want to set up. A point has three coordinates, and a characteristic length, which is the typical length between vertices at this particular element.
3. Connections between the points are set using the geometrical shape one wants to achieve. Besides straight lines, circles or ellipses, there exist splines and other more complicated shapes, so that an arbitrary setup can be described.
4. As we focus on two-dimensional meshes in this work, a definition of a closed surface (called `Line Loop` in Gmsh) must be defined enclosing the `Plane Surface`. One can also use non-planar surfaces and define a three-dimensional volume in the same way.
5. As the most important step in our method is the determination of boundary conditions, we need a way to communicate the type of the boundary to the dune-module. This can be achieved easily by what is called physical properties in Gmsh, as the Dune gmshreader is able to extract these properties from the grid.  
We therefore define the type of the boundary (i.e. if we want to set Dirichlet, Neumann or iterated boundary conditions) as a physical property of the boundary element. In our implementation, the type 0 is reserved for boundaries of Dirichlet type, type 1 is for zero flux Neumann boundaries and all boundary types  $\geq 2$  are calculated with the iterative procedure.
6. Finally, a physical surface (and a physical volume in three dimensions) needs to be defined.

Figure 3.3.1 shows the resulting mesh of the above geometry script produced with a Delaunay triangulation method. Gmsh currently provides a choice between three 2D unstructured algorithms and between two 3D unstructured algorithms, but as our geometrical domains remain quite simple while our main focus is a fine resolution on the particles surfaces, we have a lot of freedom in selecting the meshing algorithm.

### 3. Algorithm and implementation

---

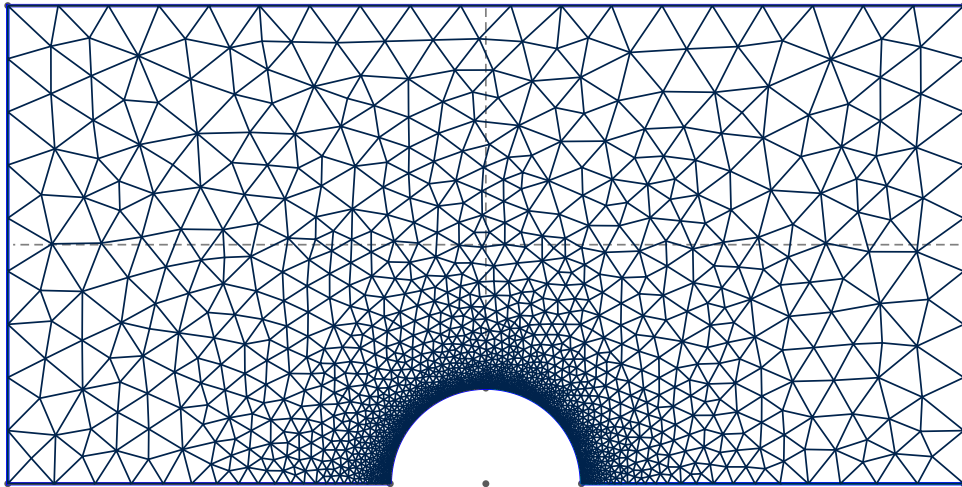


Figure 3.3.1.: A simple grid for simulating a spherical particle, that can be obtained easily with Gmsh using the geometry script presented above. The refinement on the surface can be influenced by using the characteristic length on the points of the geometry.

### 3.4. Algorithm details and implementation

As mentioned in chapter 1.2.1, we use an iterative method for determining the implicit boundary condition at the surface of particles. Using boundary conditions of Neumann type, we determine the electric field on the surface via the charge density  $\rho(\mathbf{r})$ , where in the Poisson–Boltzmann description the charge density of the micro-ions is related to the electrostatic potential  $\phi$ ,

$$\mathbf{E}_S(\mathbf{r}) = -\nabla\phi_S(\mathbf{r}) = f(\rho(\phi)), \quad \mathbf{r} \in S. \quad (3.4.1)$$

The functional  $f$  can in principle take different forms, depending on the symmetry and dimensionality of the system, which affects the corresponding Green's function. Here  $\phi_S$  denotes the potential at the surface of the colloid and  $\mathbf{E}_S$  the corresponding electric field.  $\rho(\mathbf{r})$  is the charge distribution in the whole domain  $\Omega_h$  of computation.

Particles with an arbitrary charge distribution can then be modeled by assigning a local surface charge density  $\sigma(\mathbf{r})$ . However, we will limit ourselves to constant surface charge densities at the moment, the implementation of local varying surface charge densities is straight-forward and can be easily implemented using the existing code. Using Gauss's law at a charged interface [47], we get the jump in the electric field,

$$\mathbf{E}_{out}(\mathbf{r})\hat{\mathbf{n}}_{out} - \mathbf{E}_{in}(\mathbf{r})\hat{\mathbf{n}}_{in} = 4\pi\ell_B\sigma(\mathbf{r}). \quad (3.4.2)$$

In terms of finite elements, we can rewrite the latter expression for an element  $i$ ,

$$\begin{aligned} \mathbf{E}_{in}(\mathbf{r}_i) &= \mathbf{E}_{ext}(\mathbf{r}_i) - 2\pi\ell_B\sigma_i \\ \mathbf{E}_{out}(\mathbf{r}_i) &= \mathbf{E}_{ext}(\mathbf{r}_i) + 2\pi\ell_B\sigma_i. \end{aligned} \quad (3.4.3)$$

As we are using Neumann boundary conditions, and our domain is defined only on the outside of the particle, we set the normal flux on a boundary element  $i$ ,

$$\begin{aligned} j_i(\mathbf{r}_i) &= 2\pi\ell_B\sigma_i + \mathbf{E}_{ext}(\mathbf{r}_i) \cdot \hat{\mathbf{n}}_i \\ &= 2\pi\ell_B\sigma_i - \nabla\phi_{ext}(\mathbf{r}_i) \cdot \hat{\mathbf{n}}_i. \end{aligned} \quad (3.4.4)$$

Here,  $\phi_{ext}(\mathbf{r}_i)$  denotes the superposition of the electrostatic potential of all charges in the system at the position  $r_i$  of the boundary element. These charges include the surface charges of all the remaining surface elements as well as the charge distribution of the dissolved ions. Using the three-dimensional Green's-function, we can split the contributions of the ions from that of surface charge elements,

$$j_i(\mathbf{r}_i) = 2\pi\ell_B\sigma_i + \ell_B \int_{\Omega} \rho(\mathbf{r}_i) \frac{\mathbf{r}_i - \mathbf{r}'}{|\mathbf{r}_i - \mathbf{r}'|^3} d\mathbf{r}' \cdot \hat{\mathbf{n}}_i + \ell_B \int_{\partial\Omega} \sigma_j(\mathbf{r}') \frac{\mathbf{r}_i - \mathbf{r}'}{|\mathbf{r}_i - \mathbf{r}'|^3} d\mathbf{r}' \cdot \hat{\mathbf{n}}_i, \quad (3.4.5)$$

where the second term is integrated over the whole domain of computation to get the ion contribution and the last term accounts for the other charged surface elements of all

### 3. Algorithm and implementation

---

particles (including the particle itself). For a symmetric  $z - z$  electrolyte, the charge density  $\rho(\mathbf{r})$  is given by eq. 2.3.8,

$$\rho(\Phi(\mathbf{r})) = \frac{\kappa^2 z}{4\pi\ell_B} \sinh(-z\Phi(\mathbf{r})), \quad (3.4.6)$$

This implies that we can write the implicit Neumann boundary conditions as a sum of three contributions to the surface flux, modeling an effective charge density at the surface,

$$\sigma_i^{\text{eff}} = \frac{1}{4\pi\ell_B} j_i = \frac{1}{4\pi\ell_B} \left( j_i^{\text{imposed}} + j_i^{\text{surface charges}} + j_i^{\text{ion distribution}} \right). \quad (3.4.7)$$

Equation 3.4.7 is the central point of the algorithm, computing the appropriate boundary conditions for such systems as described in chapter 1.2.1. We dubbed this scheme *IPBS*, an iterative Poisson–Boltzmann Solver, as the latter expression can be used as a starting point for employing an iterative approach determining the effective surface charge on each element. The iterative scheme can be implemented using one of the many available methods[72] such as Jacobi, Gauss-Seidel, or Successive Over-Relaxations (SOR). In the SOR approach, which has been employed for the calculation presented here, equation 3.4.1 is approximated to a desired accuracy using a sequence of iteratively estimated solutions,

$$\nabla\Phi_S^{(n+1)}(\mathbf{r}) \cdot \hat{\mathbf{n}} = \alpha f \left( \rho \left( \Phi^{(n)}(\mathbf{r}) \right) \right) + (1 - \alpha) \nabla\Phi_S^{(n)}(\mathbf{r}) \cdot \hat{\mathbf{n}}. \quad (3.4.8)$$

The initial step is done using an arbitrary (usually random) initial guess of the solution, and relaxing the solution via the parameter  $\alpha \in (0, 2)$  in each iteration step.

This scheme can be employed to obtain successive estimates of the value of the potential (unknown Dirichlet boundary conditions) or field (unknown Neumann boundary conditions) at the surface of the colloids, in cases where neither constant surface charge nor constant surface potential hold true. Such an estimation of the effective surface charge density  $\sigma^{\text{eff}}$  is a necessary ingredient to solve the nonlinear Poisson Boltzmann equation using a finite elements approach with Neumann boundary conditions. The IPBS algorithm, can then be summarized as follows:

1. Assign an arbitrary (guessed or random) value for the initial surface charge density,

$$\sigma_i^{\text{start}} = \frac{1}{4\pi\ell_B} j_i^{(n)}$$

2. Solve the nonlinear problem using the driver described in chapter 3.2, using this guessed boundary condition, and obtain the estimate for the potential,  $\Phi^{(n)}$ .
3. Using this potential, obtain the corresponding ion distribution, compute a new estimate for the effective surface charge density, and set the new boundary condition by the flux through the surface element,  $j_i^{n+1}$ , inserting  $\Phi^{(n)}$  into eq.3.4.8.

4. Steps 2 and 3 are repeated, until a desired relative accuracy,

$$\Delta = \max \left\{ 2 \frac{|j_S^{n+1} - j_S^{(n)}|}{|j_S^{n+1} + j_S^{(n)}|} \right\}$$

is achieved. We note that this is not a strict abort criterion ensuring convergence to the correct solution, but usually one obtains a sufficient estimate such that the system of equations converges using this fix-point iteration.

### 3.4.1. Including dielectric mismatch

One of the great advantages of the algorithm determining the effective surface charge density  $\sigma^{\text{eff}}$  self-consistently, is the proper treatment of a dielectric contrast between areas of different dielectric constant. Using the boundary intersections of the finite elements, the algorithm can accurately deal with a jump of the dielectric constant. In experiments, such interfaces with a dielectric mismatch are the norm, however few simulations have attempted to tackle the problem and analytical approaches are rare. In this thesis we focus on the particular case of colloids in aqueous solution which can be thought of as hard shells within which the dielectric constant is different from the surrounding solution. The implementation also offers the possibility of examining polarization effects of planar surfaces.

In recent experiments, the interactions of colloidal particles suspended in salt solutions enclosed by a nano-slit of  $SiO_2$  have been examined [46]. In such confining geometries like-charge attraction between the colloids and the corner of the slit have been reported. Especially if imposing DNA-molecules into the slit this offers a new variety of experimental possibilities due to the entropic unrolling of DNA [45], that usually is difficult to obtain. However due to the combination of dielectric interfaces and the computational effort required to simulate the salt ions, the origin of the reported attraction in such systems has so far resisted from being answered by common simulations. Our calculations offer the possibility to analyze electrostatic interactions in such systems modeling the solution on a mean-field level.

The correct way to specify the dielectric properties of a material is by setting the relative dielectric permittivity,  $\varepsilon_r$ , instead of assigning a different Bjerrum length  $\ell_B$  to each material. Therefore we define the Bjerrum length in our system to be that in the solution, such that all other Bjerrum lengths would have to be divided by the solution's relative permittivity. As all dielectric properties only depend on the relative values of the permittivity this choice will not change any physical properties and we can specify the jump of the electric field on intersections with dielectric mismatch (see eq. 3.4.2),

$$(\varepsilon_1 \mathbf{E}_{out}(\mathbf{r}) - \varepsilon_2 \mathbf{E}_{in}(\mathbf{r})) \cdot \hat{\mathbf{n}}_{out} = 4\pi \ell_B \sigma(\mathbf{r}) \quad (3.4.9)$$

Instead of solving Poisson's equation in the inner region of the particles we replace this problem by an equivalent one, namely one that provides the same solution to the

### 3. Algorithm and implementation

---

Poisson–Boltzmann equation in the outer region without the dielectric discontinuity. This can indeed be achieved [69], by replacing the inner region of dielectric permittivity  $\varepsilon_2$  by one of dielectric permittivity  $\varepsilon_1$ , and introducing an induced surface charge density  $\sigma^{ind}(\mathbf{r})$  [40]. Applying Gauss's law to the electric field in proximity of the surface  $S$  one obtains:

$$(\mathbf{E}_{out}(\mathbf{r}) - \mathbf{E}_{in}(\mathbf{r})) \cdot \hat{\mathbf{n}} = 4\pi\ell_B (\sigma^{ind}(\mathbf{r}) + \sigma(\mathbf{r})) \quad (3.4.10)$$

Again, we split the field in terms of finite elements and introduce the electric field of all charges in the system. This field  $\mathbf{E}_{ext}(\mathbf{r}_i)$  acting on the surface element  $i$  is caused by a superposition of the potentials of the ion distribution, the surface charge density of the surface elements and the induced polarization charges at each surface element. The discretized field at the surface element  $i$  then reads:

$$\begin{aligned} \mathbf{E}_{in}(\mathbf{r}_i) &= \mathbf{E}_{ext}(\mathbf{r}_i) - 2\pi\ell_B (\sigma^{ind}(\mathbf{r}) + \sigma(\mathbf{r})) \\ \mathbf{E}_{out}(\mathbf{r}_i) &= \mathbf{E}_{ext}(\mathbf{r}_i) + 2\pi\ell_B (\sigma^{ind}(\mathbf{r}) + \sigma(\mathbf{r})). \end{aligned} \quad (3.4.11)$$

Inserting the latter expression for  $\mathbf{E}_{in}$  into eq. 3.4.9, we can isolate an implicit expression for the induced charge density,

$$\begin{aligned} (\varepsilon_1 - \varepsilon_2) \mathbf{E}_{ext}(\mathbf{r}_i) + (\varepsilon_1 + \varepsilon_2) 2\pi\ell_B (\sigma^{ind}(\mathbf{r}) + \sigma(\mathbf{r})) &= 4\pi\ell_B \sigma \\ \Rightarrow \sigma^{ind}(\mathbf{r}_i) &= \frac{\varepsilon_1 - \varepsilon_2}{\varepsilon_1 + \varepsilon_2} \left( \sigma + \frac{\varepsilon_1}{2\pi\ell_B} \mathbf{E}_{ext}(\mathbf{r}_i) \right). \end{aligned} \quad (3.4.12)$$

Being the starting point of another iterative procedure, the latter expression can be determined every iteration step for each surface element. The induced surface charge  $\sigma^{ind}$  can be introduced to the iterative scheme of the IPBS algorithm directly by extending the effective charge density 3.4.7,

$$\sigma_i^{\text{eff}} = \frac{1}{4\pi\ell_B} j_i^{\text{eff}}, \quad (3.4.13)$$

with the effective surface flux with respect to polarization effects being defined by

$$\begin{aligned} j^{ind}(\mathbf{r}_i) &= \mathbf{E}_{out}(\mathbf{r}_i) \cdot \hat{\mathbf{n}} = \mathbf{E}_{ext}(\mathbf{r}_i) \cdot \hat{\mathbf{n}} + 2\pi\ell_B (\sigma + \sigma^{ind}(\mathbf{r}_i)) \\ &= \frac{2}{\varepsilon_1 + \varepsilon_2} \sigma + \frac{2\varepsilon_1}{\varepsilon_1 + \varepsilon_2} \mathbf{E}_{ext}(\mathbf{r}_i). \end{aligned} \quad (3.4.14)$$

That way, we can obtain a new estimate for the external field  $\mathbf{E}_{ext}$  and the induced surface charge  $\sigma^{ind}$  at the same time, without having to iterate twice. The estimate for the induced surface charge can be treated in an analogous matter as the estimates of the effective surface flux in eq. 3.4.5, making use of one of the many iterative solution methods.

For reasons of simplicity, we decided to employ another Successive Over-Relaxations procedure (3.4.8), starting from an induced charge  $\sigma^{\text{start}} = 0$  and using a common relaxation parameter  $\alpha$  for both estimation procedures. That way we maintained the convergence behavior of the system without having any dielectric contrast for bad dielectric materials ( $\varepsilon_1 \gg \varepsilon_2$ ), but observing a decline of the convergence for materials where  $\varepsilon_1 \ll \varepsilon_2$ .

This convergence behavior is intuitive, as the induced charge will strongly depend on the estimated values of the electric field at the surface.

### 3.4.2. Use of symmetry

A huge reduction in computational effort can be achieved exploiting symmetries in the system, as the number of mesh elements  $N$  depends on the length  $l$  of the simulated system,  $N \propto l^d$ , where  $d$  denotes the dimension of the system. A drastically reduction of the degrees of freedom can then be achieved by reducing the dimension. For a system of planes, one can use two-dimensional meshes, or, in principle, even reduce the system to an effective one-dimensional problem.

As we want to model colloidal particles, it is appropriate to use a cylindrical coordinate system, assuming rotational invariance. The particle can then be projected into the  $r$ - $z$  plane (see figure 3.4.1), and we can use an explicit integration in the angular coordinate  $\vartheta$ .

The dune-pdelab concept does not know the concepts of coordinate systems a priori, but is only working with element-local and entity-global coordinates. Therefore we had to adapt the creation of the stiffness-matrix 3.1.22 such, that the integrals 3.1.18 are performed in cylindrical coordinates, yielding

$$A_{ij} = \sum_i u_i 2\pi \int_{-z}^z \int_0^r \nabla \phi_i \nabla \phi_j + a \phi_i \phi_j r \, dr \, dz + 2\pi \int_{\partial\Omega} u_0 \phi_i \phi_j r \, dr \, dz = 0. \quad (3.4.15)$$

The other modification necessary is in the calculation of the boundary conditions. In Cartesian coordinates, the electric field of a charge distribution  $\rho(\mathbf{r})$  is given by

$$\mathbf{E}(\mathbf{r}) = \ell_B \int \rho(\mathbf{r}') \frac{\mathbf{r} - \mathbf{r}'}{|\mathbf{r} - \mathbf{r}'|^3} d^3V, \quad (3.4.16)$$

where the integration is performed using the volume element  $d^3V = dx \, dy \, dz$ . Using radial coordinates

$$\mathbf{r} = \begin{pmatrix} r \\ z \\ \varphi \end{pmatrix} \doteq \begin{pmatrix} r \\ z \\ 0 \end{pmatrix} \quad \text{and} \quad \mathbf{r}' = \begin{pmatrix} r' \\ z' \\ \varphi' \end{pmatrix} \doteq \begin{pmatrix} r' \\ z' \\ \vartheta \end{pmatrix} \quad (3.4.17)$$

with the relative angle  $\vartheta = \varphi' - \varphi$  and the volume element  $dV = r dr \, d\varphi \, dz$ , the integral in equation 3.4.16 transforms to

$$\int \frac{\mathbf{r} - \mathbf{r}'}{|\mathbf{r} - \mathbf{r}'|^3} dx \, dy \, dz = \int \frac{(z - z') \hat{\mathbf{e}}_z + (r - r' \cos \vartheta) \hat{\mathbf{e}}_r + \vartheta \hat{\mathbf{e}}_\vartheta}{\left[ r^2 + r'^2 - 2rr' (1 - \sin^2(\frac{\vartheta}{2})) + (z - z')^2 \right]^{3/2}} r dr \, d\varphi \, dz. \quad (3.4.18)$$

### 3. Algorithm and implementation

---

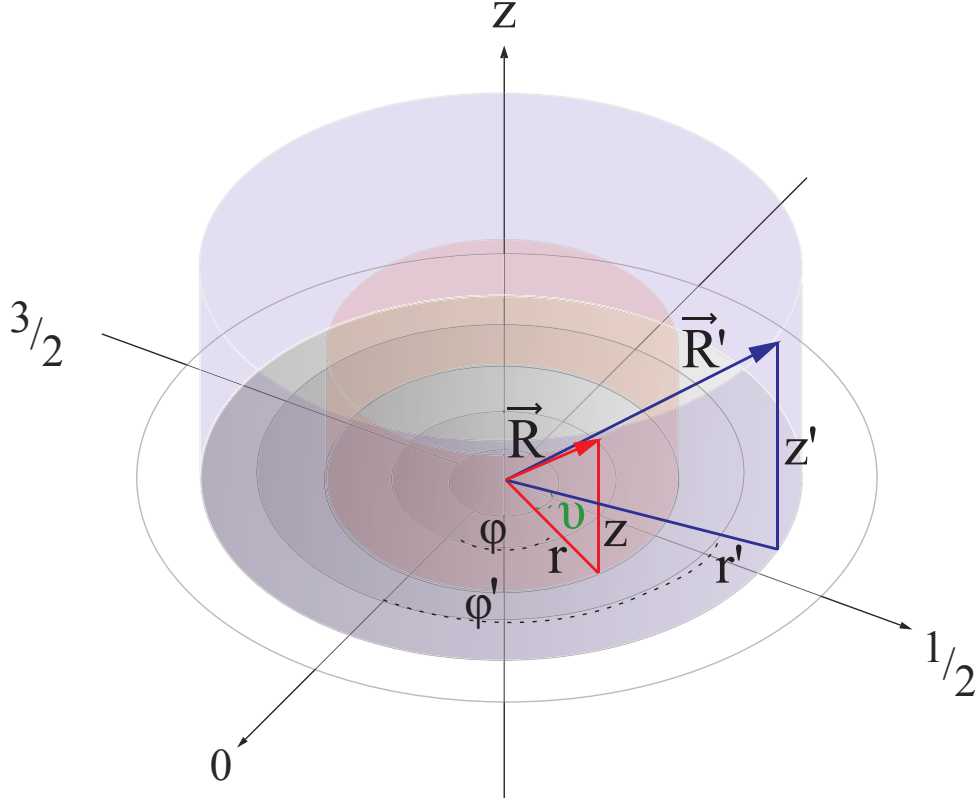


Figure 3.4.1.: A cylindrical coordinate system as used in our calculation. Without loss of generality the angle  $\vartheta$  can be defined as  $\vartheta = \varphi - \varphi'$  and the coordinate system shifted such that  $\varphi = 0$ .

Using this approach we can use a 2-dimensional mesh like shown in figure 3.3.1 and perform an explicit integration in  $\varphi$  to model particles of cylindrical symmetry when using a zero flux b.c. on the  $z$ -axis. The integration in  $r$  and  $z$  direction can then be done easily numerically by adding up the contributions for each element.

We will use the discretized values  $r_i$  and  $z_i$  for the element center coordinates in the case of a volume integral  $\int_V$  and the intersection center coordinates in the case of surface integrals  $\int_{\partial V}$ . Substituting  $A = r^2 + r'^2 + (z - z')^2 + 2rr'$ ,  $B = 4rr'$  and  $q = \frac{\vartheta}{2}$  in equation 3.4.18, the electric field 3.4.16 can be rewritten as

$$\mathbf{E}(r_i, z_i) = \ell_B \sum_j \rho(r_j, z_j) \int_0^\pi \frac{\Delta z_{ij} \hat{\mathbf{e}}_z + (r_i + r_j \cos(2q)) \hat{\mathbf{e}}_r + 2q \hat{\mathbf{e}}_\varphi}{[A - B + 2B \sin^2(q)]^{3/2}} r_j \, dq, \quad (3.4.19)$$

where we introduced  $\Delta z_{ij} = z_i - z_j$ .

Considering equation 3.4.3, we have to determine the normal component of the

external field in order to get its contribution to the flux through a surface element  $i$ ,

$$\mathbf{E}(r_i, z_i) \cdot \hat{\mathbf{n}}_i = \ell_B \sum_j \rho(r_j, z_j) \int_0^{2\pi} \frac{\Delta z_{ij} n_{i,z} + (r_i + r_j \cos(2q)) n_{i,r}}{[A - B + 2B \sin^2(q)]^{3/2}} r_j dq, \quad (3.4.20)$$

where  $\hat{\mathbf{n}}_i$  denotes the normal vector of the  $i$ -th surface element of the particle and  $n_{i,r}$  and  $n_{i,z}$  denote its radial and axial coordinates respectively. Note that the  $\hat{\mathbf{e}}_\varphi$  term vanishes as the surface normal of any spherical particle will be perpendicular to the direction of rotational invariance.

The integral in equation 3.4.20 can be written in terms of the complete elliptic integrals of first kind  $K(m)$  and of second kind  $E(m)$  [1], using  $m = \sqrt{\frac{B}{A}}$  we get:

$$\begin{aligned} & \int_0^\pi \frac{\Delta z_{ij} n_{i,z} + (r_i + r_j \cos(2q)) n_{i,r}}{(A - B + 2B \sin^2(q))^{3/2}} dq \\ &= \frac{2}{(A - B) \sqrt{AB}} [(-\Delta z_{ij} n_{i,z} + (2Ar_j - B(r_i + r_j)) n_{i,r}) E(m) \\ & \quad + r_j n_{i,r} (-2A + 2B) K(m)] \end{aligned} \quad (3.4.21)$$

The charge density in the Poisson–Boltzmann description is given by eq. 2.3.8,

$$\begin{aligned} \rho(\Phi(\mathbf{r})) &= e \sum_i z_i c_i^{eq} \exp(-z_i \Phi(\mathbf{r})) \\ &= \frac{\kappa^2 z}{4\pi \ell_B} \sinh(-z \Phi(\mathbf{r})), \end{aligned} \quad (3.4.22)$$

where the latter expression holds true for symmetric  $z - z$  electrolytes. In that case, eq. 3.4.7 transforms in terms of discrete elements and cylindrical symmetry to

$$\begin{aligned} j_S^{solution}(\mathbf{r}_i) &= -\ell_B \int \rho(\Phi(\mathbf{r}')) \frac{\mathbf{r}_i - \mathbf{r}'}{|\mathbf{r} - \mathbf{r}'|^3} \cdot \hat{\mathbf{n}} dV \\ &= - \sum_{j \in \mathbf{V}} \frac{r_j \kappa^2 z \sinh(-z \Phi(\mathbf{r}))}{\pi (A - B) \sqrt{AB}} [(-\Delta z_{ij} n_{i,z} + (2Ar_j - B(r_i + r_j)) n_{i,r}) E(m) \\ & \quad + r_j n_{i,r} (-2A + 2B) K(m)] 2\pi r_j \Delta V_j \end{aligned} \quad (3.4.23)$$

$$\begin{aligned} j_S^{particles}(\mathbf{r}_i) &= -\ell_B \int \sigma(\mathbf{r}') \frac{\mathbf{r} - \mathbf{r}'}{|\mathbf{r} - \mathbf{r}'|^3} dS \\ &= - \sum_{j \in \mathbf{S}} \frac{4r_j \sigma(\mathbf{r}_j) \ell_B}{(A - B) \sqrt{AB}} [(-\Delta z_{ij} n_{i,z} + (2Ar_j - B(r_i + r_j)) n_{i,r}) E(m) \\ & \quad + r_j n_{i,r} (-2A + 2B) K(m)] 2\pi r_j \Delta A_j \end{aligned} \quad (3.4.24)$$

$$j_S^{imposed}(\mathbf{r}_i) = 2\pi \ell_B \sigma_i, \quad (3.4.25)$$

### 3. Algorithm and implementation

---

where  $\Delta V_j$  and  $\Delta A_j$  denote the volume and the area of element  $j$ , such that the integration element is given by  $dV = 2\pi r_j \Delta V_j$  and  $dA = 2\pi r_j \Delta A_j$  for the volume and surface integral respectively.

Besides the cylindrical symmetry, we also implemented a two-dimensional Cartesian coordinate system, for which only the Green's-function had to be adopted. The algorithm is also capable of performing all of the calculations in three dimensions. We have also implemented periodic boundary conditions using zero-flux boundary conditions combined with a minimum image convention for nearest neighbor interactions.

#### 3.4.3. The configuration file

For the sake of easy usage, we offer the complete user interface via a simple, easy to use, configuration file, where the system properties are defined. This allows for the simulation of a large number of input parameters without needing to modify and recompile the source code.

The file consists of different sections which we will now describe. The `[solver]` settings directly invoke the solution of the systems of equations, specifying the Successive Over-Relaxations parameter  $\alpha$  as well as the target relative accuracy  $\Delta$ .

The `[mesh]` section deals with the mesh input and offers possibility of refining the mesh, either globally or using adaptive refinement. Symmetry specifies the kernel of the solver, where 2 implies the cylindrical symmetry of the two-dimensional mesh. The `boxLength` needs to be specified only in the case where periodic images (nearest neighbor interactions) are calculated.

The `[system]` deals with the most important specifications, namely the Bjerrum length  $\ell_B$  and the inverse Debye length  $\lambda_D$ . `epsilon` is the value of the relative solution permittivity, on which all other relative permittivities are based. The number `[NPart]` specifies the number of iterated boundary types (in most cases this is the number of particles in the system). These boundary types need to have a physical index  $\geq 2$  specified in the mesh-file (chapter 3.3).

Finally the characteristics of each iterated boundary needs to be specified, namely the relative permittivity with respect to the solution permittivity and the surface charge density in term of  $[\sigma] = e/\lambda_D$ .

## Sample configuration file

```

# Config file for iPBS

# Settings for the iPBS solver
[solver]
# Parameter for Successive Overrelaxation (SOR) in [0;2]
alpha_sor = .67
# Accuracy we want to reach
tolerance = 5e-5
newton_tolerance = 1e-10

[ mesh ]

filename = "grids/2sphere2d.msh"
global_refinement_level = 0
adaptive_refinement_steps = 0
adaptive_refinement_fraction = 0.17
symmetry = 2
boxLength = 10

[ system ]
# Debye and Bjerrum length in [nm],
# colloid charge in [e]/debye_length

verbose = 0
# 0 - salt case enabled ; 1 - counterions
salt = 0
NPart = 2
lambda = 1
bjerrum = 1
epsilon = 1

# boundary types like specified in msh-file
# note: 0 always sets zero dirichlet
#       1 always sets zero flux
# others are used to model colloidal particles

[ boundary_2 ]
charge_density = .2
epsilon = .5

[ boundary_3 ]
charge_density = .01
epsilon = .0125

```



## 4. Verification

To verify both the algorithm and the implementation we analyzed the results obtained by the IPBS solver in various test-cases. In the first part we consider a single isolated spherical colloid. In that case the solution should match to that of a constant surface charge density boundary condition due to symmetry. Therefore we solved the nonlinear Poisson–Boltzmann equation with our solver implemented in DUNE without iterating the boundary condition. Instead we applied a constant flux boundary condition and compared the results to those obtained by employing the iterative procedure. Furthermore we compared the solution of the IPBS implementation for the salt-free limit ( $\kappa^{-1} \rightarrow \infty$ ) to a well established numerical solver, that can in principle reach machine precision. An analytical approximation to the electrostatic potential can be achieved by linearization in the limit of small values of the potential (Debye–Hückel approximation  $ephi \ll 1$ ) and in the case where the radius of the sphere is large compared to the screening length (Gouy–Chapman limit,  $\kappa a \rightarrow \infty$ ). Comparing our numerical results allows us to both verify the accuracy of our the implementation while testing the range of validity of these approximations.

In the second part we present an analytical approximation in the Debye–Hückel limit of the potential between two infinite charged walls. We show that for finite distances the effective field at the surface differs significantly from that caused by a constant surface charge density in absence of the second wall and that IPBS is able to recover the correct potential. The analytical approximation can also include a dielectric mismatch between the walls and the surrounding solution and the results the results again are in good agreement with our IPBS solver. We also show that the infinite walls can be approximates by finite line charges which reproduces the Gouy-Chapman result. This in turn is used as another test of our Poisson-Boltzmann solver.

### 4.1. A single spherical particle

We performed a first test of the accuracy of the implementation by determining the potential around a single spherical colloid. Due to symmetry all contributions of the electric field caused by the counter-ions must cancel and the effective b.c. should be equal to that of a constant surface charge density, i. e. the resulting effective surface charge density sould be ( $\sigma^{\text{eff}} = \sigma$  in eq. 3.4.7). We compared the solution of both methods making use of the spherical symmetry for a system with a screening length  $\lambda_D = 1$  nm, a sphere of radius  $a = 5\lambda_D$  and a total charge  $Q = 10$  e.

#### 4. Verification

---

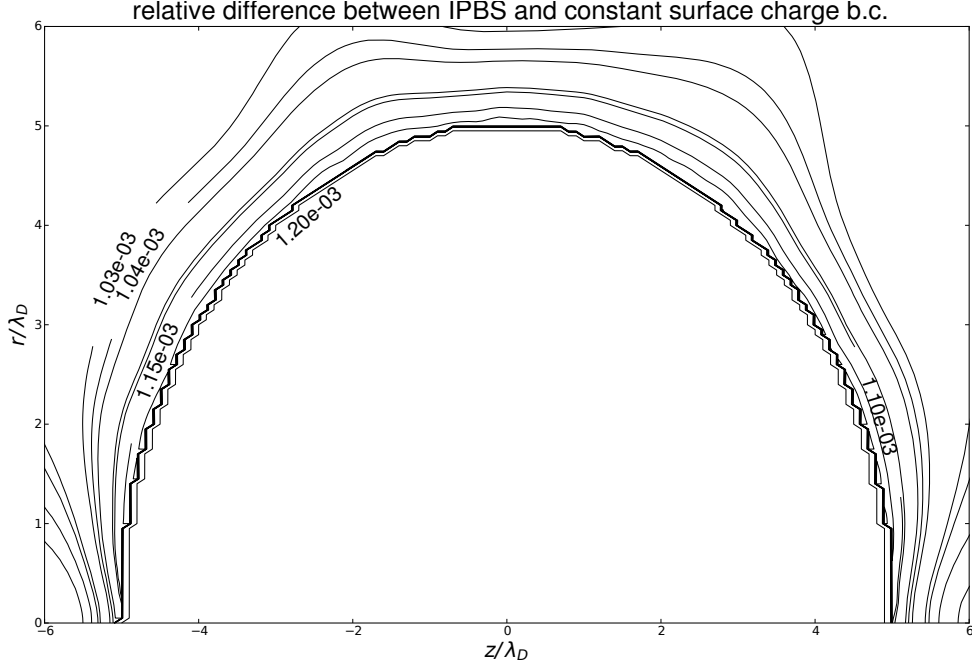


Figure 4.1.1.: The nonlinear Poisson–Boltzmann equation has been solved with constant surface charge (Neumann) boundary condition and with the IPBS algorithm for a sphere of radius  $\kappa a = 5$  and  $Q = 10$  e. The relative error shown here can easily be reduced to about  $10^{-3}$  by refinement (here we used about 40.000 elements, so that the sphere is approximated by 1500 linear segments).

We found that differences at distances larger than the screening length  $\lambda_D$  are negligible as numerical errors in the calculation of the interactions are of the same order. In figure 4.1.1, the relative difference between both solution methods is shown, which we explain by two contributions. The quite homogeneous distribution corresponds to an offset in the surface potential caused by averaging the ion distribution over the elements, resulting in an effective charge  $\sigma^{\text{eff}}$  which is slightly too small as the flux contribution given by the ions is given by (eq. 2.3.8),

$$j_S^{\text{solution}}(\mathbf{r}_i) = - \int \frac{\kappa^2}{4\pi\ell_B} \sinh(-z_i\Phi(\mathbf{r})) \frac{\mathbf{r}_i - \mathbf{r}'}{|\mathbf{r} - \mathbf{r}'|^3} \cdot \hat{\mathbf{n}} dV. \quad (4.1.1)$$

However, this error induced by our algorithm can be minimized easily by an appropriate refinement of the sphere's surface, such that the surface elements are smaller and thus the flux through the surface can be calculated more accurately. The results shown in fig. 4.1.1 suggest that for a reasonable resolution of the sphere's surface the resulting offset is less than a relative deviation of  $10^{-3}$  and can be disregarded for most practical purposes.

The second contribution, causing an increase of the deviation near the  $z$ -axis

of the cylindrical coordinate system is induced by the diverging behaviour of the elliptic integral in eq. 3.4.21 at  $r = 0$ . We verified this assumption by solving Poisson's equation with the surface flux set via eq. 3.4.7 and neglecting the solution contribution. A comparison to constant surface charge density b.c. shows that in this case, the homogeneous offset previously described vanishes while the asymmetric behaviour at the axis remains unaltered. However the relative deviation highly localized to the region near the axis of symmetry and therefore affects the solution only locally in the order of  $10^{-3}$ .

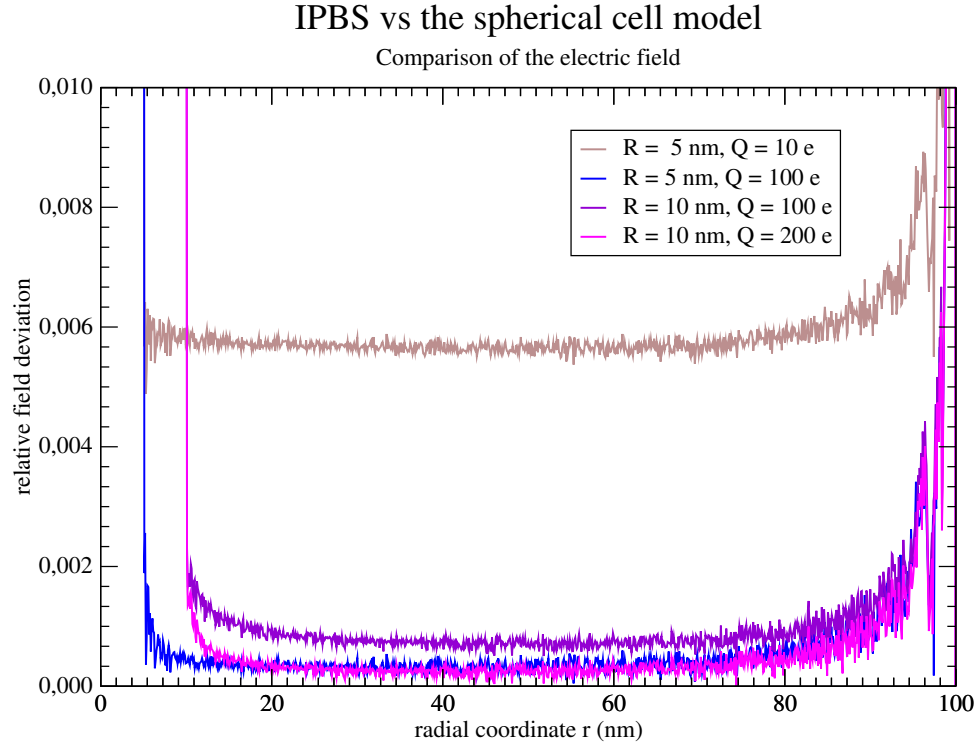


Figure 4.1.2.: The electric field of a spherical colloid has been determined using IPBS and a solver for the salt-free cylindrical cell model. The cell boundary was located at  $r = 100$  nm where a zero flux b.c. was used for the IPBS calculations. Shown is the relative deviation of both solution methods for spheres of different radius  $R$  and charge  $Q$ , where the screening length  $\kappa^{-1}$  was set to  $10^5$  nm.

To further verify the quantitative results we obtain with our implementation, we also compared the results to a numerical code developed by Deserno et. al. [20, 6]. This solver uses an iterative solution method to solve for the salt-free spherical cell model [21], i. e. the charge of the colloid is exactly compensated by the counter-ions present within a spherical cell around it. The numerical procedure is inspired by Alexander et. al. [3] and can in principle be tuned to arbitrary accuracy. The algorithm assumes an initial charge

#### 4. Verification

---

distribution from which the actual potential can be calculated. Then the ion distribution is determined and the scheme is iterated until it converges.

The salt-free limit can be modeled as a system in contact with a reservoir with a vanishing salt concentration, thus enforcing a huge screening length  $\kappa^{-1} \rightarrow \infty$ . However we found that the electric field  $\mathbf{E}(\mathbf{r}) = -\nabla\phi(\mathbf{r})$  does not differ significantly compared to the cell model for  $\kappa^{-1} > 10^5$  nm. Figure 4.1.2 shows the relative deviation in the electric field between the two solution methods. Besides an offset located at the surface the solutions agree excellently for the different parameters. This off set however is most likely due to the diskretization in the finite element method since the errors are of the order of less a per mill next to the surface, as one would expect. The deviations farther from the colloid however are artefacts the diskretization at the boundary and the calculation of the relative deviation, so we can state that the IPBS to be able to reproduce the salt-free spherical cell model.

There exists no analytical solutions of the Poisson–Boltzmann equation in spherical geometries in closed form [62], there are however several approximate expressions widely used in the literature. For small values of the potential  $\phi \ll 1$ , the Poisson–Boltzmann equation can be linearized, resulting in the Debye–Hückel potential (see chapter 2.4),

$$\phi(x) = \ell_B Z \frac{\exp(\kappa a)}{1 + \kappa a} \frac{\exp(-\kappa x)}{x}, \quad (4.1.2)$$

where we introduced the distance  $x = |\mathbf{r} - \mathbf{R}|$  to the sphere's origin located at  $\mathbf{R}$ .

Figure 4.1.3 shows the solution of the nonlinear Poisson–Boltzman equation obtained with IPBS and the corresponding Debye–Hückel potential, where we used a charge of  $Q = 10$  e, such that the resulting surface potential in the Debye–Hückel approximation,

$$\phi_S(a) = Z/\ell_B (a + \kappa a^2), \quad (4.1.3)$$

can be linearized. As the figure shows, the IPBS implementation is capable of reproducing the trend of the Debye–Hückel potential perfectly, showing only a small but constant offset at the surface. This offset has already been diskussed above and for a mesh where the semicircle is approximated by 1000 linear segments is less than 0.5%.

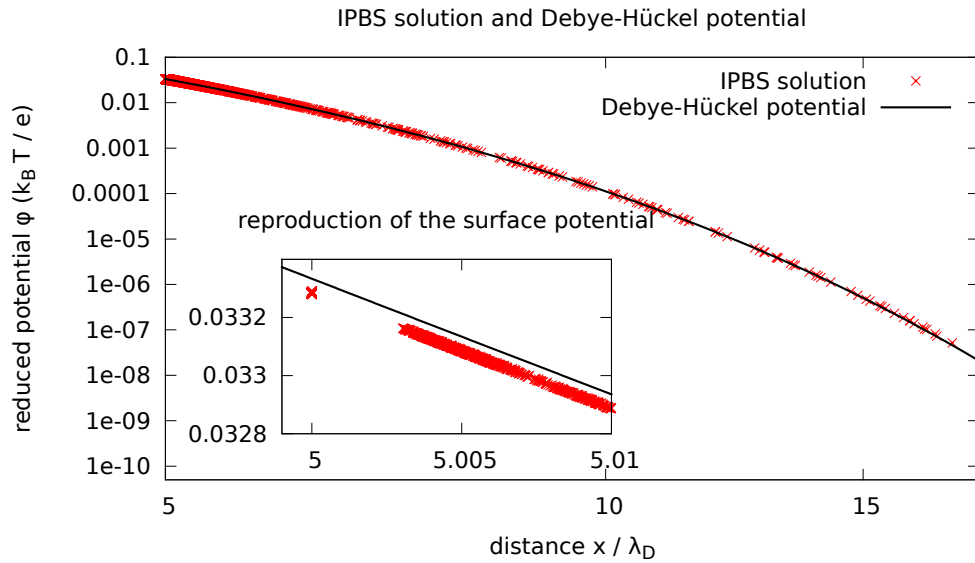


Figure 4.1.3.: The solution of the nonlinear Poisson–Boltzmann equation obtained via the IPBS algorithm is compared to the DH-approximation for a single spherical particle of radius  $a = 5$  nm and  $Q = 10$  e at a screening length  $\lambda_D = 1$  nm. The inset shows the reproduction of the surface potential predicted by the linearized theory where the relative difference between both results strongly depends on the mesh resolution.

#### 4. Verification

---

Having verified that we can in principle reproduce the qualitative trend of the linearized Poisson–Boltzmann equation, we can now proceed to the investigation of different parameter ranges. There are two characteristic parameters in 4.1.3, the surface charge density on the one hand (given by the ratio  $Z/a$ ), and the ratio between sphere radius and the screening parameter ( $\kappa a$ ) on the other hand. We compared the dependency of the surface potential  $\phi_S$  to  $\kappa a$  for a sphere of radius  $a = 5\lambda_D$  for three values of  $Z$ , which are definitely inside ( $Z = 0.1$ ), on the border ( $Z = 1$ ) and outside ( $Z = 10$ ) of the regime where linearization is reasonable.

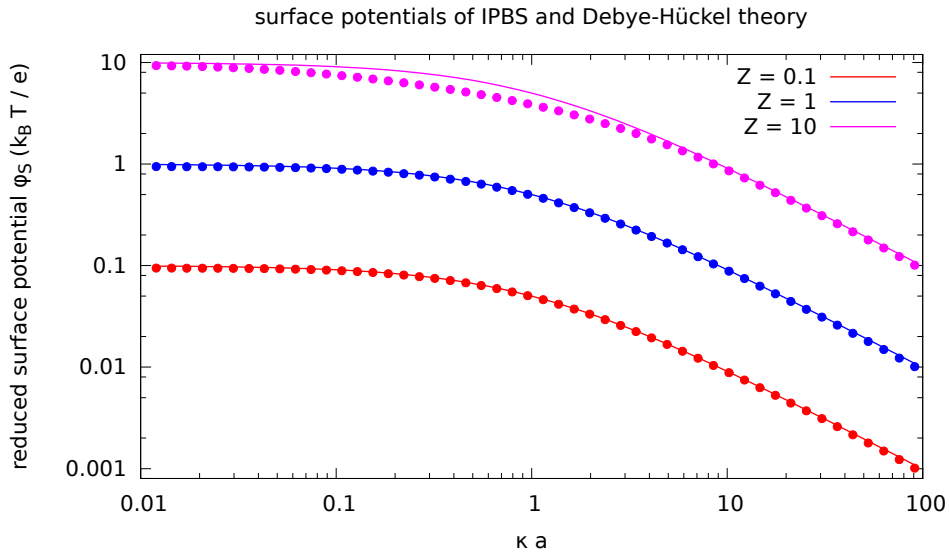


Figure 4.1.4.: Surface potential of a sphere of radius  $a = 5\lambda_D$  as a function of the screening length  $\kappa a$  for values inside ( $Z = 0.1$ ), on the border ( $Z = 1$ ) and outside ( $Z = 10$ ) of the regime of linearization. The curve for  $Z = 1$  fits remarkably well although linearization becomes questionable for these values, while for  $Z = 10$  nonlinear effects become clearly visible.

Figure 4.1.4 shows the nearly perfect reproduction of the sphere's surface potential for small values of  $\phi_S$ . For small values of  $\kappa a$  the potential approaches a non-screened Coulomb's potential, which is long-ranged due to its  $1/x$ -behavior and therefore the influence of the finite simulation box of size  $L = 25\lambda_D$  with the boundary condition  $\phi(25\lambda_D) = 0$  leads to a systematic error of order  $1/L = 5\%$ . We also note that the values of  $\phi_S$  for  $Z = 1$  still fits remarkably well, while for  $Z = 10$  nonlinear effects can be seen clearly, as expected.

Another approach to the potential of a single spherical particle can be performed in the limit of very large spheres compared to the screening length,  $\kappa a \gg 1$ . In this case the surface of the sphere can be treated as a plane intersection, such that the result of Gouy

and Chapman, eq. A.1.14, becomes valid.

In the Gouy-Chapman solution, the surface potential depends nonlinearly on the surface charge density,

$$\phi_S^{\text{GC}} = \frac{2}{z} \operatorname{arcsinh} \left( \frac{\ell_B z 2\pi}{\kappa} \sigma \right) \quad (4.1.4)$$

while in the linearized Debye-Hückel solution the surface potential is given by

$$\phi_S^{\text{DH}} = 4\pi \ell_B z \frac{\sigma}{z} \left( \frac{a}{1 + \kappa a} \right). \quad (4.1.5)$$

The last term in the latter expression,  $\left( \frac{a}{1 + \kappa a} \right)$ , introduces the curvature of the sphere to the linearized surface potential, while in the limit  $\kappa a \rightarrow \infty$  it will converge to  $\frac{1}{\kappa}$ , being consistent with the linearization of eq. 4.1.4.

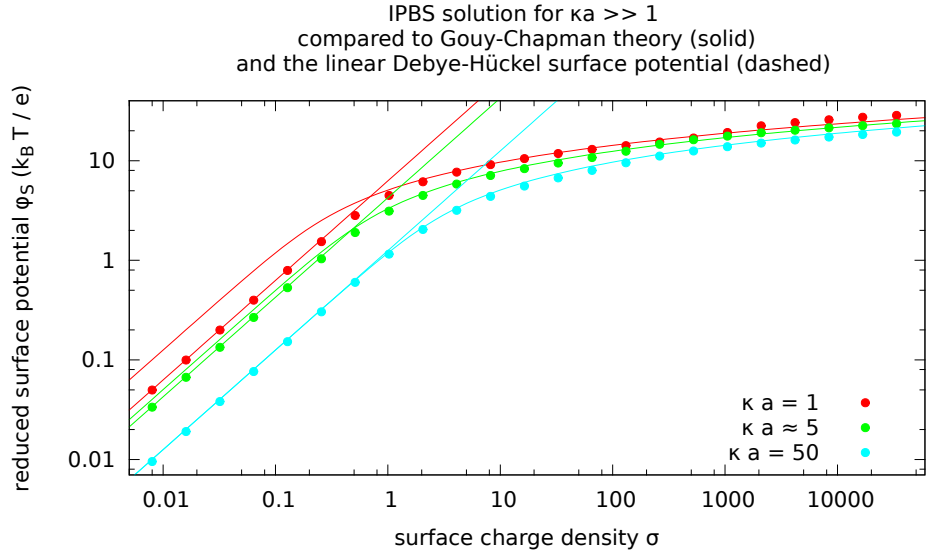


Figure 4.1.5.: Surface potential of spheres for different values  $\kappa a$ . For  $\kappa a \gg 1$  the surface can be treated as being flat, approaching the validity of the Gouy-Chapman solution, whereas the linearized solution of Debye and Hückel is valid for arbitrary  $\kappa a$ , but only for small values of  $\phi_S$ , i.e. small surface charge densities  $\sigma$ . The plot shows values of  $\kappa a$  that are clearly inside, on the border and outside the regime where the Gouy-Chapman approach is valid. The deviations for large values of  $\phi_S$  appear due to linearization artefacts and are explained more in detail in the text.

Assuming a monovalent symmetric salt,  $z = 1$ , fig. 4.1.5 shows the expected behavior in the nonlinear regime, verifying the Newton-method used for solving the nonlinear system

#### 4. Verification

---

of equations appearing in the Galerkin formulation 3.1.7. For high curvature only the linearized result of the Debye-Hückel potential fits well to the calculated data in the case of small surface charge densities. For small curvature, the IPBS solution reproduces the Gouy-Chapman result perfectly. In fact, Rouzina and Bloomfield [61] showed that the twodimensional behaviour of the surface is recovered for  $\kappa a \geq 25$ . Fluctuations, that are observed for very high surface charge densities  $\sigma > 1000 \frac{e}{nm^2}$ , are expected appear due to the strong nonlinearity at the surface, where errors in the linearization of the surface elements are induced. This influence can be neglected for our kind of studies as such surface charge densities are unreachable in the physical systems we are interested in.

We also note, that the characteristic mesh length on the surface of the sphere,  $l_c$ , should be smaller than the Debye length,  $l_c \ll \lambda_D = 1/\kappa$  using polynomial ansatz-functions of first degree in order to determine the correct surface potential. We also tested using polynomial ansatz-functions of higher degree, but for our setup it tends to increase the numerical effort as the number of elements can't be drastically reduced as in the numerical integration of the volume flux, the charge density is averaged over one element, and therefore larger elements will increase the error in the ion-density profile. Therefore we decided to use linear ansatz-functions, which proved to be quite effective for our purposes

## 4.2. Planar symmetry

In this chapter we will use planar symmetry to test our algorithm and implementation. For an infinite charged plane, there exists an analytical solution (see appendix A.1) by Gouy [31], 1910, and Chapman [17], 1913. The electrostatic repulsion between two identical planes can be approximated via two approaches, the one valid for large distances  $h$  between the planes, neglecting any interactions between the planes and thus resulting in a linear superposition of the Gouy-Chapman potentials of each plane. The other one, based on the linearization of the Poisson–Boltzman equation, is only valid for small surface potentials.

### 4.2.1. A single planar surface

Modeling a single planar surface, we used different approaches, again using two-dimensional representations of the system. A first test was performed in a Cartesian coordinate system, using a flat wall at the boundary of the box. That way we could verify the finite element backend, imposing the surface charge density on the surface to be constant. Then, using the iterative algorithm, we that verified both the IPBS solution and the constant charge solution match the predictions of Gouy-Chapman theory.

For further tests, which also delivered detailed information on the implementation of cylindrical and Cartesian symmetries, we wanted to built a symmetric object representing an infinite charged wall filling a half-space. As an approximation we used a stick in a two-dimensional Cartesian coordinate system, and a disk in the three-dimensional cylindrical coordinate system making use of the symmetry (see fig. 4.1(a)).

The error introduced to the electric field outside of the plane by this approximation can be calculated analytically. Using Green’s function in two dimensions, the electric field  $\mathbf{E}(x)$  of an infinite charged wall at position  $x = 0$  results in

$$\mathbf{E}(x) = -\frac{\partial}{\partial x}\phi(x) = -\frac{\partial}{\partial x}\left(4\pi\ell_B \int_{-\infty}^{\infty} \frac{\sigma}{2\pi} \ln\left(\sqrt{x^2 + y^2}\right) dy\right) = \ell_B\sigma, \quad (4.2.1)$$

while for a finite stick the integration yields

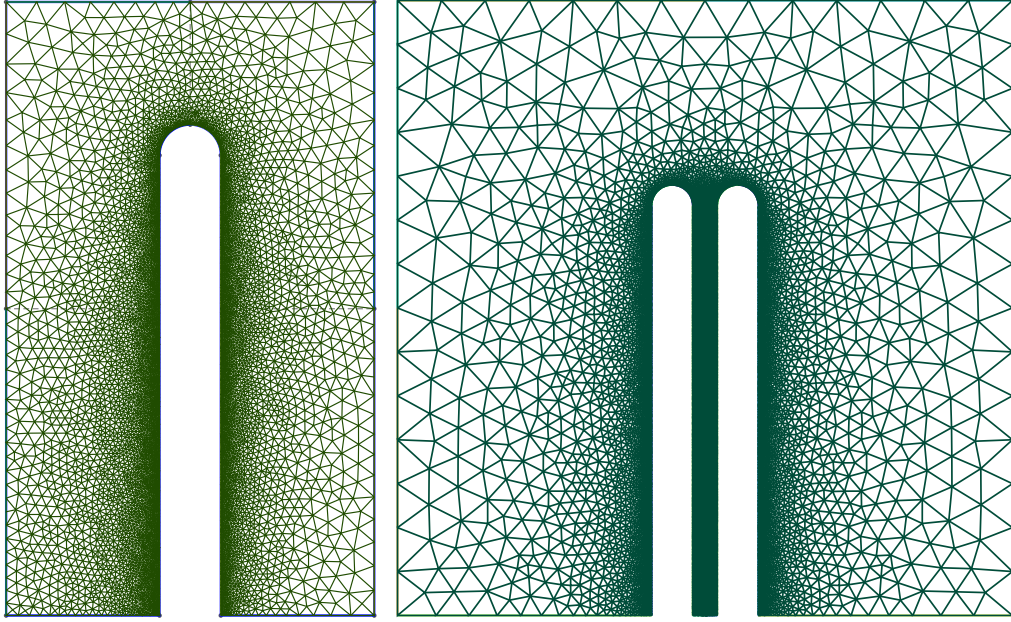
$$\begin{aligned} \mathbf{E}(x) &= -\frac{\partial}{\partial x}\phi(x) = -\frac{\partial}{\partial x}\left(4\pi\ell_B \int_{-y_{max}}^{y_{max}} \frac{\sigma}{2\pi} \ln\left(\sqrt{x^2 + y^2}\right) dy\right) \\ &= \frac{2}{\pi}\ell_B\sigma \operatorname{arctanh}\left(\frac{y_{max}}{x}\right) \xrightarrow{y_{max} \rightarrow \infty} \ell_B\sigma. \end{aligned} \quad (4.2.2)$$

Analogously, we can perform the same calculation for the disk in cylindrical coordinates,

$$\begin{aligned} \mathbf{E}(z) &= -\frac{\partial}{\partial z} \int_{-r_{max}}^{r_{max}} \int_0^\pi \frac{\ell_B\sigma\delta(z)}{r^2 + r'^2 + 2rr' + (z - z')^2 - 4rr'\sin(\theta)} d\theta dr \\ &= \frac{\pi r_{max}}{\sqrt{r_{max}^2 + 1}} \xrightarrow{r_{max} \rightarrow \infty} \pi. \end{aligned} \quad (4.2.3)$$

#### 4. Verification

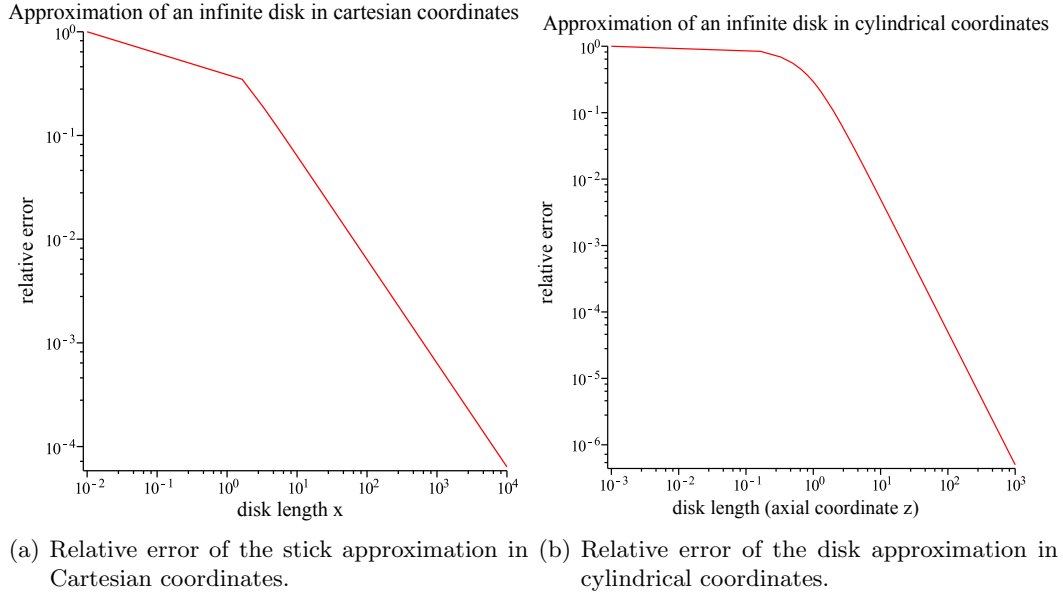
---



- (a) A single stick both suitable for Cartesian and cylindrical coordinate calculations.
- (b) For simulating two charged sticks/disks, the mesh resolution between the two particles must be high enough ( $l_c \ll \kappa$ ), so that the gradient at the intersection nodes fits the flux boundary conditions.

Figure 4.2.1.: An infinite charged plane has been modeled by a stick (Cartesian symmetry) and a disk (in cylindrical coordinates) respectively. The element resolution on the surface must be significantly smaller than  $\lambda_D$ , while the ratio between wall width and wall height determines the accuracy of approximating a infinite wall by a finite stick.

Figure 4.2.2 shows the asymptotic behavior of this integration both for cylindrical and Cartesian coordinate systems. As expected, the error decays faster for the disk, as after integrating in  $\theta$ , the disk has a diameter of  $2r_{max}$  and an area of  $4\pi r_{max}^2$ , which should better approximate a plane than the two-dimensional line-segment of length  $y_{max}$ . As seen in the figure, a relative error of less than one percent for the stick geometry can only be reached with a ratio of the typical length-scale,  $l_c$ , of about  $y_{max} > 1000l_c$ , while for a disk geometry we only need to satisfy  $r_{max} > 7l_c$ , which quantitatively reduces the number of mesh elements by a about 10000. Therefore we decided to show once that both the Cartesian and the cylindrical symmetry are capable to reproduce the Gouy-Chapman potential, and then simply use the cylindrical disk for modeling planes. That way we can also combine the geometrical properties, i.e. simulate a spherical particle in front of a wall or similar setups. This is another case where the symmetry considerably helps simplifying the system.



(a) Relative error of the stick approximation in Cartesian coordinates.  
 (b) Relative error of the disk approximation in cylindrical coordinates.

Figure 4.2.2.: The relative error of the finite integration limits when approximating an infinite charged plane by a stick, or a disk respectively, decays quite fast. As we have to use a ratio of the typical length scale of the system to the length of the stick of about 100 to get a relative error of less than one percent for the stick, for the disc to get a similar error requires only a ratio of about seven

A verification that both geometrical setups using the IPBS algorithm reproduce the Gouy-Chapman potential is shown in figure 4.2.3. We have used quite coarse meshes and a “short” stick intentionally to present an impression of the resulting errors. Also shown is the solution of a quadratic box, on which one boundary has been chosen to carry the iterative surface charge.

#### 4. Verification

---

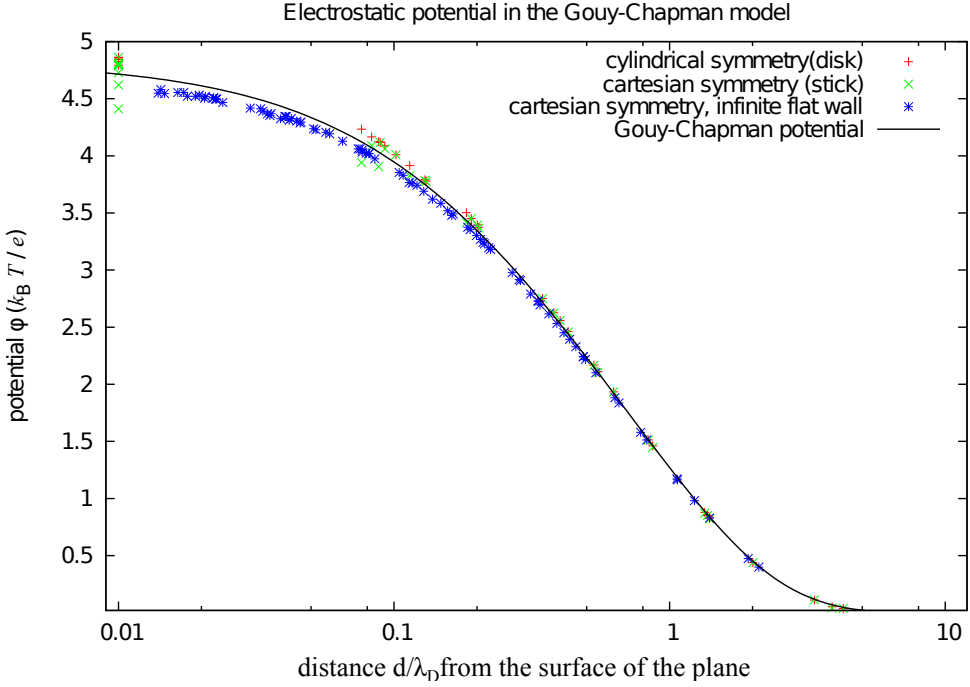
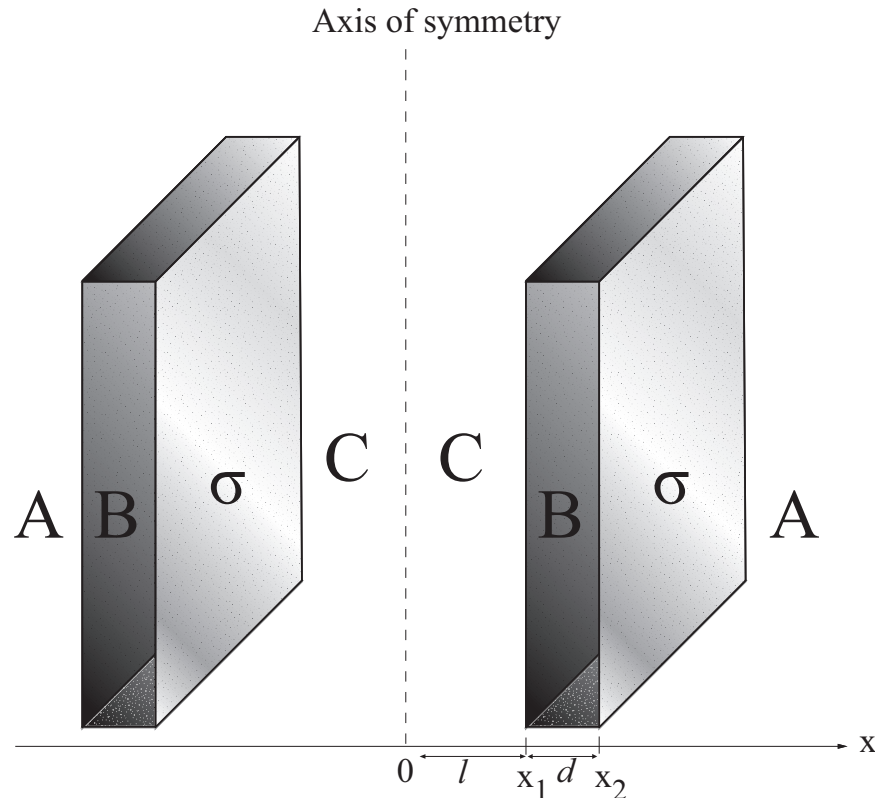


Figure 4.2.3.: The Gouy Chapman solution is reproduced in all three setups used for planar surfaces. A very coarse mesh ( $N \leq 8000$  elements) was used to illustrate the different types of errors introduced. For a simple flat border, the nonlinear effects become dominant close to the surface. The finite size of the box, which in the corners leads to huge deviations in the integrated ion density, results in an underestimation of the surface potential. For modeling both the stick and the disk, the same mesh was used, setting the wall ten times as high as broad, illustrating the much better approximation of the sphere, although a slight overestimation of the surface potential can be observed due to the coarse mesh. For distances  $d \gg \lambda_D$ , the solutions become practically indistinguishable.

### 4.2.2. The potential between two plane surfaces

Having verified that we can solve planar symmetries, we can now perform a first test on the algorithm itself, turning to systems where the effective surface charge will be affected by the iterative procedure. As a simple test-case, we modeled two planar disks (fig. 4.1(b)), for which in the case of small surface charges the potential can be calculated analytically for the case of monovalent symmetric salt through linearization.



Areas: A - outside, B - inside disk, C - between disks

Figure 4.2.4.: Using symmetry, the one-dimensional potential curve can be calculated analytically for the three different regions A, B and C, as marked in the figure.

Making use of the symmetry, we can divide the system in three parts (fig. 4.2.4), on which we can solve the linearized equations. In the domain outside of the disk,  $\Omega_A$ , the Poisson–Boltzman equation of a flat surface must be solved, whereas in the inside of the disk,  $\Omega_B$ , which we assume to be non-penetrable by ions, we have to solve Poisson's equation. In the region  $\Omega_B$  between both disks, we can use the linearity of the electrostatic potential and use a linear combination of the potential of both disk surfaces resulting in

#### 4. Verification

---

a set of equations,

$$\frac{d^2}{dx^2}\phi(x) = \kappa^2 \sinh(\phi(x)) \quad x \in \Omega_A \quad (4.2.4)$$

$$\frac{d^2}{dx^2}\phi(x) = -4\pi\ell_B\sigma\delta(x - x_2) - 4\pi\ell_B\sigma\delta(x - x_1) \quad x \in \Omega_B \quad (4.2.5)$$

$$\frac{d^2}{dx^2}\phi(x) = \kappa^2 \sinh(\phi(x)) + \kappa^2 \sinh(\phi(-x)) \quad x \in \Omega_C, \quad (4.2.6)$$

where we used the symmetry of the solution in the origin. Using the linearized Gouy-Chapman result and the fact that the field between two parallel plates is linear, we can rewrite this system of partial differential equations as a problem of determining the coefficients of the known solutions in the partial domains,

$$\phi_A(x) = A \exp(x - x_2) \quad (4.2.7)$$

$$\phi_B(x) = B_1(x - x_1) + B_2 \quad (4.2.8)$$

$$\phi_C(x) = C \frac{\cosh(\kappa x)}{\cosh(\kappa x_1)}, \quad (4.2.9)$$

which delivers a continuity condition. Gauss' law yields two more equations for the jump of the electric field, at the surface,

$$\begin{aligned} \left. \frac{d\phi_A(x)}{dx} - \frac{d\phi_B(x)}{dx} \right|_{x=x_1} &= 4\pi\sigma \\ \left. \frac{d\phi_B(x)}{dx} - \frac{d\phi_C(x)}{dx} \right|_{x=x_2} &= 4\pi\sigma \end{aligned} \quad (4.2.10)$$

Solving eq. 4.2.10 together with the continuity of the potential obtained from eq. 4.2.9 yields

$$\phi_A(x) = 4\pi \frac{\sigma}{\kappa} \left( 2 - \frac{2 + \kappa d}{1 + \kappa d + \coth(\kappa l)} \right) \exp(-\kappa(x - x_2)) \quad (4.2.11)$$

$$\begin{aligned} \phi_B(x) &= 8\pi\sigma \left( 2 - \frac{2 + \kappa d}{1 + \kappa d + \coth(\kappa l)} \right) (x - x_1) \\ &\quad + 4\pi \frac{\sigma}{\kappa} \left( \frac{2 + \kappa d}{1 + (1 + \kappa d) \tanh(\kappa l)} \right) \end{aligned} \quad (4.2.12)$$

$$\phi_C(x) = 4\pi \frac{\sigma}{\kappa} \left( \frac{2 + \kappa d}{1 + (1 + \kappa d) \tanh(\kappa l)} \right) \frac{\cosh(\kappa x)}{\cosh(\kappa l)} \quad (4.2.13)$$

Figure 4.2.5 shows the result of our IPBS solver both for constant surface charge and for the iterative determination of the surface charge, which shows excellent agreement with the results of our analytical results of eq. (4.2.11) - (4.2.13). This problem would be a typical example where the constant surface charge density assumption fails as soon as the planes start interacting.

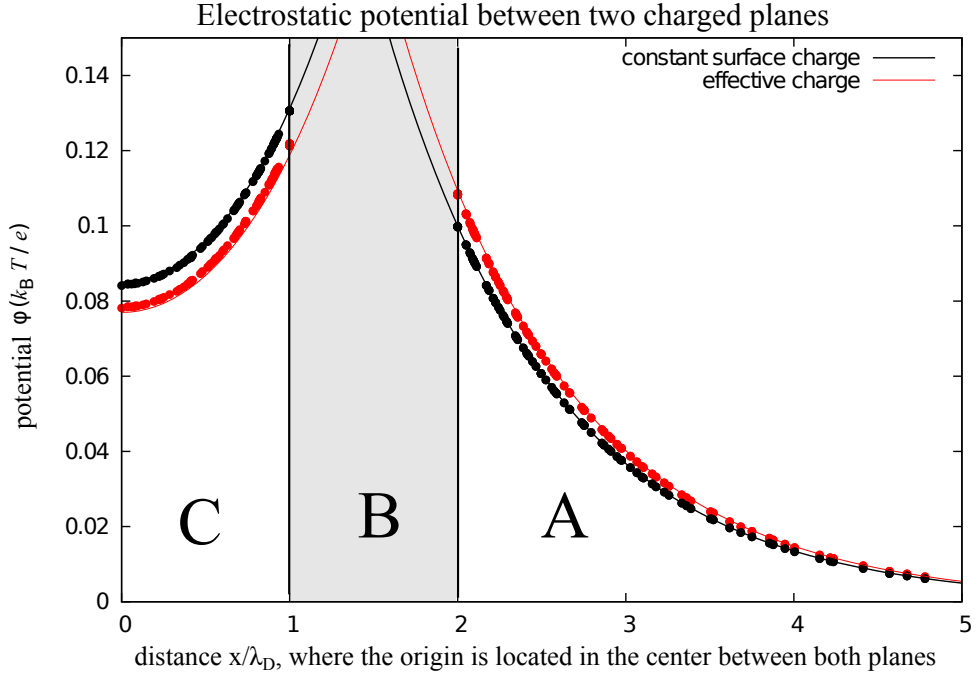


Figure 4.2.5.: The electrostatic potential of two charged planes at a distance  $\kappa l = 1$  and thickness  $\kappa d = 1$  calculated both for constant surface charge and with the iterative method determining the effective surface charge, showing excellent agreement with our calculations. The surface charge density  $\sigma = 0.1/(4\pi) \frac{e}{\text{nm}^2}$  was chosen such, that the potential can be linearized without introducing errors (units measured in a system where  $\ell_B = \lambda_D$ ).

Under the assumption of constant surface charge density, the potential can be calculated using the Gouy-Chapman result on the outside border of the plane, and determining the constant  $C$  in eq. 4.2.9 by

$$\frac{d}{dx} A \frac{\cosh(\kappa x)}{\cosh(\kappa l)} \Big|_{x=l} = A \coth(\kappa l) \equiv 4\pi\sigma. \quad (4.2.14)$$

The effective surface charge density can be obtained by

$$\sigma_1^{\text{eff}} = \frac{d}{dx} \phi_A(x) \Big|_{x=x_2} \quad (4.2.15)$$

$$\sigma_2^{\text{eff}} = \frac{d}{dx} \phi_C(x) \Big|_{x=x_1}, \quad (4.2.16)$$

where charge neutrality demands

$$\sigma_1^{\text{eff}} + \sigma_2^{\text{eff}} = 2\sigma. \quad (4.2.17)$$

### Including dielectric contrast

The model system 4.2.4 can be extended to situations where the plane has a different dielectric permittivity than the surrounding medium. In the case of the linearized Poisson–Boltzman equation, the resulting system of equations still can be solved analytically, modifying eq. 4.2.10 for dielectric mismatch yields

$$\begin{aligned} \varepsilon_{out} \frac{d\phi_A(x)}{dx} - \varepsilon_{in} \frac{d\phi_B(x)}{dx} \Big|_{x=x_1} &= 4\pi\sigma \\ \varepsilon_{in} \frac{d\phi_B(x)}{dx} - \varepsilon_{out} \frac{d\phi_C(x)}{dx} \Big|_{x=x_2} &= 4\pi\sigma, \end{aligned} \quad (4.2.18)$$

where with  $\varepsilon_{in}$  and  $\varepsilon_{out}$  we denote the relative dielectric constant inside and outside of the plane respectively. The solution of the system of equations then offers the possibility of verifying that our algorithm and implementation correctly reproduces the induced surface charge density for systems with dielectric mismatch.

In order to clearly verify the influence of the polarization, the two planes had to be quite close ( $\kappa l = 0.5$ ). The required number of elements therefore quickly grows, as errors due to coarse meshes as discussed in the previous section quickly become significant, nevertheless IPBS is able to handle such systems and converge to the expected results. Figure 4.2.6 shows the electrostatic potential obtained for a thickness  $\kappa d = 3$  of the disks for a surface charge density  $\sigma = 0.01/(4\pi) \frac{e}{nm^2}$ , which is chosen such that the potential can be linearized without introducing errors.

The relative permittivity of the solution was set to  $\varepsilon_1 = 1$ , while for the wall we used a good dielectric material ( $\varepsilon_2 = 1/10\varepsilon_1$ ), a bad dielectric material ( $\varepsilon_2 = 80\varepsilon_1$ ) and the case without mismatch ( $\varepsilon_2 = \varepsilon_1$ ). Excellent agreement with the analytical solution can be observed, showing the expected convergence of the solution for a bad dielectric material towards the solution of a constant surface charge density, as the induced surface charge will exactly tend to compensate the flux through the surface invoked by the external charges.

For the case without mismatch in the dielectric properties, the solution differs slightly from the analytical result, but this is purely caused by the small distance, as in figure 4.2.5 such a deviation could not be observed. For a good dielectric material this error is amplified as the number of iteration steps needed to reach the same relative accuracy will be larger, but still it shows a very good agreement with the theoretical prediction.

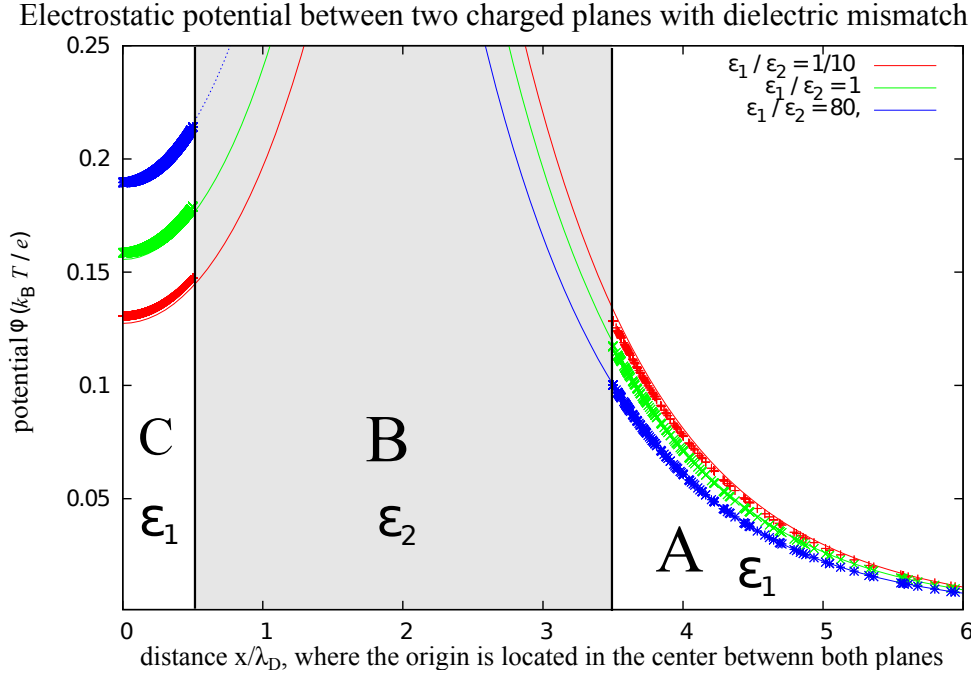


Figure 4.2.6.: The electrostatic potential of two charged planes at a distance  $\kappa l = 1/2$  and thickness  $\kappa d = 3$  has been calculated for a surface charge density  $\sigma = 0.01/(4\pi \frac{e}{nm^2})$  chosen such, that the potential can be linearized without introducing errors (again, the unit system is chosen such that  $\ell_B = \lambda_D$ ). The relative permittivity of the solution was set to 1 while for the wall we used a good dielectric material ( $\varepsilon_2 = 1/10\varepsilon_1$ ), a bad dielectric material ( $\varepsilon_2 = 80\varepsilon_1$ ) and the case without mismatch ( $\varepsilon_2 = \varepsilon_1$ ).

An excellent agreement with the analytical solution can be observed, however we note that for small distances between the plates, the errors due to the finite size of the walls and the mesh resolution in the center become important during the iterative calculations. As expected, the error vanishes for the case of a bad dielectric as the induced charge will compensate the influence of the contributions  $E_{ext}$ , and therefore the solution converges rapidly to the same as for constant surface charge without iterating  $\sigma_{eff}$



## 5. The two-colloid problem

Having verified the implementation and accuracy of the algorithm, we now turn to the physically interesting problem of determining the force acting between two spherical, charged mesoscopic particles (colloids) suspended in an electrolyte solution. The effective interaction potential for these systems has often been expressed in terms of a Yukawa potential [68] and can be measured directly in experiments by force measurements using optical tweezers [32] [42] [23]. However the question of the influence of multi-body effects within the Poisson Boltzmann description has yet to be studied in detail [39].

In this chapter, we will address this issue and, in addition, examine the influence of a jump of the dielectric constant across the surface of the colloidal particles on the effective force between them. To the best of our knowledge this problem has not been examined so far in the framework of the Poisson-Boltzmann mean-field description with proper boundary conditions at the surface.

### 5.1. The force in the effective surface charge density model

#### 5.1.1. Force calculation method

According to the predictions of the DLVO theory (chapter 2.5), the interaction of spherical macro-ions of radius  $a$  within the linearized Poisson–Boltzman description can be described by an effective interaction potential [19][71],

$$v_{\text{eff}}(x) = Z'^2 \ell_B \frac{\exp(-\kappa x)}{x}, \quad (5.1.1)$$

where  $x$  denotes the separation between the particle centers. The bare charge  $Z$  is reduced by the screening of the counter-ions within the double layer to an effective charge,

$$Z' = \frac{\exp(\kappa a)}{1 + \kappa a} Z. \quad (5.1.2)$$

Consequently, the pairwise forces acting between two colloids are given by

$$F_{\text{eff}}(x) = Z^2 \ell_B \left( \frac{\exp(\kappa a)}{1 + \kappa a} \right)^2 \left( \frac{\exp(-\kappa x)}{x^2} + \kappa \frac{\exp(-\kappa x)}{x} \right). \quad (5.1.3)$$

From the solution of our iterative finite element method, the force acting on colloidal particles in an electrolyte solution can be calculated via the stress tensor, which in fact

## 5. The two-colloid problem

---

can be considered as a sum of two parts, the osmotic and the electrostatic contribution [22]. First we will consider only the electrostatic contribution to the force.

The electrostatic force acting on a single particle can be obtained by making use of the Maxwell stress tensor,

$$\sigma_{ij} = \frac{1}{4\pi\ell_B} \left( E_i E_j + \frac{1}{2} E^2 \delta_{ij} \right). \quad (5.1.4)$$

Using the reduced electrostatic units, the force acting on a unit volume can then be obtained by

$$\beta \mathbf{f} = \nabla \cdot \boldsymbol{\sigma}, \quad (5.1.5)$$

so that the force on a particle can be obtained using Gauss's theorem,

$$\beta \mathbf{F}_p = \oint_{\partial S} \boldsymbol{\sigma} \cdot \hat{\mathbf{n}} \, dS \quad (5.1.6)$$

$$\simeq \sum_i \boldsymbol{\sigma} \cdot \hat{\mathbf{n}}_i 2\pi r_i \Delta A_i, \quad (5.1.7)$$

where the last term shows the discretized formulas of the integration over the finite element boundary intersection, each having an area  $\Delta A_i$ , in cylindrical coordinates. In our implementation, the integration is performed by summing over all surface elements belonging to that particle and taking the element normal vector of each element.

Here we note that the use of linear ansatz functions for the finite element method turned out not to be satisfactory. This is due to the fact that eq. 5.1.4 requires the calculation of the electric field at a given position  $\mathbf{r}$ ,

$$\sigma_{ij}(\mathbf{r}) = \frac{1}{4\pi\ell_B} (\partial_i \phi(\mathbf{r}) \partial_j \phi(\mathbf{r}) + (\partial_i \phi(\mathbf{r}))^2). \quad (5.1.8)$$

Using P1 elements, the derivatives at each of the element nodes are constant, i.e., in element-local coordinates we can only obtain correct values (in the sense of element-wise linear ansatz-functions) for the gradients at the node positions and the center of the elements. The DUNE framework offered an easy way of changing the finite element method to use ansatz-functions of polynomial degree  $k$  and in all our tests  $k = 2$  or at most  $k = 3$  met the requirements for a sufficient force calculation.

The other crucial quantity is the discretization of the surface  $\partial S$ , as this obviously will influence the integration 5.1.7. However we found that a discretization which is satisfactory for obtaining the correct iterated boundary condition via eq. 3.4.5 near the surface also conforms with that requirement.

As Bell and Levine [12] showed, a force due to the gradient of osmotic pressure is acting on charged colloidal particles suspended in an electrolyte solution. The change in the osmotic pressure at a given position,

$$\Delta\Pi(\mathbf{r}) = \Pi(n_i(\mathbf{r})) - \Pi(n_{0,i}) \quad (5.1.9)$$

where  $n_i$  denotes the ion number density and  $n_{0,i}$  is equilibrium concentration of ion species  $i$ , is resulting from the redistribution of those ions, which remain in the medium when double layers are formed. If a Boltzmann distribution is assumed, the change is given by

$$\Delta\Pi = k_B T \sum_i (n_i - n_i^\infty), \quad (5.1.10)$$

where the number density at position  $\mathbf{r}$  in the Poisson–Boltzman description is given by  $n_i(\mathbf{r}) = n_{0,i} \exp(-z\Phi(\mathbf{r}))$  and for a symmetric salt of valency  $z$ , the osmotic pressure change is given by

$$\beta\Delta\Pi = 2n_{i,0} (\cosh(z\Phi(\mathbf{r})) - 1). \quad (5.1.11)$$

Using the relation

$$\frac{1}{\ell_B \lambda_D^2} = \frac{4\pi\ell_B \sum_i z_i n_{i,0}}{\ell_B} = 4\pi \cdot 2n_0, \quad (5.1.12)$$

we can easily introduce the force due the difference of osmotic pressure compared to equilibrium acting on a surface element into a resulting stress tensor,

$$\beta\mathbf{T} = \beta(\boldsymbol{\sigma} + \Delta\Pi \mathbf{1}) \quad (5.1.13)$$

$$= \frac{1}{4\pi\ell_B} \left( \left( \frac{1}{\lambda_D^2} (\cosh(z\phi) - 1) + \frac{1}{2} \mathbf{E}^2 \right) \mathbf{1} - 2\mathbf{E} \otimes \mathbf{E} \right). \quad (5.1.14)$$

It can be verified by a straight-forward calculation [22], that

$$\nabla \cdot \mathbf{T} = 0, \quad (5.1.15)$$

so that the integral does not need to be taken over the particle's surface but any surface enclosing the particle. However, we also considered integrating the effective stress tensor along the mid-plane between the particles but as the accuracy achieved was satisfactory, we iterated along the elements characterizing the surface of the particles.

To check the correct implementation of the force measurement we compared the results obtained with the predictions of DLVO theory. We should note here, that the DLVO theory includes both effects, electrostatic as well as osmotic contributions (chapter 2.5). Figure 5.1.1 shows the ability of the IPBS implementation to reproduce the force obtained via the DLVO potential 5.1.3 for system parameters ensuring small surface potentials and small average overlap of the diffuse Debye layers.

Using identical particles and symmetry arguments, the system can be reduced to a mesh containing only a single particle, having a center to center distance  $x$  to its mirrored picture and a radius  $\kappa a = 1$ . To quantify our results we used parameters accessible in common experiments, namely  $\ell_B = 1$  nm and  $a = 10$  nm. To ensure that the potential is sufficiently small to compare to the linearized case, we set the surface charge density to a very small value,  $\sigma = 10^{-3}$  e/nm<sup>2</sup>. The figure shows an excellent agreement of our results with the DLVO prediction for distances  $\kappa x > 3$ , i.e. when the surface-surface separation is larger than the extension of the Debye layer. For smaller separations, the

## 5. The two-colloid problem

---

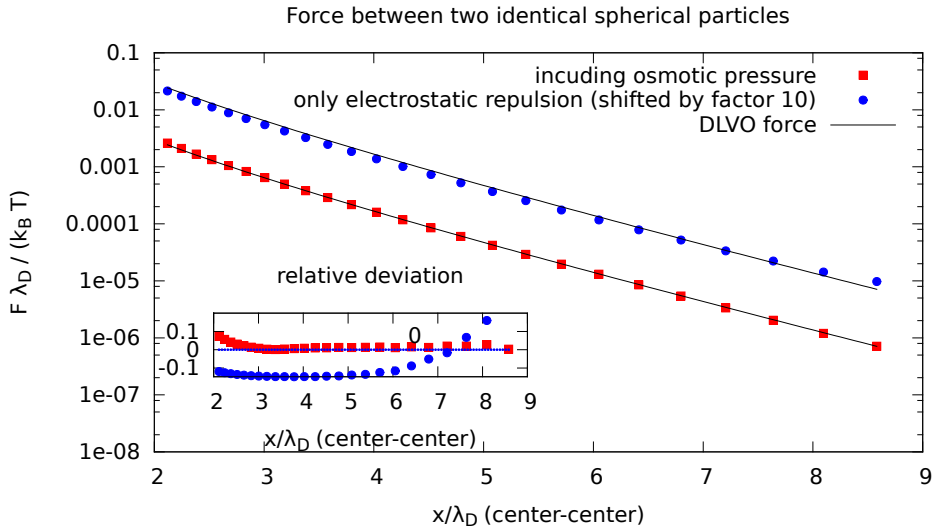


Figure 5.1.1.: The force between two identical spherical particles compared to the predictions of DLVO theory, regarding both only electrostatic interactions (shifted by a factor of 10) and the version also taking care of the osmotic pressure. The relative error in the inset shows that our implementation is capable of reproducing the Debye–Hückel force while neglecting entropic effects leads to an underestimation of the resulting force for small distances and an overestimation for large ones. The increase of the error for  $x > 3\lambda_D$  is simply caused by numerical fluctuation in the integration.

average overlap of the Debye layers of each particle cannot be neglected and therefore the concept of charge renormalization (see chapter 2.5) cannot be applied. The increasing relative error for larger separations shown in the inset is due to increasing numerical errors when determining the forces, which at huge separations, become extremely small.

In figure 5.1.1, we also plotted the force acting on the particle when only electrostatic interactions are taken into account, i.e. integrating only the Maxwell stress tensor over the particle's surface. Here we can nicely show the influence of the asymmetric counter-ion distribution. The ions are dragged into the space between the two colloids and thus, the osmotic pressure results in an additional repulsion which is not found when considering only electrostatic interactions. This behaviour would be the other way round for the case of the colloids being far apart from each other and close to the boundary, as here counter-ions will also collect in the space between the colloids and the boundaries of the computational domain where charge-neutrality is assumed. This repulsion from the boundary, resulting from the fact that the counter-ions need to compensate the electric field of the colloid is also included by the assumption of being in equilibrium with a reservoir by the DLVO

theory. We checked that we are not effected by this finite size behaviour by doubling the box size, still showing perfect agreement.

The failure of the resulting force when only considering electrostatic interactions at large separations of the colloids, where the resulting force is over-estimated, is related to the boundary condition at the boundary of system, where the electric field is set to zero. The absence of osmotic pressure results in a screened repulsive potential, but with a different interaction potential which could be obtained by solving another minimization problem similar to that in chapter 2.5. The effect of entropic contributions can also be seen in figure 5.1.2, where we plotted the effective ion density  $n_{\text{eff}}(\mathbf{r}) = n_+(\mathbf{r}) + n_-(\mathbf{r})$  in the  $r$ - $z$ -plane for a separation of 40 nm. Within half a Debye length of the surface, the ion distribution remains remarkably symmetric, but in the center between both particles a significant increase of the ion density can be observed compared to a single free particle.

### 5.1.2. Effective ion density and overlap of Debye layers

To check at which distance the overlap of the Debye layers will give a significant contribution, we defined a sphere around the colloids whose radius is set to be half of the center-center separation (see fig. 5.1.3) and calculated the charge within this shell,

$$Z^* = \int_0^{2\pi} \int_0^\pi \int_a^{x/2} n_{\text{eff}}(r, z) dr dz d\alpha \quad (5.1.16)$$

and checked at which distance the colloidal charge is neutralized by the circumjacent ion cloud for a single particle in the previously described setup (figure 5.1.4).

In the case of the linearized Debye–Hückel solution, the ion density is known and can easily be integrated within such a cell,

$$Q(r) = Ze \left( 1 - \frac{\exp(\kappa a)}{1 + \kappa a} \ell_B(1 + \kappa r) \exp(-\kappa r) \right). \quad (5.1.17)$$

We can now examine the influence of nonlinear effects on the ion distribution and at which distances the Debye layers are expected to have a strong overlap. We calculated the charge compensation for the simple system of a single isolated colloid whose radius we set by  $\kappa a = 1$ . In the limit where linearization is applicable, i. e. for a very low surface charge density  $\sigma = 0.001 \frac{e}{\text{nm}^2}$  at  $\lambda_D = 10 \text{ nm}$ , 5.1.4 shows, that the system behaves as expected as the charge density around the colloid perfectly fits the linearized expression. However, a system modeling a typical colloidal particle, where the total colloidal charge is set to  $Z = 255$  ( $\sigma = 0.123 \frac{e}{\text{nm}^2}$ ) and  $\lambda_D = 40 \text{ nm}$ , shows a strong influence of the nonlinearity, inducing an increased ion density near the colloid. However, we found that if separation distance between two colloids is larger  $\kappa x \approx 10$ , they can be treated decoupled, meaning that the overlap of the Debye layers is negligible as can be extracted from fig. 5.1.4.

Having assessed that the density profile of the micro-ions is influenced by the presence of a second colloidal particle if the distance is less than  $\kappa x \approx 10$ , we will now quantitatively characterize the influence of boundary conditions to the solution of the finite

## 5. The two-colloid problem

---

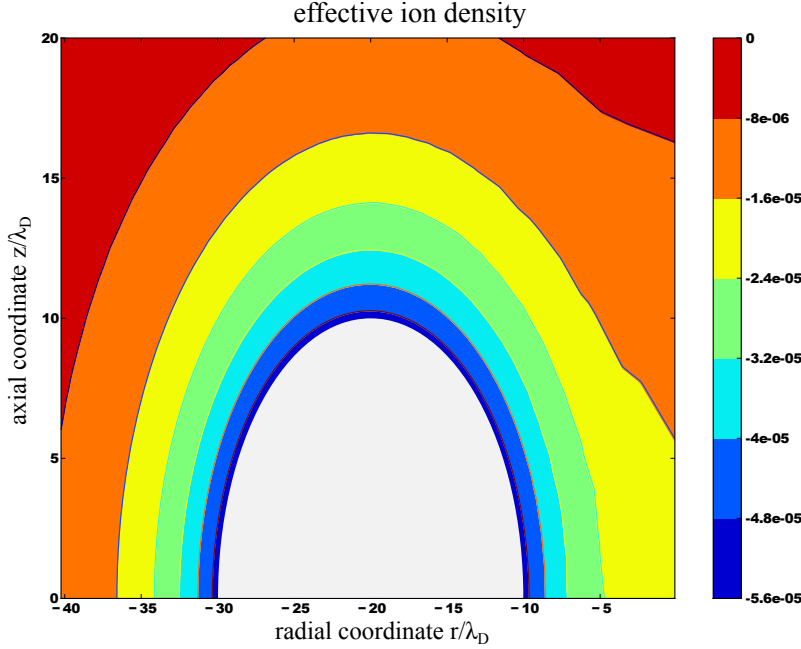


Figure 5.1.2.: The effective ion density  $n_+ + n_-$  of two spherical, equally charged particles,  $Z = 4\pi/10$  e of radius  $a = 10$  nm at a center-center distance of 40 nm and  $\lambda_D = 10$  nm. Within half a Debye layer the ion distribution remains rather symmetric due to strong electrostatic interactions, for in the region between the two colloids a significant increase of the ion density compared to a single free colloid can be observed. The second colloid is located at  $r = 20\lambda_D$ , making use of the symmetry.

element procedure. As a reference we solved the nonlinear Poisson–Boltzmann equation for the system of two symmetrical particles described in the previous section under the assumption of each particle having a homogeneous constant surface charge density (figure 5.1.5).

For large separations, where the Debye layers on average have a small overlap such that the change in the density of micro-ions between the colloids can be neglected and the electrostatic influence of one colloid acting on the second can be assumed as being nearly independent of the position on its surface, the deviations are expected to be small. Indeed, we find that at surface-surface separations of about two Debye lengths (note that this is exactly the distance where the overlap of the Debye layers becomes weak), both solution methods are in accordance to the Debye-Hückel predictions within the numerical accuracy of the force determination.

For smaller separations, both the ions and the opposing colloid will influence the electric field at the colloid's surface. The electric field generated by the neighboring colloid

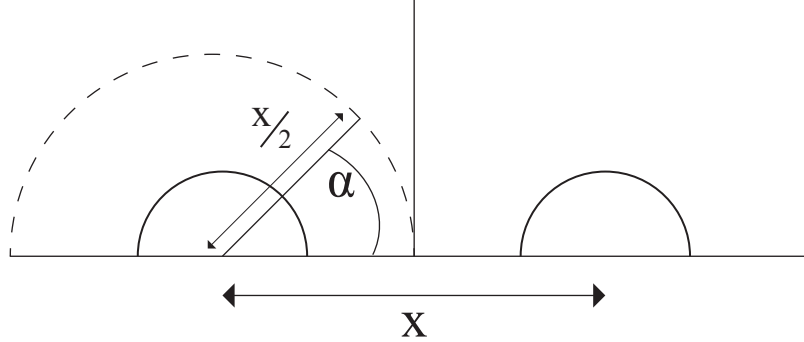


Figure 5.1.3.: A spherical shell around the colloidal particle of radius  $a$  separated from the second particle by a distance  $x$  can be defined such that its angular resolved charge density is a quantitative measure on the influence of overlapping Debye layers.

of same charge,  $E_{\text{col}}$ , results in a negative contribution to the surface flux,  $j = -E_{\text{tot}} \cdot \hat{\mathbf{n}}$  of an element, whereas the change of the local ion number density between the particles adds an additional field contribution,  $E_{\text{ion}}$ , due to the effective charge of opposite sign. For large separations, the two contributions will cancel on the surface,  $E_{\text{ion}} + E_{\text{col}}|_{\text{surface}} = 2\pi\ell_B\sigma$ , such that the boundary condition again simplifies to

$$j = 4\pi\ell_B\sigma. \quad (5.1.18)$$

Comparing the relative error of both calculation methods to the prediction of DLVO theory (inset in figure 5.1.5), it becomes evident that for separations  $x \geq \lambda_D$ , our iterative method perfectly reproduces the theoretical predictions, while the assumption of a constant electric field corresponding to eq. 5.1.18 shows significant differences even for separations  $x \geq 5\lambda_D$ . As we used the same mesh and parameters, the deviation shown in figure 5.1.5 shows that it is exactly that kind of system where our implementation will be able to recover the correct results and could establish possible new applications.

To examine further the effective boundary condition of the colloid,  $j_{\text{eff}}$ , we compared our solution to that obtained by equation 5.1.18 (figure 5.1.6). Shown is the relative difference  $(j_{\text{eff}} - 4\pi\ell_B\sigma) / (4\pi\ell_B\sigma)$  in percent for a system of two negatively charged particles (parameters as in the system above) for different values of  $\kappa x$  in dependence of the radial angle  $\alpha$  as defined in figure 5.1.3. At very strong overlap of the Debye Layers ( $\kappa x \leq 1$ ) the effect of the charge distribution contributes additively to the electric field between both particles, and corrections of the order of 10% can easily be reached. For the points on the colloid which are farthest from the other particle, the correction to the surface electric field is negative (thus resulting in a positive correction of the flux  $j$ ), corresponding to the increased effective density of counter-ions between the two colloids. Even for a distance of  $\kappa x = 2$ , where the exponential decay of the counter-ion density should give rise to a

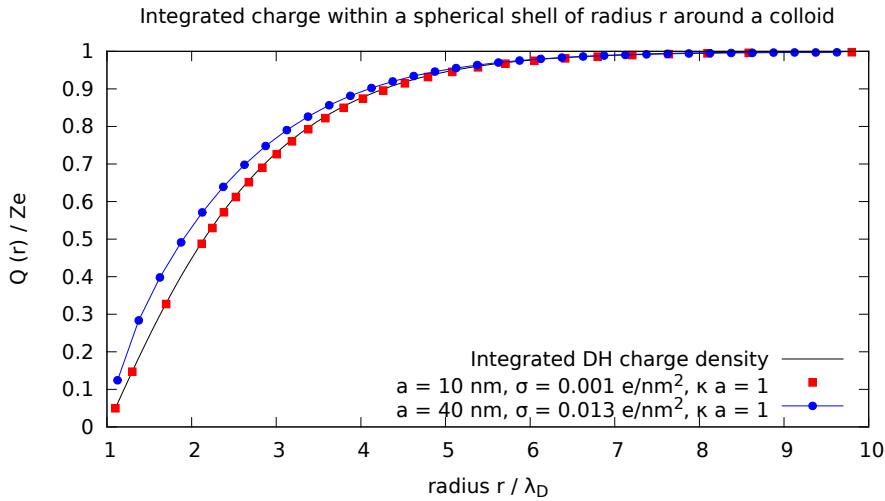


Figure 5.1.4.: Compensation of the colloidal charge by the integrated charge density within a spherical cell (fig. 5.1.3) around a spherical macro-ion. Red squares show the case suited for linearization ( $\sigma \ll 1 \rightarrow \phi \ll 1$ ), blue circles the system discussed in chapter 5.2, where nonlinear effects are expected to be relevant. Solid line shows the prediction of DH theory.

different behavior, the change is significant on the side facing the particles, while on the opposite side the correction can be neglected.

As our calculations show, at already separations  $\kappa x \gtrsim 5$  the influence on the boundary conditions can be neglected - the asymmetry observed can be explained by the diverging contribution of the elliptic integral (eq. 3.4.21) used during the calculations in reduced symmetry. This means that the assumption of a constant electric field all over the colloid surface can only be used if  $\kappa x \gg 1$ !

## 5.2. Colloidal charge renormalization

All the calculations concerning the interaction of two colloids presented so far were limited to the case where the Debye-Hückel linearization is applicable. Most physical systems of interest however, do not fulfill the requirement of small electrostatic interactions compared to thermal fluctuations,  $\phi \ll 1$ . Therefore we will now focus on the influence of nonlinear effects on colloidal interactions, which based on the prescription of Alexander et. al. [3], can be modeled accurately as interaction between Debye-Hückel like particles (chapter 2.5) even for highly charged colloids in more dense systems, provided that the colloidal charge is renormalized properly.

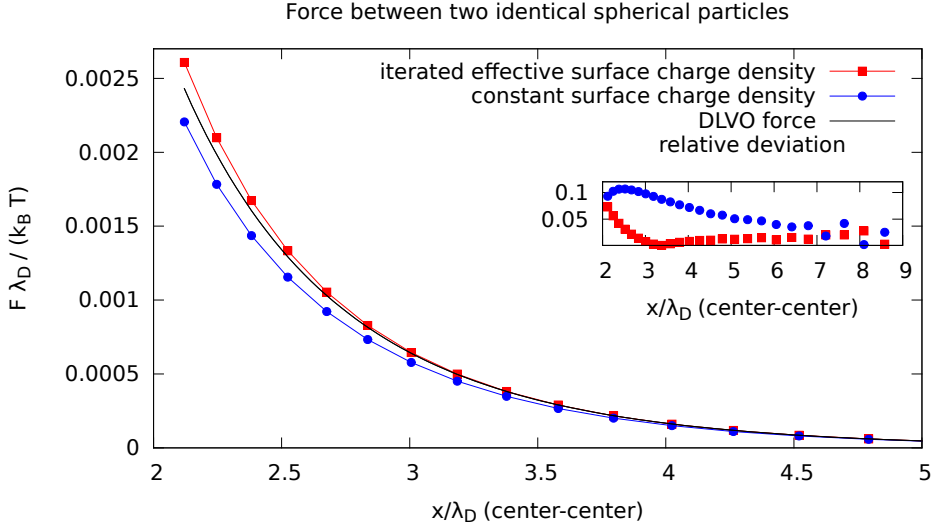


Figure 5.1.5.: The force between two identical spherical particles of a radius  $a = 1\lambda_D$  and a surface charge density  $\sigma = 0.001 \text{ e/nm}^2$  in a system with a screening length  $\lambda_D = 10 \text{ nm}$ . The assumption of a constant surface flux (eq. 5.1.18) shows significant deviations to the result of our iterative method (see text). In the inset the relative error compared to DLVO theory is shown.

In their famous work, Alexander et. al., essentially provided a numerical recipe on how to calculate the effective colloidal charge,  $Z_{\text{eff}}e$ , which is in general smaller than the colloid's bare charge,  $Ze$ , due to a dense counter-ion cloud surrounding the colloid, while salt renormalization effects can usually be neglected,  $\kappa_{\text{eff}} \approx \kappa$ . For dilute systems, a (spherical) Wigner–Seitz cell around the colloids can be defined, in which the net charge should be zero and which should look rather similar for different colloids. This corresponds to the fact that there is a steady state between electrostatic repulsion of the colloids and osmotic pressure, such that the colloids arrange having on average a certain region around which no other colloid will occupy. In such a Poisson–Boltzmann cell model the complicated many-particle system can be reduced to an effective one-colloid problem [53]. If interactions between such cells are neglected, the thermodynamic potential of the whole system is equal to the number of cells times the thermodynamic potential of one cell [68]. In such a cell model, it is sufficient to solve the Poisson–Boltzmann equation in a single cell assuming a net charge of zero per cell so that Gauss' law yields a zero flux boundary condition at the outer cell boundary[21].

The basic idea of Alexander et. al. to determine the effective colloidal charge  $Z_{\text{eff}}$  in order to apply an effective DLVO theory can then be summarized as that of matching the linearized solution of the Poisson–Boltzmann equation at the cell boundary to the

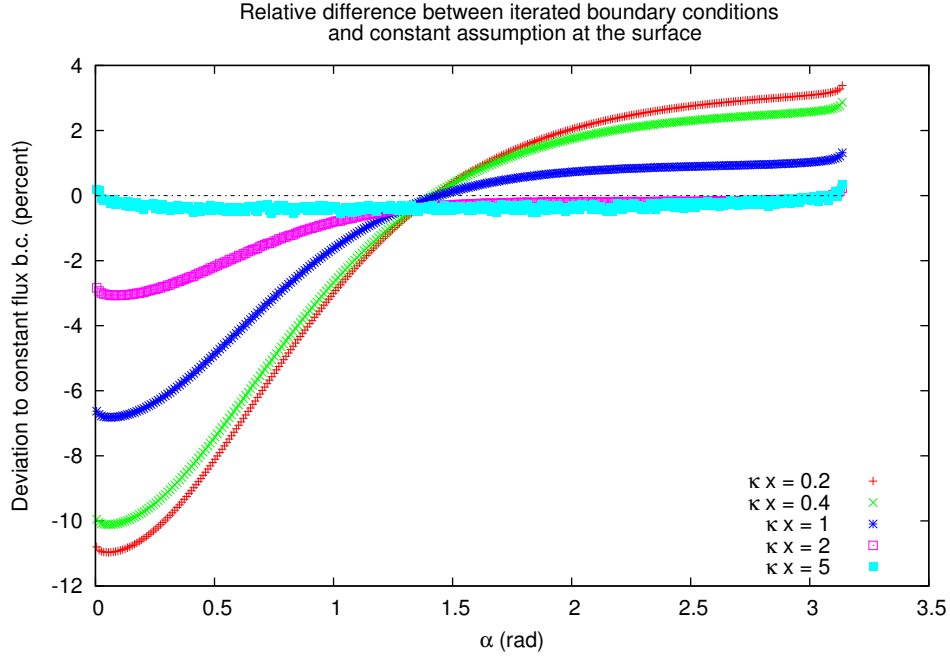


Figure 5.1.6.: The resulting iterated boundary conditions are compared to the naive one (eq. 5.1.18) by plotting the relative difference of the field values at the surface position defined by the angle  $\alpha$  (fig. 5.1.3. For strong overlapping Debye layers, a huge deviation can be observed due to the electric field of the effective charge contribution. Deviations visible for  $\kappa x = 5$  are artifacts of our numerical scheme.

nonlinear one and use that to calculate the effective charge of the colloid. The boundary value problem for the cell-model of cell radius  $R$  (monovalent salt, compare eq. 2.3.6) is then given by [68]

$$\begin{aligned} \nabla^2 \phi(x) &= \kappa^2 \sinh(\phi(x)) & a < x < R \\ \hat{\mathbf{n}} \cdot \nabla \phi(x) &= Z\ell_B/a^2 & x = a \\ \hat{\mathbf{n}} \cdot \nabla \phi(x) &= 0 & x = R. \end{aligned} \quad (5.2.1)$$

From the solution of the nonlinear problem one can then calculate the effective screening constant (eq. 2.3.7) at the cell boundary,

$$\kappa_{\text{cell}}^2 = 4\pi\ell_B (c_+(R) + c_-(R)) = \kappa^2 \cosh(\phi(R)). \quad (5.2.2)$$

Then, the linearized charge density (i.e. equation 2.3.8 linearized) can be integrated from  $R$  to  $a$  to obtain the effective ion charge in that Wigner-Seitz cell which, due to the

assumption of charge neutrality, is equal to the charge of the colloidal particle in the DLVO approximation.

Aubouy et al. [5] proposed an analytical estimate for this effective colloidal charge, which is asymptotically correct in the infinite dilution limit,  $\kappa a \gg 1$ . According to their calculations, the effective charge can be calculated from the bare charge  $Z$  and the salt concentration of the reservoir,  $\kappa$ , by

$$Z_{\text{eff}} = \frac{a}{\ell_b} \left( 4\kappa a t_Z + 2 \left( 5 - \frac{t_Z^4 + 3}{t_Z^2 + 1} \right) t_Z \right), \quad (5.2.3)$$

where the bare colloidal charge  $Z$  enters via the functional

$$t_Z = T \left( \frac{Z\ell_B/a}{2\kappa a + 2} \right) \quad (5.2.4)$$

and

$$T(x) = \frac{\sqrt{1+x^2} - 1}{x}. \quad (5.2.5)$$

In their publication Alexander et al. stated that equation 5.2.3 delivers accurate results for  $\kappa a \gtrsim 1$  and the screening length of the linearized cell-model,  $\kappa_{\text{cell}}$ , should tend to the reservoir screening length,

$$\kappa_{\text{cell}} \rightarrow \kappa, \quad (5.2.6)$$

if the potential at the boundary of a Wigner–Seitz cell can be assumed to vanish, i.e. if  $R - a \lesssim \lambda_D$  (sufficient screening).

We performed calculations using our iterative method for the force between two colloidal particles of charge  $Z = 255$  and radii  $a = \lambda_D/3$ ,  $a = \lambda_D$  and  $a = 5\lambda_D/3$  at a low salt concentration ( $60 \mu\text{mol}$ ) to test the expected pairwise additivity predicted by DLVO theory. The values of  $a$  are chosen such that they are respectively outside, at the border, and inside the prescription of Aubouy et al. (eq. 5.2.3), where the screening is implied to  $\lambda_D = 40 \text{ nm}$  by the choice of  $\ell_B = 0.96 \text{ nm}$ .

The algorithm perfectly reproduces a Yukawa force (figure 5.2.1) where it is intuitive to use only points at  $x > x_0$  to perform the fit as for distances where the colloids are nearly in contact neither our finite element procedure will give very precise results nor the theory predicts a strict Yukawa-like potential. On the other hand, the accuracy of our force calculation reduces drastically in the case of small forces and high surface charge density (see section 5.1.1), so only fitting the long tail does not work as well. As there is no obvious procedure for how to choose which points to include into the fit we examined the convergence of both  $Z_{\text{eff}}$  and  $\kappa$  in the fit and determined  $x_0$  accordingly. As expected from equation 5.2.6, the values of  $\kappa_{\text{cell}}$  differed only minimally from the bare  $\kappa$ , so we did the fit again in for a constant  $\kappa_{\text{cell}} = \kappa$ . The fitted values show perfect agreement with equation 5.2.3 in the range of its validity, but, remarkably, even  $\kappa a = 1/3$  seems to obey a DLVO potential very well.

## 5. The two-colloid problem

---

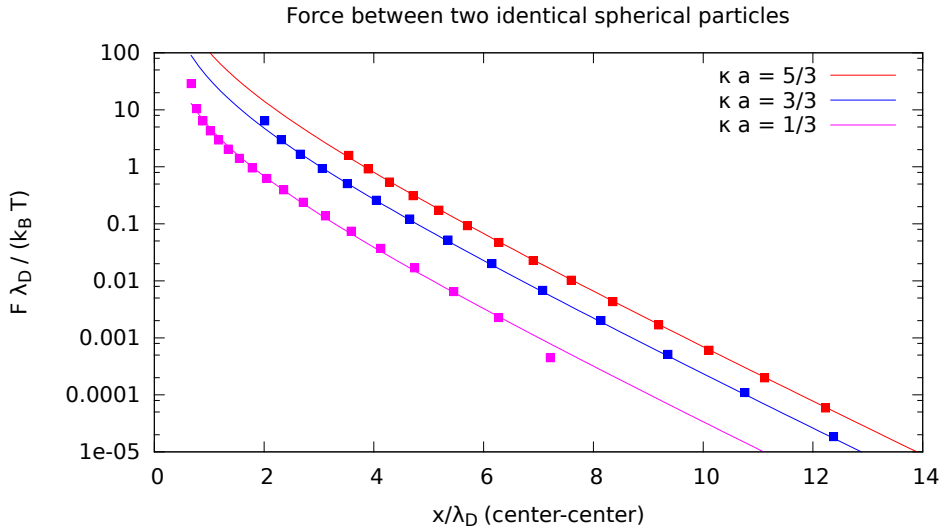


Figure 5.2.1.: The force between two identical spherical colloids for different values of  $\kappa a$  is shown, where the obtained values are fitted to an effective charge  $Z_{\text{eff}}$  according to DLVO theory. The fits were performed observing the best convergence using points  $x \geq x_0$  (see text), resulting fit parameters are shown in table 5.2.1. Deviations from fit for small forces are due to numerical errors during the force calculation.

In reference [44], Kreer et. al. reported about the influence of nonlinear effects in the interactions between isolated pairs of macro-ions using Molecular Dynamics simulations. As these results did not seem to be in accordance with expectations of the Alexander theory of renormalized charge, we tried to reproduce the simulation using our nonlinear solver algorithm which we have shown matches the predictions of Alexander's charge renormalization.

The setup consisted of macro-ions  $Z = 255$  of radius  $a = 10$  nm and ions  $Z_{\text{ion}} = \pm e$  of radius  $a/100$ . Using conditions of water at room temperature ( $\ell_B = 0.71$  nm) Kreer et al. varied the number of salt ions such that the total number of ions in the simulation box was

$$n_{\text{tot}} = Zn'_C + 2n_s \quad (5.2.7)$$

where  $n'_C$  is the number of macro-ions. We modeled the system assuming the simulation box is in contact with a salt reservoir such that the number of salt ions in the system is the same. For the salt-free case we fixed the concentration of co-ions such that the net-charge of the box is zero. The resulting parameters are shown in table 5.2.2.

To directly compare our simulation data, we calculated the quantity  $E(x) = \frac{1}{Z_e} F(x)$ ,

$x/\lambda_D$	$Z_{\text{eff}}$ (IPBS)	$Z_{\text{eff}}$ (eq. 5.2.3)	relative deviation
5/3	$238.5 \pm 0.1$	241.4	1.1%
3/3	$202.0 \pm 0.5$	208.0	2.8%
1/3	$99.4 \pm 1.0$	87.2	13.9 %

Table 5.2.1.: The results of our fits perfectly reproduce the prediction of Aubouy et al. in the range of its validity. Remarkably even for  $\kappa a < 1$  the calculated values do not show a large deviation from their theory, and are always lower than the bare charge  $Z = 255$ .

which we plotted on a logarithmic scale against the macro-ion separation in figure 5.2.2. Our fits to a DLVO potential (eq. 5.1.3) show excellent accordance for separations  $x \gtrsim \lambda_D$ , which is also expected due to the assumption of not having strong overlapping Debye layers (see chapter 2.5). Contrary to the results of Kreer et. al. , the solution of the full nonlinear Poisson–Boltzmann equation seems to be in accordance with the asymptotic matching of the linear potential proposed by Alexander. Furthermore, Kreer et al. reported an increase of the effective macro-ion charge with increasing salt concentration ([44], fig. 3). To investigate this phenomenon, we determined the effective charge  $Z_{\text{eff}}$  of the macro-ions using data points of separations  $x \geq 2.6a$  (table 5.2.2). We also extracted the force Kreer et. al. obtained by MD simulations (circles in figure 5.2.3) and performed a fit to eq. 5.1.3 (dashed line).

The results of our fits show an agreement between the finite element implementation and the analytical predictions within 5-10% while the effective charge obtained from the MD data differs significantly. Kreer et. al. claimed to have obtained a ratio  $Z_{\text{eff}}/Z > 1$  which we were not able to reproduce. Contrary, for all the examined salt concentrations we obtained  $Z_{\text{eff}} \lesssim 0.5Z$ .

A closer inspection of figure 5.2.3 indeed shows deviations from Debye-Hückel like behavior of the MD simulation data as well as the deviations in the behavior of effective charge compared to the prediction of Alexander theory. Their data suggests a monotonic increase of  $Z_{\text{eff}}$  with increasing salt concentration while both the analytical expression and IPBS data show the opposite. At small separations, deviations to the mean-field behavior could be expected due to correlation effects in the distribution of the micro-ions in the explicit simulation, but these effects should limit to a range  $x \lesssim \kappa^{-1}$  due to screening effects. Also, the charge density of  $255 \text{ e}/(4\pi 10^2 \text{ nm}^2) \approx 0.2 \text{ e}/\text{nm}^2$  is not exceptionally high, and we estimate correlation effects to be weak, i.e. the Poisson–Boltzmann predictions should still be valid. The huge deviations can also not be explained by a failure of the cell model charge renormalization concept as reported, as also our simulation considered an isolated pair of macro-ions in a charge-neutral box (i.e. zero flux b.c.) of linear dimension  $L = 160 \text{ nm}$ . We verified that there is no influence of finite size effects by comparing the results to those of using a box of doubled length. Our results more likely

## 5. The two-colloid problem

---

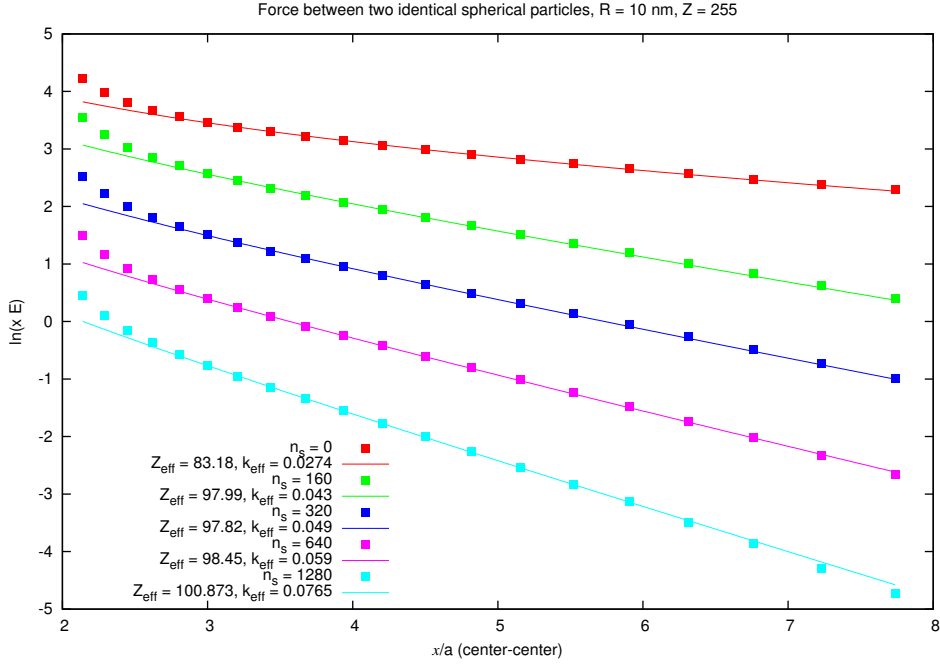


Figure 5.2.2.: The iterative boundaries finite element solution of the system described by Kreer et al. fitted by eq. 5.1.3. The logarithm of the electric field times the macro-ion separation,  $x E$ , is shown as a function of the separation where the obtained values for salt concentrations  $n_s = 0, 160, 320$  and  $640$  are shifted by 4, 3, 2 and 1 respectively for the sake of clarity.

give a hint to the assumption that within the validity of the potential of mean force, cell model charge renormalization remains valid even if the definition of a Wigner-Seitz cell is not unambiguous.

However, the origin of the deviations remains an open question. Of course there are effects of excluded volume expected in explicit ion simulations, but the influence is not expected for separations  $x \gtrsim \lambda_D$ . As our calculations showed, as long as the mean-field approach can be regarded as being valid, the deviations cannot be explained by nonlinear effects either. We also cannot eliminate a possible influence in the simulation data, as Kreer et al. reported a distance of  $7\lambda_D$  between periodic images of the colloids, and at these distances osmotic pressure might still influence the inter-colloidal forces.

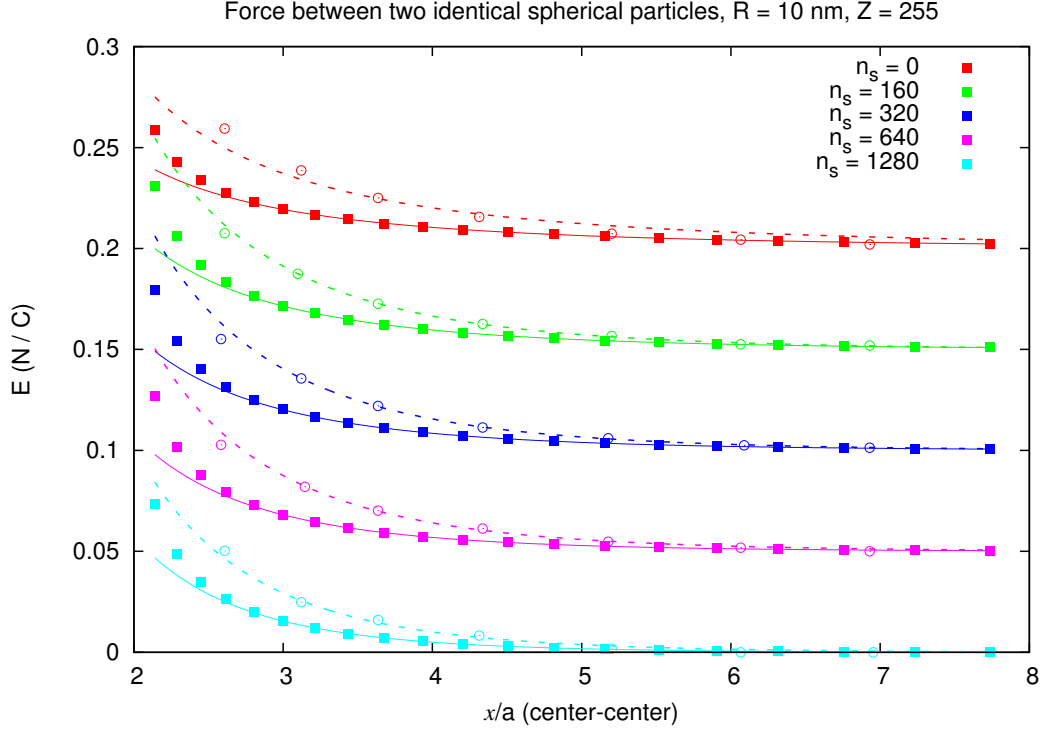


Figure 5.2.3.: The electric field obtained by our finite element procedure is compared to the results of Molecular Dynamic studies by Kreer et al. The results are shifted by 0.2 for  $n_s = 0$ , 0.15 for  $n_s = 160$ , 0.1 for  $n_s = 320$  and 0.05 for  $n_s = 640$  respectively.

$n_s$	$Z_{\text{eff}}$ (IPBS)	$Z_{\text{eff}}$ (Kreer)	$Z_{\text{eff}}$ (eq. 5.2.3)	$\kappa$ (IPBS)	$\kappa$ (Kreer)	$\kappa$
0	83.2	111.9	88.3	0.0274	0.0138	0.0333
160	98.0	142.5	91.7	0.043	0.052	0.0425
320	97.8	144.9	94.4	0.049	0.057	0.05
640	98.5	141.7	98.7	0.059	0.059	0.062
1280	100.9	132.8	105.5	0.077	0.069	0.082

Table 5.2.2.: Fit parameters of the IPBS solution and analytical predictions. We also performed a fit to MD data by Kreer et.al. ([44], fig. 1). The effective colloidal charge is determined at various salt concentrations, that correspond to the number of ions in the system (eq. 5.2.7).

### 5.3. Influence of jumps of the dielectric constant at the colloids surface

A novel feature of our algorithm is that it allows us to treat dielectric contrast at the surface of colloidal particles in a natural way (see chapter 3.4). As a sample application we applied the method to suspensions of charged colloidal spheres, though there exist several other applications like aerosols, toner particles of laser printers [64] and water droplets in clouds [55]. An influence on electrostatic interactions in quasi-two-dimensional nano-slits of silica filled with salt solution and spherical colloidal particles [46] or DNA [45] is also expected.

Bichoutskaia et al. [14] recently presented a general solution to the Poisson problem of charged dielectric particles using a multipole expansion, showing that there are configurations of interacting dielectric spheres, where attractive forces act between likely charged particles. As a first correction to the case of two unpolarizable spheres (i.e.  $\varepsilon_1 = \varepsilon_2$ ) their calculations provides the force between a non-polarizable sphere (radius  $a_1$ , charge  $q_1$ ) and a polarizable sphere of dielectric constant  $\varepsilon_2$ , radius  $a_2$  and charge  $q_2$  to be

$$F^1 = \ell_B \frac{q_1 q_2}{x^2} - \ell_B \frac{q_1^2}{x^2} \sum_{m=1}^{\infty} \frac{(\varepsilon_2 - 1)m(m+1)}{(\varepsilon_2 + 1)m + 1} \frac{a_2^{2m+1}}{x^{2m+1}}. \quad (5.3.1)$$

Here the sum is taken over all multipole contributions. So the first correction to the monopole of a point charge is the dipole contribution which already scales  $\propto 1/x^5$  for the case of the Poisson problem. In an electrolyte solution, additional screening has to be considered such that the influence of the jump in the dielectric constant at the surface will scale at most  $\propto \exp(-\kappa x)/x^5$ , so we should expect notably differences only for small distances.

The influence of dielectric contrast at the colloid's surface can be explained by the following considerations. For bad dielectric colloids,  $\varepsilon_2 \ll \varepsilon_1$ , an induced charge density will be influenced at the surface trying to push out the field lines of the electric field. According to equation 3.4.12, the sign of the influenced charge density will be such that it counteracts the source of the external field  $E_{\text{ext}}$  as previously defined, i.e. mainly the field of the second particle. The additional force will therefore be repulsive, and following the same argumentation for the case  $\varepsilon_2 \gg \varepsilon_1$  the resulting force will be reduced compared to the case without mismatch.

To check how large the influence of the dielectric contrast at the colloid's surface has on the force between them, we modeled a system containing two spherical colloids of charge  $Z = 255$  and radius  $a = 40$  nm where the salt concentration was chosen such that  $\kappa a = 1$ . The calculations were performed for particles with low dielectric constant compared to water as well as for good dielectric spheres. Figure 5.3.1 shows the resulting forces. The first interesting observation is, that for the case without dielectric contrast, the DLVO force prediction is fulfilled precisely down to a surface-surface separation of  $0.4\lambda_D$ , i.e. a region where very large overlap of the Debye layer is expected. This indicates

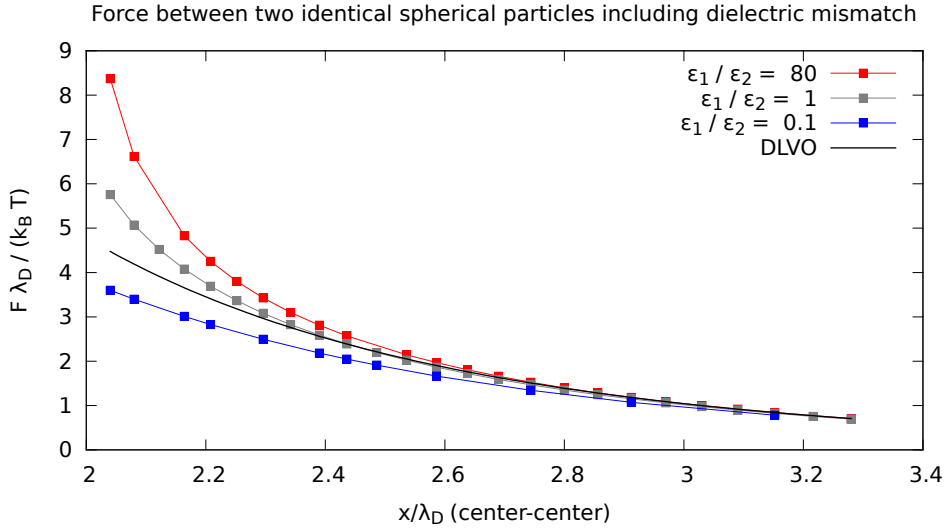


Figure 5.3.1.: The force between two spherical colloids ( $a = \lambda_D = 40$  nm,  $Z = 255$ ) gets influenced by jumps of the dielectric constant at separations  $x \lesssim \lambda_D$ . Calculations were performed for bad dielectric colloids,  $\varepsilon_1/\varepsilon_2 = 80$ , metal-like good dielectric colloids  $\varepsilon_1/\varepsilon_2 = 0.1$  and for  $\varepsilon_1 = \varepsilon_2$ . Also shown is the DLVO force curve for the renormalized effective charge.

that the charge renormalization concept introduced by Alexander et al. is an excellent tool for many areas of applications to calculate the effective forces in colloidal suspensions.

As figure 5.3.1 shows, the influence of dielectric properties of the colloids gives significant contributions only if the particles have a surface-surface separation of the order of one Debye length. However, for colloids in confinement these effects might give a significant contribution and should be examined further.



## 6. Conclusions and outlook

We have devised an iterative technique to determine the correct boundary conditions to solve the nonlinear Poisson–Boltzmann equation in the presence of dielectric mismatch for problems whose lack of symmetry prevents the use of constant potential or constant field boundary conditions.

Our implementation in a Finite Element scheme employed the DUNE framework and provides a highly efficient computer program, ensures extensibility and re-usability, and offers adaptive mesh refinement and full parallelization for computational highly demanding tasks. An easy-to-use interface is provided *inter alia* which takes advantage of the GMSH software to generate meshes for the Finite Element representation. A large variety of applications can be addressed by making use of the available symmetries, allowing calculations in one, two and three dimensions.

The scheme is capable to solve problems for systems characterized by a dielectric mismatch between macro-particles and solution. Polarization effects are directly included in the iterative determination of the boundary conditions. In the present work we checked thoroughly the implementation and accuracy of the algorithm by comparing calculation results with known analytical solutions. In particular, for the case of dielectric mismatch, the case of two spherical, charged discs in a salt solution – for which also the analytical solution is available – was checked. The iterative procedure, which we dubbed IPBS (Iterative Poisson–Boltzmann Solver), was capable of reproducing up to the required accuracy the analytical results in all tests. The accuracy, besides finite size effects, depends only on the mesh refinement near the surfaces.

The method was then applied to the problem of two charged colloidal particles in an electrolyte solution. For the case without dielectric mismatch we showed that the IPBS solution of the nonlinear Poisson–Boltzmann equation is capable of reproducing the effective force between the colloids predicted by charge renormalization theory in its range of validity (colloidal particles larger than the screening length), while it delivers new insight into the case where colloidal particles are small compared to the screening length. When dielectric mismatch is considered, we found that at small separations between charged colloidal particles, strong forces due to the polarization charges appears, which should not be neglected.

In future, IPBS could be used to address various interesting problems like charged colloids in front of a polarizable plane or in confinement, DNA translocation through nano-pores or the examination of pairwise additivity of multi-body interaction within the

## *6. Conclusions and outlook*

---

framework of Poisson–Boltzmann theory, becoming a valuable tool in the investigation of charged soft-matter in the presence of confinement.

## 7. Acknowledgements

In the following, I would like to thank all those that helped me during my studies and with this thesis in various ways, especially:

**Prof. Dr. Christian Holm** for supervising this thesis and introducing me into the fields of soft matter and computational physics.

**Riccarda** for supporting me all the time and being the epicenter of my life.

**Stefan Kesselheim** for his patience in debugging hard-to-find bugs in my code, lots of stimulating discussions and his help with the analytical calculations.

**My Parents**, who simply made it all possible.

**Dr. Marcello Sega** for his support and discussions.

**Dr. Bernd Flemisch** helping me to fight some of the difficulties with DUNE.

**The DUNE-project** for their great software and for their support on the mailing list.



## A. Analytical results

### A.1. Gouy-Chapman theory of a charged plane

The first use of Poisson–Boltzmann theory describing the electric double layer formation near a charged plane was made by Gouy in 1910 [31] and Chapman in 1913 [17], introducing the replacement of the potential of mean-force by the mean electrostatic potential (see chapter 2.2).

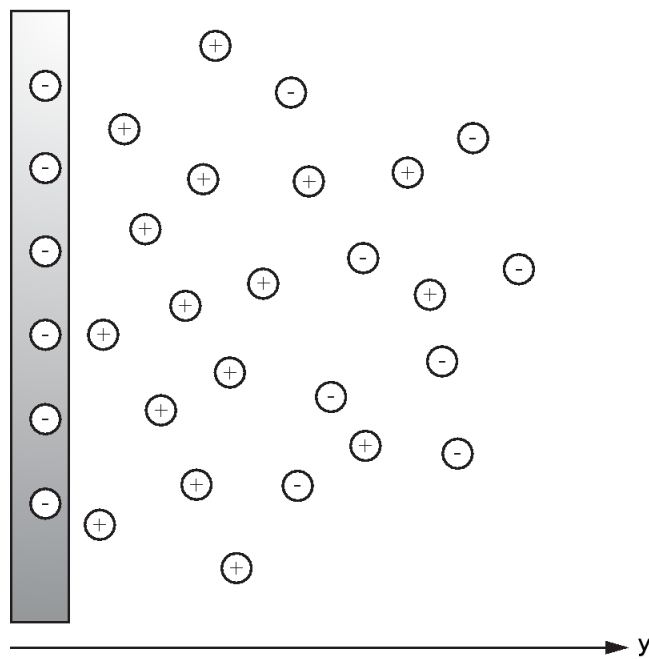


Figure A.1.1.: A charged plane immersed into an electrolyte solution attracting solution ions of the same sign while repelling those of opposite sign. This electrical double layer imposes an effective screening to the electrostatic potential on the Gouy-Chapman length  $\lambda$ .

In the planar case, the Poisson–Boltzmann equation 2.3.6 is analytical solvable,

## A. Analytical results

---

resulting in

$$\frac{d^2\phi}{dy^2} = -4\pi\ell_B e \sum_i z_i c_i^{eq} \exp(-z_i\phi(\mathbf{r})). \quad (\text{A.1.1})$$

Assuming the plane, described by a surface charge density  $\sigma$ , is located in the origin and the solvent, characterized by the dielectric constant  $\epsilon$ , fills the half-space  $y > 0$ , we can set-up the boundary conditions. At infinite distance,  $y \rightarrow \infty$ , Gauss' law requires the derivative of the potential to be zero,

$$\left. \frac{d\phi}{dy} \right|_{z \rightarrow \infty} = 0, \quad (\text{A.1.2})$$

while at the plane's surface the jump in the derivative is given by (2.1.10) and we replace the dielectric constant of the plane by an induced surface charge density  $\sigma^{ind}$  as described in section 3.4, yielding

$$\left. \frac{d\phi}{dy} \right|_{z=0} = -4\pi\ell_B \sigma. \quad (\text{A.1.3})$$

Eq. A.1.1 can then be transformed into an integrable form, using the identity,

$$\frac{d}{dy} \left( \frac{df}{dy} \right)^2 = 2 \frac{d^2 f}{dy^2} \frac{df}{dy}, \quad (\text{A.1.4})$$

and multiplying both sides with  $2d\phi/dy$ , and intergrating from a point infinitely far away from the plain, for which we know that  $\phi(\infty) = 0$  to a point  $y_0$  yields

$$\begin{aligned} \int_{\infty}^{y_0} \frac{d}{dy} \left( \frac{d\phi}{dy} \right)^2 dy &= \int_{\infty}^{y_0} - \left( \frac{d\phi}{dy} \right) 8\pi\ell_B e \sum_i z_i c_i^{eq} \exp(-z_i\phi(\mathbf{r})) dy \\ &= \int_{\infty}^{y_0} \frac{d}{dy} \left( 8\pi\ell_B e \sum_i z_i c_i^{eq} \exp(-z_i\phi(\mathbf{r})) \right) dy, \end{aligned} \quad (\text{A.1.5})$$

where we used chain-rule in the last step. This transforms the Poisson–Boltzmann equation for this particular setup into a differential equation of first order in one dimension,

$$\left( \frac{d\phi}{dy} \right)^2 = 8\pi\ell_B e \sum_i z_i c_i^{eq} (\exp(-z_i\phi) - 1) + C_1. \quad (\text{A.1.6})$$

We will now limit the analysis to the case of a symmetric  $z-z$  electrolyte, simplifying the sum on the r.h.s. of the latter expression

$$\begin{aligned} \exp(-z\Phi) + \exp(z\Phi) - 2 &= 2 \cosh(z\Phi) - 2 \\ &= 4 \sinh^2 \left( \frac{z\Phi}{2} \right) \end{aligned} \quad (\text{A.1.7})$$

Using the Debye length  $\lambda_D$  as defined in eq. 2.4.2 for the symmetric electrolyte, eq. A.1.6 simplifies to

$$\left(\frac{d\phi}{dy}\right)^2 = 4\frac{\kappa^2}{z} \sinh^2\left(\frac{z\phi}{2}\right). \quad (\text{A.1.8})$$

The integration constant  $C_1$  can be determined using the boundary condition A.1.2, resulting in  $C_1 = 0$ . Furthermore we already assumed  $\phi(\infty) = 0$ , such that when taking the square root of the latter equation, we choose the sign in such a way that  $d\phi/dy < 0$  if  $\phi > 0$  and  $d\phi/dy < 0$  if  $\phi < 0$ , resulting in

$$\frac{d\phi}{dy} = -2\frac{\kappa}{z} \sinh\left(\frac{z\Phi}{2}\right). \quad (\text{A.1.9})$$

Integration of the latter expression then yields

$$\int \frac{dy}{d\phi} d\phi = \int \frac{1}{2\kappa \sinh(-\frac{z\phi}{2})} d\phi + C_2 \quad (\text{A.1.10})$$

$$y = \frac{2}{\kappa z} \operatorname{arctanh}\left(e^{-\frac{z\phi}{2}}\right), \quad (\text{A.1.11})$$

which can be transformed to

$$\phi(z) = -\frac{2}{z} \ln \left[ \tanh\left(\frac{\kappa z}{2}(y - C_2)\right) \right] \quad (\text{A.1.12})$$

Using the boundary condition from eq. (A.1.3) at the plane's surface and eq. A.1.9 we can determine the integration constant  $C_2$ ,

$$\left.\frac{d\phi}{dy}\right|_{y=0} = -2\frac{\kappa}{z} \sinh\left(\frac{z\phi_0}{2}\right) = -4\pi\ell_B\sigma \quad (\text{A.1.13})$$

$$\phi_0 = \frac{2}{z} \operatorname{arcsinh}\left(\frac{\ell_B z 2\pi}{\kappa}\sigma\right), \quad (\text{A.1.14})$$

and using eq. A.1.12 at  $y = 0$  finally yields

$$\begin{aligned} \phi_0 &= -\frac{2}{z} \ln \left[ \tanh\left(-\frac{C_2 \kappa z}{2}\right) \right] \\ C_2 &= -\frac{2}{\kappa z} \ln \left[ \tanh\left(\frac{z\phi_0}{4}\right) \right]. \end{aligned} \quad (\text{A.1.15})$$

Inserting the expression for  $C_2$ , the expression for the potential in the Gouy-Chapman description can be simplified to

$$\phi(y) = \frac{2}{z} \ln \left[ \frac{1 + \tanh\left(\frac{1}{4}\phi_0\right) \exp(-\kappa z y)}{1 - \tanh\left(\frac{1}{4}\phi_0\right) \exp(-\kappa z y)} \right]. \quad (\text{A.1.16})$$



# List of Figures

1.1.1. Mesoscopic spheres interaction through an electrolyte solution . . . . .	2
2.1.1. Jump of the electric field at the surface . . . . .	10
3.1.1. Typical computational domain for a finite element method . . . . .	28
3.1.2. Polynomial approximation of a continuous function . . . . .	29
3.1.3. Numbering of nodes in the finite element method . . . . .	30
3.1.4. Illustration of one-dimensional linear elements . . . . .	31
3.3.1. Sample grid obtained by Gmsh using a Delaunay triangulation . . . . .	38
3.4.1. Cylindrical coordinate system used for exploiting symmetry . . . . .	44
4.1.1. Relative error of the IPBS solution . . . . .	50
4.1.2. Electric field of the spherical cell model compared to IPBS . . . . .	51
4.1.3. IPBS solution compared to Debye-Hückel approximation . . . . .	53
4.1.4. Surface potential of a sphere calculated with IPBS and Debye-Hückel theory	54
4.1.5. Surface potential of a large sphere ( $\kappa a \gg 1$ ) calculated with IPBS com- pared to Debye-Hückel and Gouy-Chapman theory . . . . .	55
4.2.1. Meshes used for modeling charged planes . . . . .	58
4.2.2. Relative error of approximating an infinite plane . . . . .	59
4.2.3. Gouy-Chapman potential of a plane surface in different symmetries. . . . .	60
4.2.4. Two infinite charged planes. . . . .	61
4.2.5. Electrostatic potential between of two charged planes. . . . .	63
4.2.6. Electrostatic potential between of two charged planes including dielectric mismatch between the wall and the solution. . . . .	65
5.1.1. Force between two equal spherical particles without dielectric mismatch compared to the DLVO theory . . . . .	70
5.1.2. Effective ion density between two equally charged spherical particles . . .	72
5.1.3. Definition of the angular integration shell of the effective ion density . .	73
5.1.4. Integrated charge density within a spherical shell around a spherical colloid	74
5.1.5. Comparison of the force between two identical spherical particles having a constant surface charge density to those having iterated one . . . . .	75
5.1.6. Iterative boundary conditions are compared to the bare (single) colloid boundary conditions . . . . .	76
5.2.1. Reproduction of effective colloidal charges (Alexander theory) using the iterative boundary value method . . . . .	78

*List of Figures*

---

5.2.2. Effective electric field between two macro-ions at different salt concentrations	80
5.2.3. Effective electric field between two macro-ions at different salt concentrations compared to data by Kreer et.al.	81
5.3.1. Force between colloidal particles in an electrolyte solution including dielectric mismatch	83
A.1.1. Electric double layer in front of a charged plane	89

## List of Tables

5.2.1. Effective colloidal charge resulting from IPBS solution and Alexander's theory . . . . .	79
5.2.2. Comparison of IPBS solution, analytical predictions and MD data by Kreer et al. for the effective colloidal charge at various salt concentrations . . . . .	81



# Bibliography

- [1] M. Abramowitz and I. Stegun. *Handbook of mathematical functions*. Dover Publications Inc., New York, 1970.
- [2] Ariel Abramshkin, David Andelman, and Henri Orland. Dipolar poisson-boltzmann equation: Ions and dipoles close to charge interfaces. *Phys. Rev. Lett.*, 99(7):077801, Aug 2007.
- [3] S. Alexander, P. M. Chaikin, P. Grant, G. J. Morales, P. Pincus, and D. Hone. Charge renormalization, osmotic-pressure, and bulk modulus of colloidal crystals - theory. *J. Chem. Phys.*, 80(11):5776–5781, 1984.
- [4] David Andelman and W. Poon. *Proceedings of the Nato ASI & SUSSP on Soft condensed matter physics in molecular and cell biology*, volume 121 of *Proceedings of the Nato ASI & SUSSP*, chapter Introduction To Electrostatics in Soft and Biological Matter, pages 97–122. Taylor & Francis, New York, 2005.
- [5] M. Aubouy, Emmanuel Trizac, and Lyderic Bocquet. Effective charge versus bare charge: an analytical estimate for colloids in the infinite dilution limit. *J. Phys. A: Math. Gen.*, 36(22):5835–5840, 2003.
- [6] M. C. Barbosa, M. Deserno, C. Holm, and R. Messina. Screening of spherical colloids beyond mean field: A local density functional approach. *Phys. Rev. E*, 69:051401, 2004.
- [7] Eytan Barouch and Egon Matijevic. Double-layer interactions of unequal spheres. part 1.-the effect of electrostatic attraction with particles of like sign of potential. *J. Chem. Soc., Faraday Trans. 1*, 81(8):1797–1817, 1985.
- [8] P. Bastian, M. Blatt, A. Dedner, C. Engwer, R. Klöfkorn, R. Kornhuber, M. Ohlberger, and O. Sander. A generic grid interface for parallel and adaptive scientific computing. part I: Abstract framework. *Computing*, 82(2–3):103–119, 2008.
- [9] P. Bastian, M. Blatt, A. Dedner, C. Engwer, R. Klöfkorn, R. Kornhuber, M. Ohlberger, and O. Sander. A generic grid interface for parallel and adaptive scientific computing. part II: Implementation and tests in DUNE. *Computing*, 82(2–3):121–138, 2008.
- [10] J. Baumgartl, J.L. Arauz-Lara, and C. Bechinger. Like charge attraction in confinement: Myth or truth? *Soft Matter*, 2:631, 2006.
- [11] Clemens Bechinger and Hans-Hennig von Grünberg. Wenn drei körper mehr sind als

## Bibliography

---

- drei paare. *Physik Journal*, 3(11):33–38, 2004.
- [12] G. M. Bell and S. Levine. Statistical thermodynamics of concentrated colloidal solutions. part 2.-general theory of the double-layer forces on a colloidal particle. *Trans. Faraday Soc.*, 54:785–798, 1958.
  - [13] Gerhard Besold. Derivation of the poisson-boltzmann equation. Lecture Course Material, 2006.
  - [14] Elena Bichoutskaia, Adrian L. Boatwright, Armik Khachatourian, and Anthony J. Stace. Electrostatic analysis of the interactions between charged particles of dielectric materials. *The Journal of Chemical Physics*, 133(2):024105, 2010.
  - [15] N. Bjerrum. A new form for the electrolyte dissociation theory. In *Proceedings of the 7th International Congress of Applied Chemistry, Section X*, pages 55 – 60, 1909.
  - [16] Lesser Blum. Theory of electrified interfaces. *The Journal of Physical Chemistry*, 81(2):136–147, 1977.
  - [17] D. L. Chapman. *Philos. Mag.*, 25:475, 1913.
  - [18] P. Debye and E. Hückel. Zur Theorie der Elektrolyte. I. Gefrierpunktserniedrigung und verwandte Erscheinungen. *Phys. Z.*, 24(9):185, 1923.
  - [19] B. V. Derjaguin and L. D. Landau. Theory of the stability of strongly charged lyophobic sols and of the adhesion of strongly charged particles in solutions of electrolytes. *Acta Physicochim. (USSR)*, 14:633–650, 1941.
  - [20] M. Deserno. Rayleigh instability of charged droplets in the presence of counterions. *Eur. Phys. J. E*, 6:163–168, 2001.
  - [21] M. Deserno and C. Holm. Cell-model and poisson-boltzmann-theory: A brief introduction. In C. Holm, P. Kékicheff, and R. Podgornik, editors, *Electrostatic Effects in Soft Matter and Biophysics*, volume 46 of *NATO Science Series II - Mathematics, Physics and Chemistry*, pages 27–50. Kluwer Academic Publishers, Dordrecht, NL, December 2001.
  - [22] J. Dobnikar, D. Halozan, M. Brumen, H. H. von Grünberg, and R. Rzehak. Poisson-boltzmann brownian dynamics of charged colloids in suspension. *Computer Physics Communications*, 159(2):73–92, May 2004.
  - [23] Jure Dobnikar, Matthias Brunner, Hans-Hennig von Grünberg, and Clemens Bechinger. Three-body interactions in colloidal systems. *Phys. Rev. E*, 69(031402), 2004.
  - [24] H. Eisenberg. *Biological Macromolecules and Polyelectrolytes in Solution*. Clarendon Press, Oxford, 1976.
  - [25] H.C. Elman, D.J. Silvester, and A.J. Wathen. *Finite elements and fast iterative solvers: with applications in incompressible fluid dynamics*. Oxford University Press, 2005.

- [26] D. F. Evans and H. Wennerström. *The Colloidal Domain*. Wiley-VCH, New York, 1999.
- [27] A. Fernández-Nieves, J. S. van Duijneveldt, A. Fernández-Barbero, B. Vincent, and F. J. de las Nieves. Structure formation from mesoscopic soft particles. *Phys. Rev. E*, 64(5):051603, Oct 2001.
- [28] F. Fogolari, A. Brigo, and H. Molinari. The poisson-boltzmann equation for biomolecular electrostatics: a tool for structural biology. *Journal of Molecular Recognition*, 15(6):377–392, 2002.
- [29] R.H. Fowler and E.A. Guggenheim. *Statistical thermodynamics: a version of statistical mechanics for students of physics and chemistry*. The Macmillan Company, 1939.
- [30] Christophe Geuzaine and Jean-Francois Remacle. Gmsh: A 3-d finite element mesh generator with built-in pre- and post-processing facilities. *Int. J. Numer. Meth. Engng.*, 79(11):1309–1331, 2009.
- [31] G. L. Gouy. *J. de Phys.*, 9:457, 1910.
- [32] C. Gutsche, U. F. Keyser, K. Kegler, and F. Kremer. Forces between single pairs of charged colloids in aqueous salt solutions. *PHYSICAL REVIEW E*, 76(3, Part 1), SEP 2007.
- [33] J. P. Hansen and I. R. McDonald. *Theory of Simple Liquids*. Academic Press, London, 1986.
- [34] M Holst and F Saied. Numerical solution of the nonlinear poisson-boltzmann equation - developing more robust and efficient methods. *Journal of Computational Chemistry*, 16(3):337–364, MAR 1995.
- [35] Michael Holst and Faisal Saied. Multigrid solution of the poisson-boltzmann equation. *Journal of Computational Chemistry*, 14(1):105–113, 1993.
- [36] Cheng-Hsuan Huang, Wen-Li Cheng, Yan-Ying He, and Eric Lee. Electrophoresis of a soft particle within a cylindrical pore: Polarization effect with the nonlinear poisson–boltzmann equation. *The Journal of Physical Chemistry B*, 114(31):10114–10125, 2010.
- [37] R.J. Hunter and L.R. White. *Foundations of colloid science*. Number Bd. 2 in Oxford science publications. Clarendon Press, 1989.
- [38] J. Israelachvili. *Intermolecular and Surface Forces*. Academic, London, 1992.
- [39] R. Rzehak J. Dobnikar and H. H. von Grünberg. Effect of many-body interactions on the solid-liquid phase behavior of charge-stabilized colloidal suspensions. *Europhysics Letters*, 61(5):695–701, 2003.
- [40] J. D. Jackson. *Classical Electrodynamics*. Wiley, New York, 3rd edition, 1999.

## Bibliography

---

- [41] Richard A. L. Jones. *Soft Condensed Matter*. Oxford University Press, Great Clarendon Street, Oxford OX2 6DP, 2002.
- [42] K. Kegler, M. Salomo, and F. Kremer. Forces of interaction between dna-grafted colloids: An optical tweezer measurement. *Phys. Rev. Lett.*, 98(5):058304–, February 2007.
- [43] John G. Kirkwood. On the theory of strong electrolyte solutions. 2(11):767–781, 1934.
- [44] T. Kreer, J. Horbach, and A. Chatterji. Nonlinear effects in charge stabilized colloidal suspensions. *PHYSICAL REVIEW E*, 74(2, Part 1), AUG 2006.
- [45] M. Krishnan, I. Monch, and P. Schwille. Spontaneous stretching of dna in a two-dimensional nanoslit. *Nano Letters*, 7(5):1270–1275, 2007.
- [46] Madhavi Krishnan, Zdenk Petrek, Ingolf Mnch, and Petra Schwille. Electrostatic self-assembly of charged colloids and macromolecules in a fluidic nanoslit. *Small*, 4(11):1900–1906, 2008.
- [47] L.D. Landau, E.M. Lifšic, V.B. Beresteckij, P. Ziesche, and G. Heber. *Lehrbuch der theoretischen Physik: Elektrodynamik der Kontinua*. Deutsch, 1985.
- [48] Joseph E. Ledbetter, Thomas L. Croxton, and Donald A. McQuarrie. The interaction of two charged spheres in the poisson-boltzmann equation. *Canadian Journal of Chemistry*, 59(13):1860–1864, 1981.
- [49] S. Levine and G. M. Bell. Modified poisson-boltzmann equation and free energy of electrical double layers in hydrophobic colloids. *Discuss. Faraday Soc.*, 42:69–80, 1966.
- [50] Hartmut Löwen, Jean-Pierre Hansen, and Paul A. Madden. Nonlinear counterion screening in colloidal suspensions. *J. Chem. Phys.*, 98(4):3275–3289, 1993.
- [51] Brock A. Luty, Malcolm E. Davis, and J. Andrew McCammon. Solving the finite-difference non-linear poisson-boltzmann equation. *Journal of Computational Chemistry*, 13(9):1114–1118, 1992.
- [52] B. A. Mann, C. Holm, and K. Kremer. The swelling behaviour of charged hydrogels. *Macromolecular Symposia*, 237:90–107, 2006.
- [53] R. A. Marcus. Calculation of thermodynamic properties of polyelectrolytes. *J. Chem. Phys.*, 23(6):1057–1068, 1955.
- [54] Donald A. McQuarrie. *Statistical Mechanics*. Harper’s chemistry series. Harper Collins, New York, 1976.
- [55] Harry T. Ochs and Robert R. Czys. Charge effects on the coalescence of water drops in free fall. *Nature*, 327(6123):606–608, June 1987.
- [56] Lars. Onsager. Theories of concentrated electrolytes. *Chemical Reviews*, 13(1):73–89,

- 1933.
- [57] DUNE Project. DUNE - Distributed and Unified Numerics Environment. <http://dune-project.org/>.
  - [58] Dune Project. *dune-pdelab Howto*. Interdisziplinäres Zentrum für Wissenschaftliches Rechnen, Universität Heidelberg, Im Neuenheimer Feld 368, D-69120 Heidelberg, July 2011.
  - [59] J.N. Reddy. *An introduction to the finite element method*. McGraw-Hill series in mechanical engineering. McGraw-Hill Higher Education, 2006.
  - [60] Walter Ritz. Ueber eine neue methode zur loesung gewisser variationsprobleme der mathematischen physik. *Journal fuer die reine und angewandte Mathematik (Crelles Journal)*, 1909(135):1–61, 1909.
  - [61] I. Rouzina and V. A. Bloomfield. Macroion attraction due to electrostatic correlation between screening counterions. 1. mobile surface-adsorbed ions and diffuse ion cloud. *J. Phys. Chem.*, 100(23):9977–9989, 1996.
  - [62] W. B. Russel, D. A. Saville, and W. R. Schowalter. *Colloidal Dispersions*. Cambridge University Press, Cambridge, UK, 1989.
  - [63] J. E. Sader and D. Y. Chan. Long-range electrostatic attractions between identically charged particles in confined geometries: An unresolved problem. *J. Colloid Interface Sci.*, 213:268, 1999.
  - [64] A. A. Sickafouse, J. E. Colwell, M. Horanyi, and S. Robertson. Photoelectric charging of dust particles in vacuum. *Phys. Rev. Lett.*, 84(26):6034–6037, June 2000.
  - [65] Dieter Suess. Computational physics: The finite element method. Lecture Script, 2008.
  - [66] B. V. R. Tata, M. Rajalakshmi, and Akhilesh K. Arora. Vapor-liquid condensation in charged colloidal suspensions. *Phys. Rev. Lett.*, 69(26):3778–3781, Dec 1992.
  - [67] B. N. Taylor, International Bureau of Weights and Measures, United States. Dept. of Commerce. Technology Administration, and National Institute of Standards and Technology (U.S.). *The international system of units (SI)*. U.S. Dept. of Commerce, Technology Administration, National Institute of Standards and Technology, Gaithersburg, MD, 2001.
  - [68] Emmanuel Trizac, Lyderic Bocquet, M. Aubouy, and Hans-Hennig von Grünberg. Alexander’s prescription for colloidal charge renormalization. *Langmuir*, 19(9):4027–4033, 2003.
  - [69] C. Tyagi, M. Süzen, M. Sega, M. Barbosa, S. Kantorovich, and C. Holm. An iterative, fast, linear-scaling method for computing induced charges on arbitrary dielectric boundaries. *Journal of Chemical Physics*, 132, 2010.
  - [70] René van Roij, Marjolein Dijkstra, and Jean-Pierre Hansen. Phase diagram of charge-

## Bibliography

---

- stabilized colloidal suspensions: van der waals instability without attractive forces. *Phys. Rev. E*, 59(2):2010–2025, Feb 1999.
- [71] E. J. Verwey and J. T. G. Overbeek. *Theory of the stability of Lyophobic Colloids*. Elsevier, Amsterdam, 1948.
  - [72] D.M. Young. A historical overview of iterative methods. *Comput. Phys. Commun.*, 53(1-3):1–17, 1989.